December 2017

Oxygen Transport Membrane Reactors for Oxy-Fuel Combustion and Carbon Capture Purposes

Ryan Falkenstein-Smith
Syracuse University

Abstract

This thesis investigates oxygen transport membrane reactors (OTMs) for the application of oxy-fuel combustion. This is done by evaluating the material properties and oxygen permeability of different OTM compositions subjected to a variety of operating conditions. The scope of this work consists of three components: (1) evaluate the oxygen permeation capabilities of perovskite-type materials for the application of oxy-fuel combustion; (2) determine the effects of dual-phase membrane compositions on the oxygen permeation performance and membrane characteristics; and (3) develop a new method for estimating the oxygen permeation performance of OTMs utilized for the application of oxy-fuel combustion.

$SrSc_{0.1}Co_{0.9}O_{3-\delta}$ (SSC) is selected as the primary perovskite-type material used in this research due to its reported high ionic and electronic conductive properties and chemical stability. SSC's oxygen ion diffusivity is investigated using a conductivity relaxation technique and thermogravimetric analysis. Material properties such as chemical structure, morphology, and ionic and electronic conductivity are examined by X-ray diffraction (XRD), Scanning Electron Microscope (SEM), and conductivity testing using a four-probe method, respectively. Oxygen permeation tests study the oxygen permeability OTMs under modified membrane temperatures, sweeping gas flow rates, sweeping gas compositions, membrane configurations, and membrane compositions. When utilizing a pure CO_2 sweeping gas, the membrane composition was modified with the addition of $Sm_{0.2}Ce_{0.8}O_{1.9-\delta}$ (SDC) at varying wt.% to improve the membranes mechanical stability. A newly developed method to evaluate the oxygen permeation performance of OTMs is also presented by fitting OTM's oxygen permeability to the methane fraction in the sweeping gas composition. The fitted data is used to estimate the overall performance and size of OTMs utilized for the application of oxy-fuel combustion.

The findings from this research show that under a wide range of membrane temperatures and in a variety of atmospheres, a pure SSC OTM can achieve superior surface exchange and oxygen chemical diffusion coefficients compared to other commonly studied materials. SSC's high oxygen permeability (>1 $ml.min^{-1}.cm^{-2}$) demonstrates the material's candidacy for the application of oxy-fuel combustion. However, in the presence of rich CO_2 atmospheres, SSC shows mechanical and chemical instabilities due to the carbonate formation on the perovskite structure. The addition of SDC in the membrane composition produces a dual-phase OTM which is observed to improve the oxygen permeation flux when subjected to pure CO_2 sweeping gases. When subjected to pure methane sweeping gases, dual-phase OTM compositions exhibits lower oxygen permeability compared to the single-phase SSC OTM. Despite the decline in the oxygen permeation flux, some dual-phase compositions still exhibit a high oxygen permeability, indicating their potential for the application of oxy-fuel combustion. Furthermore, a newly developed method for evaluating OTMs for the application of oxy-fuel combustion is presented in a portion of this work. This new method calculates key components such as the average oxygen permeation flux, approximate effective surface area, and the impact of additional recirculated exhaust into the incoming sweeping gas to provide a detailed understanding of OTM's application for oxy-fuel combustion. The development of this approach will aid in the evaluation of newly developed materials and create a new standard for implementing OTMs for the application of oxy-fuel combustion.

Oxygen Transport Membrane Reactors for Oxy-Fuel Combustion and Carbon Capture Purposes

By
Ryan L. Falkenstein-Smith
B.S. Syracuse University, May 2013
M.S. Syracuse University, May 2015

DISSERTATION
SUBMITTED IN PARTIAL FULFILLMENT OF THE
REQUIREMENTS FOR THE DEGREE OF
DOCTOR OF PHILOSOPHY
IN
MECHANICAL AND AEROSPACE ENGINEERING

Syracuse University
December 2017

Acknowledgements

The experimental work presented in this study was conducted at the Combustion and Energy Research Laboratory in the Department of Mechanical and Aerospace Engineering at Syracuse University. Molecular dynamics simulations were developed by Prof. Hiroki Nagashima and Prof. Takashi Tokumasu at the Quantum Nanoscale Flow Systems Laboratory from the Institute of Fluid Science at Tohoku University. This research is based upon work partially supported by the IFS Collaborative Research Project J15085, an award from Empire State Development's Division of Science, Technology and Innovation (NYSTAR) through the Syracuse Center of Excellence (under award number #C120183) and an award from the National Science Foundation's East Asia and Pacific Summer Institutes Fellowship program (under award number #1614238).

I started this research as an undergraduate student under the mentorship of Dr. Jeongmin Ahn, who saw the potential of who I could become. The patience, dedication, and support he has given me over the past five years have motivated me to become a better researcher and more importantly a better person. I would also like to thank my committee members, Prof. Weiwei Zheng, Prof. Shalabh Maroo, Prof. Jianshun Zhang, Prof. Ed Bogucz, and Prof. Takashi Tokumasu, whose insight and wisdom has strengthened my abilities as a researcher.

I am also grateful for my Syracuse Community and their overwhelming support. Thank you to William Dossert, Richard Chave, and Sally Prasch for always delivering high quality and reliable manufactured parts and glass designs used for my experiments. Thank you to Arthur Stipanovic for aiding in the TGA experiments at ESF. Thank you to my laboratory predecessors Dr. Kang Wang and Dr. Pingying Zeng for guiding me through my first experiments and challenging me to be better. Thank you to Matt Rushby for aiding in the fabrication process of ceramic samples used

for a portion of these investigations. Thank you to Brian Carter and Tim LaBreche for their encouragement and aid in computational troubleshooting.

Lastly, I would like to thank my family for always being there for me. Thank you to my patient wife, Kelly, who never complained about me working long hours and weekends, and my mom, Linda, who was the most significant role-model, champion, and supporter in my life. I would not be where I am today without the people who have always supported me and for that, I am grateful.

Ryan Falkenstein-Smith
December 2017

Table of Contents

List of Figures

List of Tables

Nomenclature

A	Cross section area of sample bar (cm^2)
A_{ij}	Potential parameter (eV)
C_{ij}	Potential parameter ($eV/Å^{-6}$)
C_O	Molar concentration of oxygen in perovskite structure
δ	Oxygen nonstoichiometry
D_{Chem}	Oxygen chemical diffusion coefficient
D_O	Average oxygen diffusion coefficient
F	Faraday's constant
$\dot{F}_{total}$	Total sweeping gas flow rate ($ml.min^{-1}$)
J_{O_2}	Oxygen permeation flux ($ml.min^{-1}.cm^{-2}$)
K	Total resistance (Ω)
K_{ex} s	Surface exchange coefficient ($cm.s^{-1}$)
L_c	Characteristic thickness (cm)
L	Length of sample bars (cm)
$\dot{n}$	Molar flow rate ($mol.min^{-1}$)
pO_2'	Oxygen partial pressure on the OTM feed side (atm)
pO_2''	Oxygen partial pressure on the OTM permeation side (atm)
ρ_{ij}	Potential parameter (Å)
R	Universal gas constant ($J.mol^{-1}.K^{-1}$)
R_{diff}	Bulk diffusion resistance
R'_{ex}	Surface exchange resistance on the feed
R''_{ex}	Surface exchange resistance on the permeation

R_t	Total permeation resistance
σ	Total conductivity ($S.cm^{-1}$)
σ_{ion}	Ionic conductivity ($S.cm^{-1}$)
σ_e	Electronic conductivity ($S.cm^{-1}$)
T	Absolute temperature
μ_{O_2}	Chemical potential of oxygen
X	Component mole fraction of the i^{th} species

Acronyms

AZEP	Advanced zero emission power plants
ASU	Air separation unit
AESA	Approximate effective surface area
BSCF	$Ba_{0.5}Sr_{0.5}Co_{0.8}Fe_{0.2}O_{3-\delta}$
CCS	Carbon capture and sequestration
CLC	Chemical looping combustion
EBSD	Electron backscatter diffraction
ECR	Electronic conductivity relaxation technique
EDTA	Ethylenediaminetetraacetic acid
GC	Gas chromatograph
I.D.	Inner diameter
LSCF	$La_{0.6}Sr_{0.4}C_{0.2}Fe_{0.8}O_{3-\delta}$
MDS	Molecular dynamic simulation
MSD	Mean square displacement
O.D.	Outer diameter
OTM	Oxygen transport membrane reactors
SDC	$Sm_{0.2}Ce_{0.8}O_{1.9-ö}$
SEM	Scanning electronic microscopy
SOFCs	Solid oxide fuel cells
SSC	$SrSc_{0.1}Co_{0.9}O_{3-ö}$
STP	Standard temperature and pressure
TGA	Thermogravimetric analysis

Wt.%	Weight percentage
XRD	X-ray diffraction

Chapter 1 Introduction

1.1 Background

Our world is in peril. For over a century, fossil fuels have been the primary source of energy production that satisfies the increasing demand for almost every major country throughout the world [1]. Consequently, fossil fuel combustion produces a substantial portion of carbon dioxide (CO_2) emissions, making them the primary contributor to global climate change [2,3]. In response, several governments across the globe have developed legislation and commitments to reduce carbon emissions entering the atmosphere [4]. Due to these limitations, the power generation sector faces a difficult challenge: satisfying the rising global energy demand while simultaneously reducing combustion emissions without substantially sacrificing plant efficiency [5]. Already, power generation facilities have addressed this problem by adopting carbon capture and sequestration technology (CCS) into their existing infrastructures.

CCS technology can be broken down into three components. The first element is capturing CO_2 either physically, chemically or biologically pre-combustion, post-combustion, or during combustion. After successfully capturing CO_2, it is transported to a storage site, using large-scale heavy-duty gas tanks or pipelines. Finally, CO_2 can be stored either underground or underwater for long-term isolation where it will have little impact on geological storage surroundings [6,7].

There are three CCS processes: pre-combustion, post-combustion, and oxy-fuel combustion as shown in Fig. 1.1. In a pre-combustion, fuel (i.e., natural gas mainly comprised of methane) is reformed into a mixture of hydrogen and CO_2 [8]. Hydrogen then combusts with air providing cleaner power, while CO_2 is separated, captured, and contained. This process is achieved through absorption or adsorption of fuel mixtures, but at a substantial cost due to its inability to be retrofitted into current infrastructures [9,10]. Post-combustion uses amines as absorbents to

separate low concentrations of CO_2 from the plant's flue gas [11–14]. Although some have reported this approach to be an attractive solution, there have been some studies highlighting the safety risks when implementing highly hazardous chemicals used to capture CO_2 emissions [15]. Alternatively, oxy-fuel combustion has received growing attention due to its "off the shelf appeal" and ability to be integrated into current power generation facilities [16].

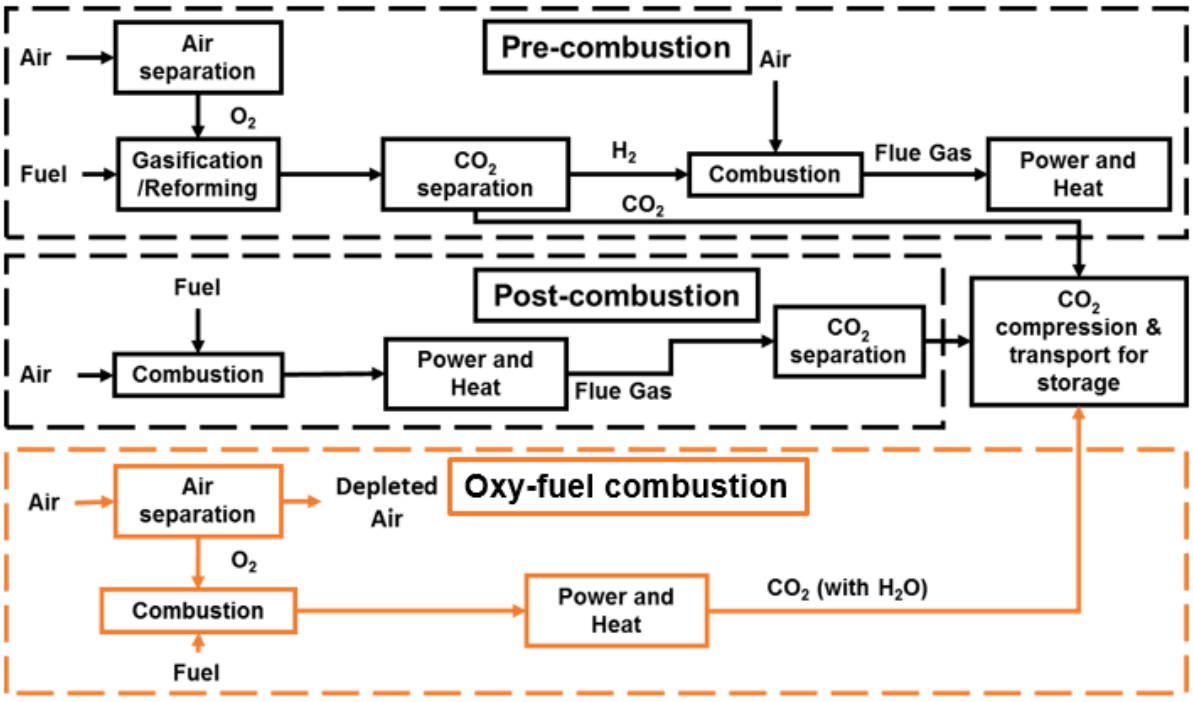

Figure 1.1 Simplified concepts of CCS processing incorporated into fossil fuel power plants

Oxy-fuel combustion is the process of using pure oxygen for fuel combustion, creating a CO_2 and H_2O enriched flue gas that can easily be separated and sequestered for future use [17–21]. As displayed in Fig. 1.2, its components include an air separation unit (ASU), a furnace, and a CO_2 capture and compression unit. Most research has focused on the development of the ASU, which supplies high volumes of pure oxygen at low energy costs. Currently, there are two methods used as ASUs for oxy-fuel combustion: cryogenic ASU and chemical looping combustion (CLC).

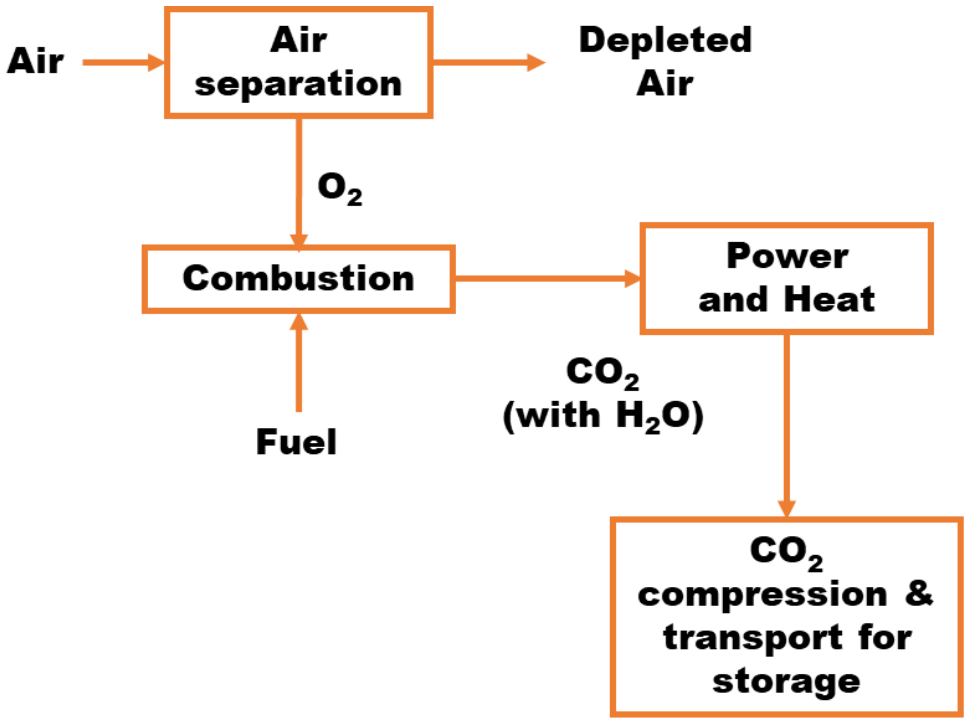

Figure 1.2 Simplified concept for oxy-fuel combustion

The first approach, cryogenic ASU, is a complicated process that primarily involves cooling and compressing air to the point of filtrating nitrogen, producing a large volume of pure oxygen to be delivered directly to the combustor. Although feasible in practice, cryogenic ASUs still require a tremendous amount of power to operate, significantly reducing plant output by 12-15% [22–24]. CLC is another method used to separate oxygen from air and deliver it to a combustor [25]. CLC involves the use of an oxygen carrier that is transported between the two reactors. In the first reactor, the metal is deoxidized to form the oxide in the presence of air. In the second reactor, the metal is reduced in the presence of the fuel. Thus direct contact between air and fuel is avoided [26]. This process, however, is arduous to ensure sufficient energy transfer from the metal re-oxidation reactor to the endothermic oxide reduction reactor, requiring the carrier to be mechanically and thermally stable [27].

An alternative solution incorporates oxygen transport membrane reactors (OTMs) to filter pure oxygen from air and deliver it directly to the fuel for the application of oxy-fuel combustion. The

filtration process occurs at high temperatures (800-900°C) when air is introduced onto one side of the OTM, while fuel is fed onto the other side. The difference in oxygen concentration across the OTM creates a chemical gradient, allowing oxygen to be separated from the surrounding air and be delivered directly to the incoming fuel, producing a nitrogen-free combustion. This permeation process attributes to the electrochemical material properties of the OTM. The heat generated from the reaction serves two purposes; (1) maintains the high temperature needed for the OTM to function, signifying no need for additional equipment; (2) is transferred back through the membrane to heat the depleted air that feeds into a turbine downstream to generate power. The exhaust gas from the turbine is then fed into a heat recovery steam generator, producing more power than an ordinary combined cycle [28]. A portion of the combustion exhaust could also feed into a "sweeping turbine" for additional power generation.

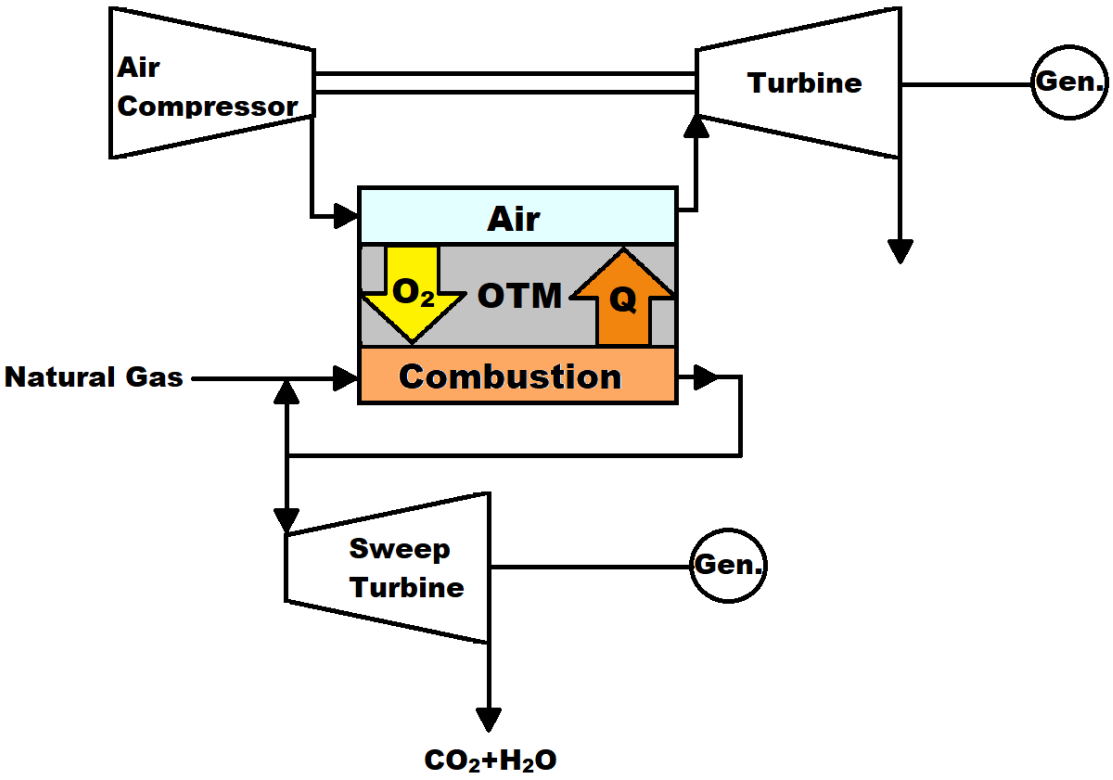

Figure 1.3 Schematic of oxygen transport membranes for oxy-fuel combustion purposes

The oxygen permeation process is achieved by adopting mixed ionic and electronic conductive perovskite structures into the OTM composition. Since the initial work of Teraoka, perovskite materials have received growing attention due to their high lattice oxygen ion mobility at elevated temperatures [29]. The ideal perovskite structure displayed in Fig. 1.4 demonstrates the chemical composition of perovskite structures: $ABO_{3-ö}$. As shown, the perovskite material centers around the B-site cation in a 12-fold coordination, with the A-site cations at the corner of the simple cubic structure (6-fold coordination), surrounded by oxygen anions are represented at the center of the cubic edges [30].

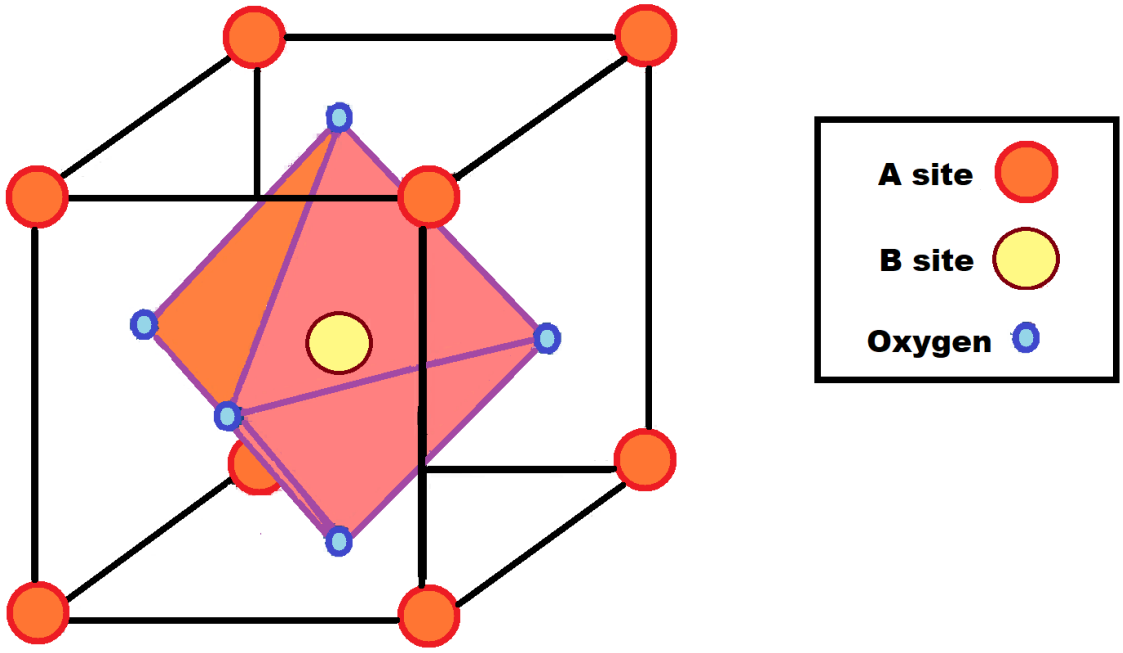

Figure 1.4 Ideal perovskite structure

A-site cations are primarily composed of alkaline earth metals or lanthanide ions, while B-site cations are mainly composed of transition metals [31]. Mixed conductivity can be achieved in the perovskite structure by the partial substitution on the A-site of a cation with a differing oxidation state relative to the initial A-site cation. The doping strategy results in the electrical neutrality becoming sustained by the formation of oxygen vacancies, which facilitates oxygen ion mobility.

Furthermore, the different oxidation state of the B-site cation allows electron hopping through the valence metals. The variation of oxygen in the perovskite structure is denoted by the oxygen nonstoichiometric coefficient (δ) in its chemical formula.

Over the past two decades, several researchers have attempted to develop new perovskite materials that exhibit a high oxygen permeation flux and excellent chemical stability [32,33]. However, for the application of oxy-fuel combustion, OTMs face several challenges that they must overcome before being implemented. Firstly, OTM performance is primarily controlled by its material composition which requires substantial experimental investigation, signifying the need for developing a computational model that evaluates the oxygen permeation performance of perovskite-type structures. Secondly, OTMs have been utilized for the partial oxidation of methane to produce syngas, but there has been little work confirming the feasibility of OTMs as simultaneous separation and methane combustion units [34–38]. Thirdly, perovskite structures have been previously discovered to exhibit poor chemical stability under high concentrations of CO_2, threatening the legitimacy of OTMs [39–42]. An alternative to developing new CO_2-tolerant materials are dual-phase OTMs which combine a high performing perovskite material with a CO_2-tolerant additive to maintain high oxygen permeability and chemical stability. Lastly, current experimental research significantly lacks standard methods for evaluating OTMs for the application of oxy-fuel combustion. If OTMs are to be implemented to mitigate CO_2 emissions, there must be a developed methodology that utilizes material science and combustion findings, further connecting this interdisciplinary research.

1.2 Objectives

A series of single and dual-phase OTMs were synthesized to evaluate their oxygen permeation performance and potential application for oxy-fuel combustion. Specifically, the material

properties of the overall membrane were studied including phase structure, morphology, chemical stability, total conductivity (ionic and electronic conductivity), diffusivity, and the oxygen permeability performance under varying surrounding conditions. The objectives of this thesis were as follows:

1. Identify and compare the oxygen diffusivity (ionic conductivity) results obtained from experimental and computational methods
2. Study the oxygen permeation performance of single phase OTMs for methane combustion
3. Investigate the oxygen permeability and chemical stability of single and dual-phase OTMs subjected to potentially degrading environments (CO_2 rich atmospheres)
4. Determine the material properties and oxygen permeation performance of dual-phase OTMs for the application of oxy-fuel combustion
5. Develop a simplified methodology that evaluates OTM performance on an experimental level while establishing a standard for the application of oxy-fuel combustion

1.3 Research Scope

The scope of this work consists of three major components:

First, the diffusivity and oxygen permeation performance of a perovskite-type material were determined using experimental and computational methods. Due to its demonstrated higher oxygen permeation performance and chemical stability, $SrSc_{0.1}Co_{0.9}O_{3-ö}$ (SSC) was the selected material used in these studies [43–45]. SSC OTM samples were fabricated using a dry pressing technique. SSC diffusivity was determined using electronic conductivity relaxation technique (ECR) and thermogravimetric analysis (TGA). Simultaneously, a molecular dynamics simulation (MDS) of SSC was developed to determine the oxygen ion diffusivity through the perovskite-type material. Furthermore, the oxygen permeation performance was investigated under similar

conditions to those used for oxy-fuel combustion (e.g., high membrane temperatures and sweeping gas flow rates).

Second, the material properties and performance of dual-phase OTMs were evaluated by modifying the weight ratio between SSC and a CO_2-tolerant additive material. A doped-ceria material, specifically $Sm_{0.2}Ce_{0.8}O_{1.9-ö}$ (SDC), was selected as the stable additive material because of their thermal compatibility with perovskite-type structures, high ionic conductivity, and reported high tolerance to acidic gases, such as CO_2 [46–49]. Several properties were investigated pre- and post-exposure to CO_2. Morphology properties including phase structure and chemical stability of the mixed materials were determined by X-ray diffraction (XRD) and Scanning Electronic Microscopy (SEM). Total conductivity was measured by a four-probe D.C. method. The oxygen permeability characterized by permeation measurements in different atmospheres under varying temperature, surrounding oxygen concentrations, and sweeping gas compositions (e.g., helium, methane, CO_2).

Third, to combine material science and combustion approaches used to investigate the oxygen permeation performance, a methodology for estimating the total oxygen permeation flux of OTMs from standard permeation experiments was developed. A high performing dual-phase OTM was used to investigate the oxygen permeation flux using a methane/CO_2 sweeping gas at different membrane temperatures and sweeping gas flow rates. These results were then fitted to estimate the average oxygen permeation flux and provides an approximate OTM size needed to perform a complete combustion.

1.4 Dissertation Organization

Chapter 1 introduces the general background and motivation for implementing OTMs for the application of oxy-fuel combustion. A summary of lagging research is identified supporting the listed objectives and research scope of this dissertation.

Chapter 2 is a literature review of previous work that further supports the methods and findings presented in this dissertation. The major topics in this section include oxygen permeation fundamentals, current material developments, membrane stability in acidic environments, and OTMs' current and potential applications. Research gaps in the existing literature are also detailed, further supporting the pursuit of this work.

Chapter 3 reports the oxygen diffusivity through an SSC perovskite structure at varying temperatures using MDS and experimental analysis. MDS determines the oxygen diffusivity by investigating the interaction between each ion in the perovskite structure using an empirical potential function. Experimentally, the oxygen diffusivity is determined using conductivity relaxation methods. Findings from the computational and experimental methods are compared suggesting a new approach in the development of new perovskite materials.

Chapter 4 focuses on the performance of a perovskite-type SSC and $La_{0.6}Sr_{0.4}C_{0.2}Fe_{0.8}O_{3-\delta}$ (LSCF) OTMs for methane combustion under various conditions. These conditions include membrane temperature, sweeping gas flow rate, and material composition. Key trends that impact the oxygen permeation flux are identified, laying the foundation for implementing OTMs for the application of oxy-fuel combustion.

Chapter 5 studies the material properties of dual-phase OTMs when exposed to CO_2 atmospheres. The membranes chemical structure, morphology, total conductivity, and oxygen permeation performance are evaluated experimentally and compared pre- and post-CO_2 exposure.

Chapter 6 offers further insight into the performance of dual-phase OTMs for methane combustion. A detailed understanding of ion mobility in composite materials relative to single phase membranes is provided. Other membrane characteristics of dual-phase compositions such as chemical structure, total conductivity, and morphology are also reported.

Chapter 7 presents a new methodology for predicting the overall oxygen permeation performance of an OTM composition using established experimental methods. An innovative and resilient composite OTM is investigated under varying sweeping gas compositions, to simulate the different gas compositions that occur as a fuel stream moves across an OTM. The oxygen permeation flux results are compiled to establish a relationship between permeation performance and methane concentrations. The data also provide further insight into the OTM design parameters needed for a complete oxy-fuel combustion.

Chapter 8 summarizes the discoveries from these works and key findings that may prove significant for implementing OTMs for the application of oxy-fuel combustion. Additionally, based on this work's conclusions, recommendations are presented that suggest future research endeavors that improve the potential for OTMs to become a reality.

Chapter 2 Literature Review

2.1 Introduction

Since their initial development, oxygen transport membranes reactors (OTMs) have become one of the most promising technologies to produce large volumes of oxygen at high temperatures [50]. Already there have been several studies that highlight OTM utilization over cryogenic distillation process for oxy-fuel combustion [22,51,52]. As previously stated in Chapter 1, OTMs have an advantage over other technologies because of its capture and combustion performance at low energy costs [28].

OTMs oxygen semi-permeability attributes to the partial substitution in the A and B cations sites of the perovskite lattice structure, which facilitate the formation of oxygen vacancies via defect reactions. The OTM provides an oxygen permeation flux when exhibiting oxygen vacancies throughout its membrane structure. The creation of oxygen vacancies is achieved by maintaining high membrane temperatures ($\geq$800°C). Therefore, OTMs require a substantial heating source to be utilized for oxy-fuel combustion.

When applied as a reactor for oxy-fuel combustion, OTMs can simultaneously act as an air separation and combustion unit, providing the heat needed to maintain an oxygen permeation flux as well as generate power. As shown in Fig. 2.1, if the OTM can initially achieve a high temperature from the heated air on the feed side, fuel (i.e., methane) can be introduced onto one side of the OTM, creating an oxygen chemical gradient across the membrane. The oxygen chemical gradient allows oxygen to permeate through the membrane and be delivered to the fuel. The permeated oxygen can then react with the incoming fuel producing a high temperature, nitrogen-free, and rich CO_2 exhaust stream. The heat produced from the reaction can then be used

to generate power, and more importantly to sustain the membrane temperature needed to maintain an oxygen permeation flux.

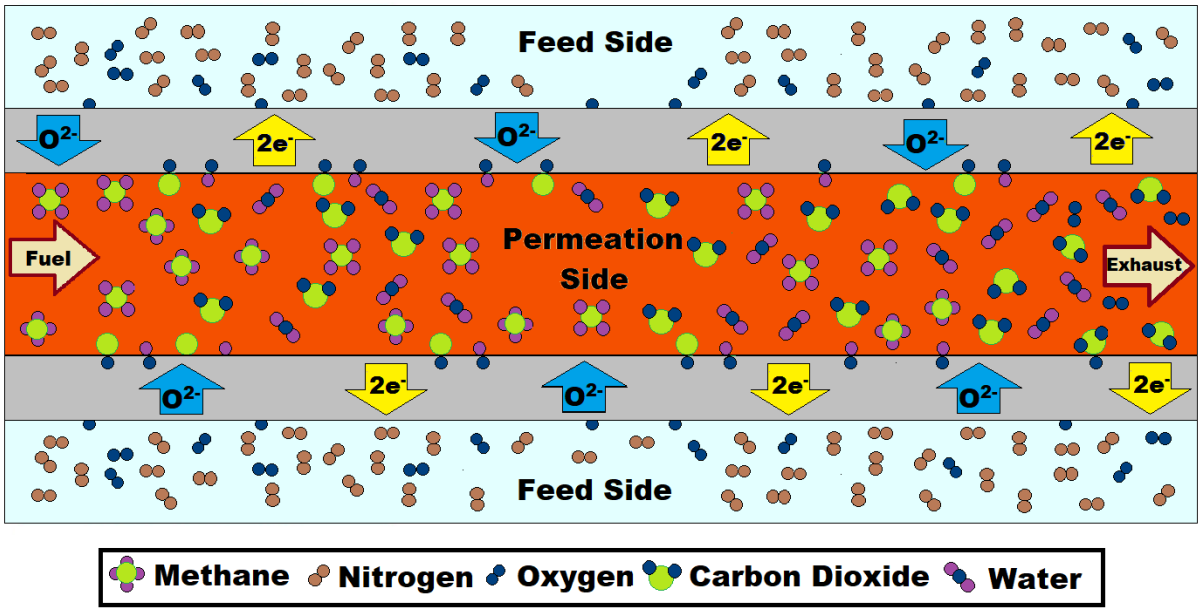

Figure 2.1 Schematic of OTM utilized for the application of oxy-fuel combustion

If OTMs are to become a reality eventually, several challenges need to be overcome. These challenges include ensuring the OTM exhibits a high oxygen permeation flux and maintains mechanical and chemical stability under all operating conditions. In summary, OTMs legitimacy depends on its lasting performance and durability, which directly relate to its material properties.

2.2 Understanding the oxygen transport through the membrane

The mixed ionic and electronic conductivity (MIEC) of perovskite materials is the basis for oxygen permeability. The ionic conductivity of the perovskite material accounts for oxygen ion mobility through vacancies within the membrane. The electron conductivity of the perovskite-type material enhances the materials catalytic ability towards oxygen reduction on the surface. The conductive properties of the OTM can be enhanced by doping low valence cations on the A or B site, facilitating the formation of oxygen vacancies. When exposed to oxygen at high temperatures,

the oxygen vacancies on the perovskite structure become occupied with oxygen ions and are then charge compensated by the presence of two electron holes. Equation 2.1 details this phenomenon in Kröger-Vink notation where $V_{\ddot{O}}$ is the oxygen vacancy, O_O^X is the occupied oxygen vacancy, $h^{\cdot}$ is the electron holes, and k_f and k_r are the forward and reverse reaction rates, respectively.

$$\frac{1}{2}O_2 + V_{\ddot{O}} \overset{k_f/k_r}{\longleftrightarrow} O_O^X + 2h^{\cdot} \qquad \text{(Eq. 2.1)}$$

As seen from Fig. 2.1 and described in Eq. 2.1, ionic mobility is charge compensated by the transport of electrons in the reverse direction. However, most perovskite materials have a substantially smaller ionic conductivity than electronic conductivity because of the higher mobility in the electron carriers compared to the ionic carriers within the perovskite structure [53]. Therefore, the ionic mobility within the perovskite material is a substantial factor in the membranes oxygen permeation performance.

2.3 Oxygen permeation process

Figure 2.2 breaks down the oxygen permeation process, detailing the ionic and electronic transport driven by the oxygen partial pressure gradient across the membrane.

Step 1) The membrane is heated to an elevated temperature where a sweeping gas (i.e., fuel) is introduced to one side of the membrane, creating an atmosphere with little to no concentration of oxygen. The opposing side is exposed to an atmosphere with a high concentration of oxygen (i.e., air). The major difference in the oxygen concentration creates a significant oxygen partial pressure gradient across the entire membrane.

Step 2) Motivated by the partial pressure gradient, gaseous oxygen on the feed side of the membrane approaches the membrane surface (advection and diffusion).

Step 3) Oxygen molecules are adsorbed onto the membrane surface where they begin to dissociate and ionize into oxygen ions. Oxygen ions begin to fill oxygen vacancies performing a surface exchange reaction (Eq. 2.1) on the feed side.

Step 4) Oxygen ions transfer through the membrane via bulk diffusion and are charge compensated by electrons moving through electron holes in the reverse direction.

Step 5) Oxygen ions reach the permeation side where they are re-oxidized via surface exchange reaction (Eq. 2.1), leaving the remaining electrons to transfer back through the membrane via electron holes.

Step 6) Oxygen molecules then feed into the sweeping gas stream and react with the incoming fuel (advection and diffusion).

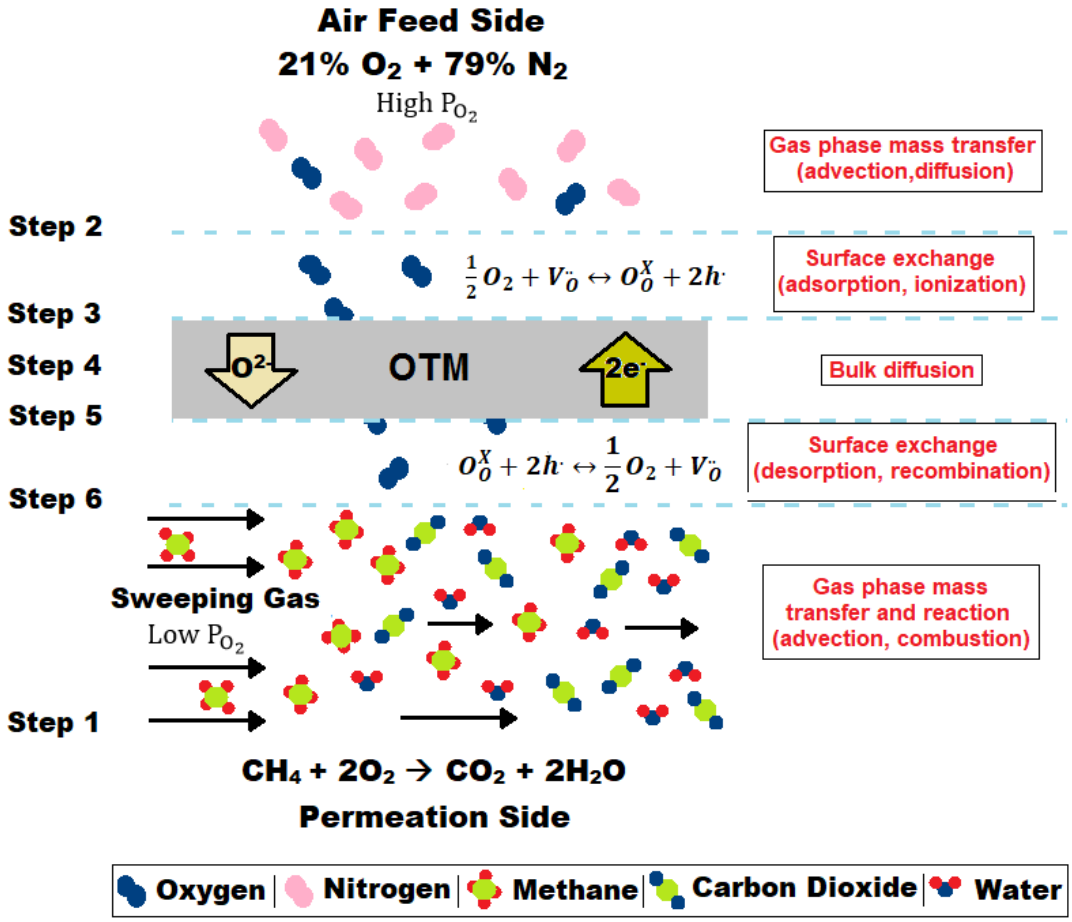

Figure 2.2 Steps for oxygen transport through OTM

The oxygen permeation process is limited by the materials properties of the membrane. More specifically, the resistance of the permeation process is constrained by the surface exchange on the air feed side (i.e., adsorption and ionization), the bulk diffusion of the oxygen ions through the OTM, and the surface exchange on the permeation side (i.e., desorption and recombination). When the oxygen permeation flux reaches a relatively stable state, the slowest step determines the overall oxygen transport through the OTM. For example, thick membranes are limited by bulk diffusion since the surface exchange reaction occurs at a faster rate, whereas in thin membranes the bulk diffusion is faster, leaving the surface exchange rate on both sides of the OTM to limit the permeation performance. In most experiments, to ensure a robust mechanical integrity, OTMs are typically thick, signifying that bulk diffusion limits the permeation flux.

The relation between the oxygen permeation flux ($\mathbf{J_{O_2}}$) and bulk diffusion can be described using the Wagner's model [54]. This model assumes the membrane is under steady-state conditions and is detailed in Eq. 2.2:

$$J_{O_2} = -\frac{RT}{16F^2L}\int_{lnpO_2''}^{lnpO_2'} \frac{\sigma_e\sigma_{ion}}{\sigma_e+\sigma_{ion}} \cdot \partial \ln(pO_2) \qquad \text{(Eq. 2.2)}$$

where σ_{ion} and σ_e are the ionic and electronic conductivities, respectively, L is the thickness of the membrane, R is the universal gas constant, F is Faraday's constant, T is the absolute temperature and pO_2' and pO_2'' is the partial pressure of oxygen on the air feed and permeation side, respectively.

As previously stated, the ionic mobility is usually far less than the electronic mobility due to the superior electronic carries in the perovskite structure ($\sigma_e \gg \sigma_{ion}$) [53]. This simplifies Wagner's equation to:

$$J_{O_2} = -\frac{RT}{16F^2L}\int_{lnpO_2''}^{lnpO_2'} \sigma_{ion} \cdot \partial \ln(pO_2) \qquad \text{(Eq. 2.3)}$$

Assuming a constant ionic conductivity throughout the entire OTM and identifying the difference of the oxygen partial pressure across the membrane as the chemical potential gradient through the bulk ($\Delta\mu_{O_2} = \mathrm{RT}\int_{\ln pO_2''}^{\ln pO_2'} \partial \ln(pO_2)$), Eq. 2.3 can be further reduced to:

$$J_{O_2} = -\frac{\sigma_{ion}}{16F^2L}\Delta\mu_{O_2} \qquad \text{(Eq. 2.4)}$$

Equation 2.4, also known as the Nernst-Planck equation, shows that the ionic conductivity and the oxygen chemical gradient across the membrane directly improve the oxygen permeation flux. Equation 2.4 also demonstrates the influence of the membrane thickness (L) which is shown to diminish the oxygen permeation flux as the membrane thickness increases.

Theoretically, Eq. 2.4 could be used to approximate the oxygen permeation flux if bulk diffusion limited the membrane's performance. However, the ionic conductivity is extremely difficult to measure experimentally but can be determined by identifying the perovskite materials oxygen diffusivity. Looking at Nernst-Einstein relationship (Eq. 2.5), the ionic conductivity relative to the average oxygen diffusion coefficient (D_O) is shown as:

$$\sigma_{ion} = \frac{4F^2C_OD_O}{RT} \qquad \text{(Eq. 2.5)}$$

where (C_O) average molar concentration of oxygen residing vacancies in the perovskite structure. This equation considers the diffusion coefficient over a range of pO_2 throughout the entire membrane structure which is challenging to estimate at local areas residing within the OTM. The average oxygen diffusion coefficient relates to the oxygen chemical diffusion coefficient by a thermodynamic factor as shown in Eq. 2.6:

$$D_{Chem} \approx D_O\frac{\partial \ln(pO_2)}{2\partial \ln(C_O)} \qquad \text{(Eq. 2.6)}$$

The oxygen chemical diffusion coefficient (D_{Chem}) is the oxygen ion mobility at varying pO_2 atmospheres. D_{Chem} can be found from ECR while the thermodynamic factor depicted in Eq. 2.6

can be obtained experimentally from a TGA, resulting in an experimental method to determine the ionic conductivity [55–57].

Despite its novelty, the model presented in Eq. 2.4 does not always directly correspond to the oxygen permeation flux. Previous literature has derived a characteristic thickness (L_c), in which the oxygen permeation flux transitions from being limited by the bulk diffusivity to the surface exchange reactions [37,58,59]. For perovskite materials in which the ionic conductivity is significantly smaller than the electronic conductivity, the characteristic thickness is the ratio between the average oxygen diffusion coefficient and the surface exchange coefficient (K_{ex}):

$$L_c = \frac{D_O}{K_{ex}} \qquad \text{(Eq. 2.7)}$$

As OTM research developed further to produce thinner membranes using a porous catalyst supports, there was a greater need for developing an all-encompassing OTM model that accounts for the bulk diffusion and surface exchange reactions on both sides of the membrane. The surface exchange reactions, previously described in Eq. 2.1, represent the ionization and re-oxidation of oxygen on the feed and permeation side of the membrane, respectively. The dynamic equilibrium equations of the surface exchange reactions, by the law of mass action, can be written as:

$$J_{O_2} = k_f (pO_2')^{0.5} C_O{}' - k_r \left[O_O^{X'}\right][2h^{\cdot}]^2 \qquad \text{(Eq. 2.8)}$$

$$J_{O_2} = k_r \left[O_O^{X''}\right][h^{\cdot\prime}]^2 - k_f (pO_2'')^{0.5} C_O{}'' \qquad \text{(Eq. 2.9)}$$

In previous research, the reverse reaction has been assumed to be independent of the concentration of oxygen and electron holes at steady state, meaning Eq. 2.8 and 2.9 reduce to:

$$J_{O_2} = k_f \left(pO_2^{'}\right)^{0.5} C_O{}' - k_r^o \qquad \text{(Eq. 2.10)}$$

$$J_{O_2} = k_r^o - k_f (pO_2^{''})^{0.5} C_O{}'' \qquad \text{(Eq. 2.11)}$$

where k_r^o is the zero-order reverse reaction rate constant [60]. A relationship between the oxygen partial pressure and the vacancy concentration that influences the oxygen permeation flux is observed from Eq. 2.10 and 2.11. The consideration presented here attributes to the presence of oxygen ions within the lattice structure to the driving force behind the oxygen permeation flux. Furthermore, Eq. 2.10 and 2.11 differ from Eq. 2.4, by considering the partial pressure gradient across the membrane to the oxygen ions mobility from the air to permeation side.

The ionic mobility of oxygen through the membrane has been represented using the Nernst-Einstein relation (Eq. 2.5) but does not necessarily represent ion mobility through oxygen vacancies within the perovskite structure. The vacancy flux (J_V) can be described by transforming the Nernst-Planck equation (Eq. 2.4) and using the correlation between the chemical potential gradient and the concentration of oxygen vacancies ($\Delta\mu_{O_2} = RT\Delta \ln C_O$) resulting in:

$$J_V = -D_O \frac{\partial C_O}{\partial x} \qquad \text{(Eq. 2.12)}$$

Considering that the oxygen permeation flux is double of the negated vacancy flux ($J_{O_2} = -\frac{1}{2}J_V$), the new relation between the bulk diffusion and oxygen permeation flux is written as follows:

$$J_{O_2} = \frac{D_O}{2L}(C_O^{''} - C_O^{'}) \qquad \text{(Eq. 2.13)}$$

Through a combination of Eq. 2.10, 2.11, 2.13, the oxygen permeation flux is represented as:

$$J_{O_2} = \frac{D_O k_r^o\left(\left(pO_2^{'}\right)^{0.5} - \left(pO_2^{''}\right)^{0.5}\right)}{2Lk_f\left(pO_2^{'}pO_2^{''}\right)^{0.5} + D_O\left(\left(pO_2^{'}\right)^{0.5} + \left(pO_2^{''}\right)^{0.5}\right)} \qquad \text{(Eq. 2.14)}$$

Equation 2.14 is an oxygen permeation flux model that combines the resistances of the bulk diffusion and surface exchange reactions on the feed and permeation side. To quantitively determine the permeation resistance of the bulk diffusion and both surface exchange kinetics, Eq. 2.14 can be broken down into three separate components. This can be achieved by identifying the

surface exchange coefficient at the feed and permeation, as a relation between the oxygen permeation flux and the difference in the oxygen vacancy concentrations relative to their equilibrium state:

$$J_{O_2} = k'_{ex}\left(C'_O - C'_{O,eq}\right) \quad \text{(Eq. 2.15)}$$

$$J_{O_2} = k''_{ex}\left(C''_{O,eq} - C''_O\right) \quad \text{(Eq. 2.16)}$$

In comparison to Eq. 2.10 and 2.11, the surface exchange coefficients on the feed and permeation side directly relate to the forward surface exchange coefficient and partial pressure on the respective membrane side. Therefore:

$$k'_{ex} = k_f(pO'_2)^{0.5} \quad \text{(Eq. 2.17)}$$

$$k''_{ex} = k_f(pO''_2)^{0.5} \quad \text{(Eq. 2.18)}$$

Using these two equations, Eq. 2.14 can be re-written as:

$$J_{O_2} = \frac{\frac{k_r}{k_f}\left((pO''_2)^{-0.5} - (pO'_2)^{-0.5}\right)}{\frac{1}{k'_{ex}} + \frac{2L}{D_O} + \frac{1}{k''_{ex}}} = \frac{\Delta(pO_2)}{R'_{ex} + R_{diff} + R''_{ex}} = \frac{\Delta(pO_2)}{R_t} \quad \text{(Eq. 2.19)}$$

where $\Delta(\mathrm{pO_2}) = (\mathrm{k_r/k_f})((\mathrm{pO''_2})^{-0.5} - (\mathrm{pO'_2})^{-0.5})$ is the pressure driving force across the membrane, $\mathrm{R_t}$ is the total permeation resistance broken down into the bulk diffusion resistance ($\mathrm{R_{diff} = 2L/D_o}$) and the surface exchange resistance ($\mathrm{R'_{ex} + R''_{ex}}$) on the feed ($\mathrm{R'_{ex} = 1/k'_{ex} = 1/k_f(pO'_2)^{0.5}}$) and permeation sides ($\mathrm{R''_{ex} = 1/k''_{ex} = 1/k_f(pO''_2)^{0.5}}$). The value in the numerator can be identified as the driving oxygen partial pressure difference across the entire membrane $\Delta(\mathrm{pO_2})$. If any one of these steps is determined to be the rate limiting steps, then Eq. 2.19 is dominated by the corresponding resistance, as simplified to one of the following three equations:

Rate determined by surface exchange kinetics on the feed side:

$$J_{O_2} = \frac{\Delta(pO_2)}{R'_{ex}} = k_r \left[\left(\frac{(pO'_2)}{(pO''_2)} \right)^{0.5} - 1 \right] \quad \text{(Eq. 2.20)}$$

Rate determined by bulk diffusion:

$$J_{O_2} = \frac{\Delta(pO_2)}{R_{diff}} = \frac{D_O k_r}{2Lk_f} [(pO''_2)^{-0.5} - (pO'_2)^{-0.5}] \quad \text{(Eq. 2.21)}$$

Rate determined by surface exchange kinetics on the permeation side:

$$J_{O_2} = \frac{\Delta(pO_2)}{R''_{ex}} = k_r \left[1 - \left(\frac{(pO''_2)}{(pO'_2)} \right)^{0.5} \right] \quad \text{(Eq. 2.22)}$$

These equations can be used to predict the oxygen permeation performance based on the dominant rate-limiting step. For example, if the permeation process is determined to be limited by bulk diffusion (Eq. 2.20), an increase in the oxygen partial pressure on the feed side would improve the oxygen permeation flux. If the exchange kinetics constrains the permeation performance on the oxygen permeation side, then a decrease in the oxygen partial pressure on the permeation side would improve the oxygen permeation flux. Several researchers have been able to fit experimentally determined oxygen permeation fluxes using this model [60,61]. In some cases, to preserve the mechanical integrity of the OTM, the membrane thickness is larger than the characteristic thickness, signifying that bulk diffusion is the rate-limiting step.

2.4 Current developments of OTMs with high oxygen permeation flux

2.4.1 Perovskite structure's influence on oxygen permeability

Although these equations are helpful in predicting the oxygen permeation flux under varying partial pressures, the membrane's performance is primarily governed by the average oxygen diffusion (D_O) and surface exchange coefficients (k_r and k_f). These parameters are mainly functions of temperature, directly improving the oxygen permeability with an increase in the

membrane temperature. Another method for improving these parameters is through doping strategies to advance the mixed conductivity of the perovskite structure.

As previously stated, A-site cations are typically occupied by large alkali earth metals (e.g., La, Ba, or Sr) while the B-site is comprised of smaller transition metal ions with different valence states (e.g., Co or Fe). Atoms on the A-site tend to determine the concentration of vacancies within the lattice structure by their larger atomic radii which cause distortion effects in the perovskite structure [62]. B-site atoms control the ionic and electronic mobility that preserve the charge neutrality as ions move through the structure [63,64]. As shown in Table 2.1, researchers have explored a wide variety of materials that further enhance the distortion and mixed ionic and electronic conductivity of perovskite structure. Much of the current research has focused on $Ba_{1-x}Sr_xFe_{1-y}Co_yO_{3-\delta}$ or $La_{1-x}Sr_xFe_{1-y}Co_yO_{3-\delta}$ with some varying combinations of other elements on the A or B-site to either improve performance/conductivity or stability. Table 2.1 lists the oxygen permeation performance of some perovskite oxides.

Table 2.1 Summary of MIEC membrane oxygen permeation flux performances

Composition	Temperature (°C)	Oxygen Permeation Flux at given temperature ($ml.min^{-1}.cm^{-2}$)	Shape	Thickness (mm)	Sweeping Gas	Ref
$BaBi_{0.5}Co_{0.2}Fe_{0.3}O_{3-\delta}$	800-925	0.37-0.75	Disk	1.5	Helium	[65]
$BaBi_{0.4}Co_{0.2}Fe_{0.4}O_{3-\delta}$	800-925	0.41-0.80	Disk	1.5	Helium	[65]
$BaBi_{0.2}Co_{0.2}Fe_{0.6}O_{3-\delta}$	800-925	0.27-0.75	Disk	1.5	Helium	[65]
$BaCe_{0.4}Fe_{0.6}O_{3-\delta}$	800-950	0.10-0.24	Disk	1-1.5	Helium	[66]
$BaCe_{0.2}Fe_{0.8}O_{3-\delta}$	800-950	0.13-0.39	Disk	1-1.5	Helium	[66]
$BaCe_{0.15}Fe_{0.85}O_{3-\delta}$	800-950	0.23-0.52	Disk	1-1.5	Helium	[66]
$BaCo_{0.4}Fe_{0.5}Zr_{0.1}O_{3-\delta}$	700-950	0.26-0.92	Disk	1	Helium	[42]
$Ba_{0.5}Sr_{0.5}Co_{0.8}Fe_{0.2}O_{3-\delta}$	850-950	0.12-2.10	Disk	1.8	Helium	[42]
$Ba_{0.5}Sr_{0.5}Co_{0.8}Fe_{0.2}O_{3-\delta}$	850-950	1.89-4.39	Tube	0.22	Helium	[67]
$BaTi_{0.2}Co_{0.4}Fe_{0.4}O_{3-\delta}$	600-950	0.00-0.65	Disk	1 to 2	Helium	[68]
$BaTi_{0.2}Co_{0.5}Fe_{0.3}O_{3-\delta}$	600-950	0.00-0.9	Disk	1 to 2	Helium	[68]
$Gd_{0.6}Sr_{0.4}CoO_{3-\delta}$	820	1.58	Disk	1.5	Helium	[69]
$La_{0.6}Ba_{0.4}Co_{0.8}Fe_{0.2}O_{3-\delta}$	860	2.06	Disk	1.5	Helium	[69]
$La_{0.4}Ba_{0.6}Co_{0.2}Fe_{0.8}O_{3-\delta}$	900	0.72	Disk	0.55	Helium	[70]

Composition	Temperature (°C)	Oxygen Permeation Flux at given temperature ($ml.min^{-1}.cm^{-2}$)	Shape	Thickness (mm)	Sweeping Gas	Ref
$La_{0.6}Ca_{0.4}Co_{0.8}Fe_{0.2}O_{3-\delta}$	860	1.83	Disk	1.5	Helium	[69]
$La_{0.4}Ca_{0.6}Co_{0.2}Fe_{0.8}O_{3-\delta}$	900	0.19	Disk	0.55	Helium	[71]
$LaCo_{0.8}Fe_{0.2}O_{3-\delta}$	860	0.02	Disk	1.5	Helium	[69]
$La_{0.6}Na_{0.4}Co_{0.8}Fe_{0.2}O_{3-\delta}$	860	0.27	Disk	1.5	Helium	[69]
$La_{0.6}Sr_{0.4}CoO_{3-\delta}$	870	0.51	Disk	1	Helium	[44]
$La_{0.6}Sr_{0.4}CoO_{3-\delta}$	850	0.54	Disk	0.24-1.3	Helium	[72]
$La_{0.6}Sr_{0.4}CoO_{3-\delta}$	850	0.02	Disk	1	Helium	[73]
$La_{0.6}Sr_{0.4}CoO_{3-\delta}$	820-860	0.72	Disk	1.5	Helium	[69]
$La_{0.6}Sr_{0.4}Co_{0.8}Cr_{0.2}O_{3-\delta}$	860	0.57	Disk	1.5	Helium	[69]
$La_{0.6}Sr_{0.4}Co_{0.8}Cu_{0.2}O_{3-\delta}$	860	1.90	Disk	1.5	Helium	[69]
$La_{0.6}Sr_{0.4}Co_{0.2}Fe_{0.8}O_{3-\delta}$	850-900	0.05-0.14	Tube	0.219	Argon	[74]
$La_{0.6}Sr_{0.4}Co_{0.4}Fe_{0.6}O_{3-\delta}$	1000-1100	0.03-0.17	Disk	1	Helium	[30]
$La_{0.6}Sr_{0.4}Co_{0.8}Fe_{0.2}O_{3-\delta}$	860	0.62	Disk	1.5	Helium	[69]
$La_{0.4}Sr_{0.6}Co_{0.2}Fe_{0.8}O_{3-\delta}$	900	0.11	Disk	0.55	Helium	[30]
$La_{0.2}Sr_{0.8}Co_{0.4}Fe_{0.6}O_{3-\delta}$	1000-1100	0.17-0.50	Disk	1	Helium	[30]
$La_{0.6}Sr_{0.4}Co_{0.8}Mn_{0.2}O_{3-\delta}$	860	0.50	Disk	1.5	Helium	[69]
$La_{0.6}Sr_{0.4}Co_{0.8}Ni_{0.2}O_{3-\delta}$	860	1.45	Disk	1.5	Helium	[69]
$La_{0.9}Sr_{0.1}FeO_{3-\delta}$	1000	0.03	Disk	1	Helium	[70]
$La_{0.8}Sr_{0.2}FeO_{3-\delta}$	1000	0.13	Disk	1	Helium	[70]
$La_{0.7}Sr_{0.3}FeO_{3-\delta}$	1000	0.22	Disk	1	Helium	[70]
$La_{0.6}Sr_{0.4}FeO_{3-\delta}$	1000	0.35	Disk	1	Helium	[70]
$La_{0.8}Sr_{0.2}Ga_{0.7}Co_{0.3}O_{3-\delta}$	700-1000	0.31-1.48	Disk	0.5	Methane	[75]
$La_{0.8}Sr_{0.2}Ga_{0.7}Fe_{0.3}O_{3-\delta}$	700-1000	0.59	Disk	0.5	Methane	[75]
$La_{0.8}Sr_{0.2}Ga_{0.7}Ni_{0.3}O_{3-\delta}$	700-1000	0.35	Disk	0.5	Methane	[75]
$Nd_{0.6}Sr_{0.4}CoO_{3-\delta}$	820	1.03	Disk	1.5	Helium	[69]
$Pr_{0.6}Sr_{0.4}CoO_{3-\delta}$	820	0.93	Disk	1.5	Helium	[69]
$Sm_{0.6}Sr_{0.4}CoO_{3-\delta}$	820	1.19	Disk	1.5	Helium	[69]
$Sr_{0.5}Bi_{0.5}FeO_{3-\delta}$	825-925	0.17-0.54	Disk	1	Argon	[76]
$SrCoO_{3-\delta}$	850-1000	0.00-0.45	Disk	1	Helium	[73]
$SrCo_{0.8}Fe_{0.2}O_{3-\delta}$	850	0.23	Disk	1	Helium	[73]
$SrCo_{0.8}Fe_{0.2}O_{3-\delta}$	780-850	0.11-0.73	Disk	1-5.5	Helium	[77]
$SrCo_{0.8}Fe_{0.2}O_{3-\delta}$	850-950	0.87-1.25	Disk	1.5	Helium	[42]

As seen in Table 2.1, most of the reported performance of membranes fall below 1 $ml.min^{-1}.cm^{-2}$, signifying a lack of high performing perovskite materials. Furthermore, many of the developed materials that exhibit a high oxygen permeation flux (>1 $ml.min^{-1}.cm^{-2}$) do so at the

expense of chemical stability or mechanical strength, which are both important factors when implementing this technology for the application of oxy-fuel combustion [78,79].

2.4.2 Oxygen permeation performance in CO_2 environments

In addition to the lack of materials with a high oxygen permeation flux, OTMs face another significant challenge that threatens their legitimacy. Looking back at Fig. 2.1, it is clear to see that incoming fuel will react as it moves through the reactor, creating a rich product stream, primarily comprised of CO_2. However, since the A-site of perovskite-type oxide is alkaline-earth element, it has the potential to react with CO_2 to form a carbonate [80]. The formation of carbonates could severely damage the membrane by modifying the material's structure and conductive properties, that results in a poor oxygen permeation performance [81,82]. There has been some initial work to develop single crystal structures that can maintain chemical stability in CO_2 enriched environments, but at the expense of the membrane's oxygen permeation performance using inert or fuel sweeping gases [41,83–95]. Alternatively, dual-phase membranes are an innovative solution to deliver a high oxygen permeation flux throughout the entire OTM while exhibiting CO_2 tolerability further downstream.

Dual-phase membranes are comprised of two materials with different atomic structures, ionic and electronic conductive properties and resistances towards destructive gases. For instance, a dual-phase membrane that combines a mixed ionic and electronic conductive perovskite material with an exclusively ionic conductive material can transport oxygen ions through both membrane materials while carrying remaining electrons back entirely through the perovskite material (Fig. 2.3, left side). If the exclusively ionic conductive material exhibits a high resistivity towards acidic gases, oxygen ions would still be able to transport through the membrane, as long as electron pathways are present. Potentially, after the formation of carbonates on the A-site, the modified

perovskite-type structure could still conduct electrons through the -O-B-O-B-O- pathways, due to the B-site ions forming oxides and exhibiting high electronic conductive properties [83,96,97]. This suggests that the addition of a stable ionic conductive material to a perovskite composition could permit OTMs to function in both inert (e.g., helium) and acidic (e.g., CO_2) environments (Fig. 2.3, right side).

In most instances, dual-phase OTMs have implemented doped-ceria materials as the stable additive to maintain the oxygen permeation performance in acidic environments [49,84,89,98–112]. Doped ceria materials, such as $Sm_{0.2}Ce_{0.8}O_{1.9-\delta}$ (SDC) or $Sm_{0.1}Ce_{0.9}O_{2.0-\delta}$, have been used as additional electrolyte layers in solid oxide fuel cells (SOFCs) mainly due to their high ionic conductivity and thermal compatibility with SOFC cathode materials (perovskite structure) [46–49,113]. An alternative to zirconia materials are doped ceria materials which have a fluorite-type cubic structure that is complementary to the SSC perovskite-type material; the lattice constants for SDC/GDC and SSC creates a coherent interface between both materials [114]. Most importantly SDC has been shown to have no interaction and high tolerance to acidic gases (i.e., CO_2 sweeping gases) making it a prime candidate for an additive material to OTM [107,109,112].

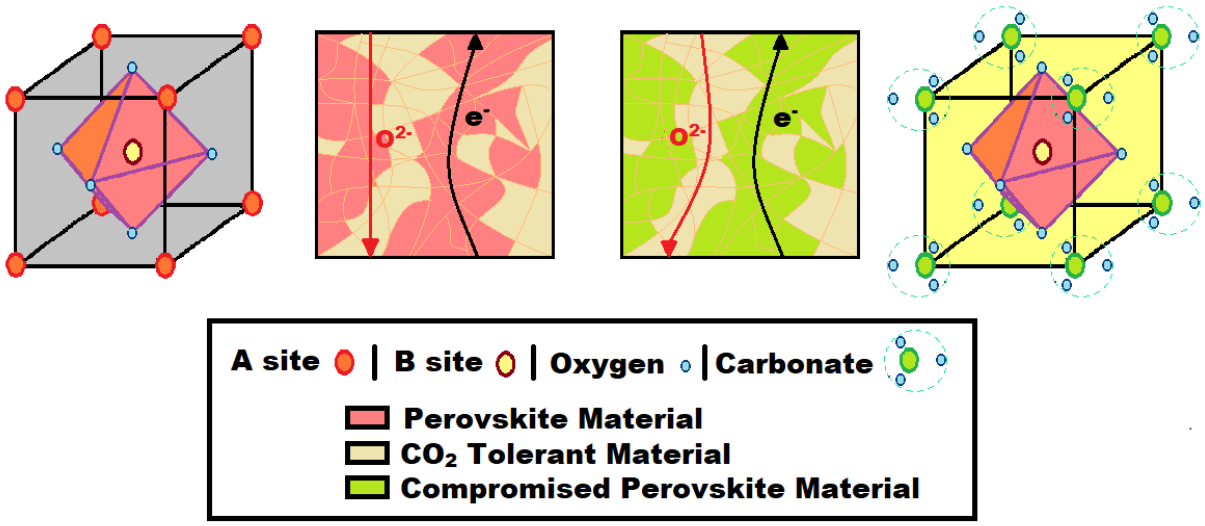

Figure 2.3 Ion and electron transportation through dual-phase membrane before (left side) and after (right side) carbonate formation on perovskite material

A potential problem with dual-phase OTMs is the addition of highly ionic conductive materials within the membrane which can limit oxygen permeation performance in the presence of inert/fuel gas streams. An exclusively mixed ionic-electronic conductive OTM can reduce, via surface reaction, surrounding oxygen anywhere on the surface. However, the addition of a purely ionic conductive material, limits the number of electron pathways leading to the surface, thus reducing the surface exchange reaction between the membrane and surrounding air. Therefore, research must determine a dual-phase composition ratio that limits the addition of a resilient ionic conductive material, to reduce the sacrifice of the oxygen permeation performance in inert and fuel environments while maintaining stability in acidic CO_2 atmospheres.

2.5 Application of OTMs

OTMs have received growing attention over the past few years because of their ability to deliver large volumes of oxygen at lower energy costs relative to conventional oxygen separation techniques. Air Products and Chemical, Inc. have already developed a sizeable scale-up process using a wafer-stack configuration for the partial oxidation of methane to syngas [115]. Praxair,

Inc. is another industry leader that has adopted a scale-up OTM design that incorporates tubular channels to produce syngas [116]. Alternative to Air Products and Chemical, Inc., Praxair, Inc. recirculates small amounts of syngas into the OTMs to further enhance the oxygen permeation flux. The OTM exhaust is then combined with methane and fed into an OTM tube packed catalyst for auto-thermal reforming for the production of syngas [116]. Although this technique sacrifices some of the produced syngas for recirculation, it benefits from the resulting higher oxygen permeation flux due to the presence of fuel.

Both scale-up processes encourage the potential for incorporating OTM technology into current power plants to mitigate carbon emissions, which some denote as advanced zero emission power plants (AZEPs). A simplified AZEP model was detailed in Fig. 1.3, in which depicts pressurized air flowing over the feed side of the OTM, while fuel (i.e., natural gas) and a portion of recycled CO_2 is fed into the sweeping side of the membrane to enhance the oxygen permeation flux [117]. The permeated oxygen reacts with the fuel, producing heat to sustain the OTM's permeability as well as to generate power [52,118–120]. Already several computational models have been developed to evaluate OTM performance and operation efficiency, with some results showings a 50% reduction in the energy penalty compared to other air separation technologies [121–124]. Presently, however, there is little experimental work that complements these models, signifying a greater need to explore research fundamentals for implementing OTMs for the application of oxy-fuel combustion.

2.6 Summary and Conclusions

In this chapter, OTM fundamentals and their relation to the oxygen permeation performance were discussed. The oxygen transport mechanisms and limitations are explained using developed models while pinpointing key components that influence oxygen permeability (i.e., structure, ionic

and electronic conductivity, and partial pressure of oxygen on either side of the OTM). Additionally, the potential degradation of OTMs from CO_2 atmospheres is also discussed, highlighting dual-phase compositions as a possible solution for maintaining the membrane's chemical and mechanical stability. Lastly, the application of OTMs for simultaneous oxygen separation and combustion is also presented.

From this summary of the current and previous research, it can be concluded that:

(1) The performance of the OTM is primarily governed by its rate-limiting step, determined by the characteristic thickness of the membrane. Due to the materials limited ionic mobility, OTM's oxygen permeation performance is limited by bulk diffusion (i.e., the ionic mobility through the membrane). Furthermore, the ionic conductivity is very difficult to quantify due to the mixed ionic and electronic conductivity of the perovskite-type material, suggesting the need for an innovative method to determine oxygen ionic mobility through the membrane.

(2) OTMs are made of perovskite-type materials due to their mixed ionic and conductive properties. Currently, most of the developed materials exhibit a low oxygen permeation flux (<1 ml.min^{-1}.cm^{-2}), resulting in limited work that identifies performance trends when investigating OTMs for the application of oxy-fuel combustion.

(3) The major disadvantage of perovskite materials is their low tolerance of CO_2 gases. The degradation of the perovskite-type oxide would jeopardize the legitimacy of OTM technology, particularly for the application of oxy-fuel combustion, which subjects the membrane to significant concentrations of CO_2 downstream. One potential solution is adapting dual-phase OTMs which combine the mixed ionic and electronic conductive properties of the perovskite-type material with a CO_2-tolerant ionically conductive

additive. However, the addition of the stable additive would jeopardize the oxygen permeation flux of the OTM in a rich fuel environment upstream. Thus, a further investigation that determines a balanced ratio between the perovskite-type and stable additive must occur.

(4) Currently, there is limited experimental research that bridges the gap between material science and combustion, despite both fields playing an essential role in the development of OTM technology. Although several simulations examine the overall oxygen permeation performance for the application of oxy-fuel combustion, no current experimental method can estimate the overall performance and size needed for complete combustion. If OTMs are to be established for the implementation of oxy-fuel combustion, an innovative approach must be adapted to create a standard that newly developed OTMs can aspire to achieve.

Chapter 3 Understanding the oxygen ion diffusivity of $SrSc_{0.1}Co_{0.9}O_{3-\delta}$ using experimental and computational methods

3.1 Introduction

Perovskite-type oxides ($ABO_{3-\delta}$) have been identified as candidates for oxygen transport membranes reactors because of their combined oxygen permeability at high temperatures ($\geq$800°C) and chemical stability in both oxidizing and reducing atmospheres. As shown in Table 2.1, current developed perovskite-type materials exhibit a low oxygen permeation flux (<1 $ml.min^{-1}.cm^{-2}$) signifying a lack of high performing membranes. The major contributing factor towards the oxygen permeability is the oxygen ion transport through the membrane. At high temperatures, vacancies sites are formed throughout the entire membrane, allowing oxygen ions to diffuse from the air feed side (high pO_2) to the permeation side (low pO_2) (Fig. 3.1). Therefore, to develop perovskite-type materials with a high oxygen permeation flux, there should be a stronger focus on oxygen ion diffusivity.

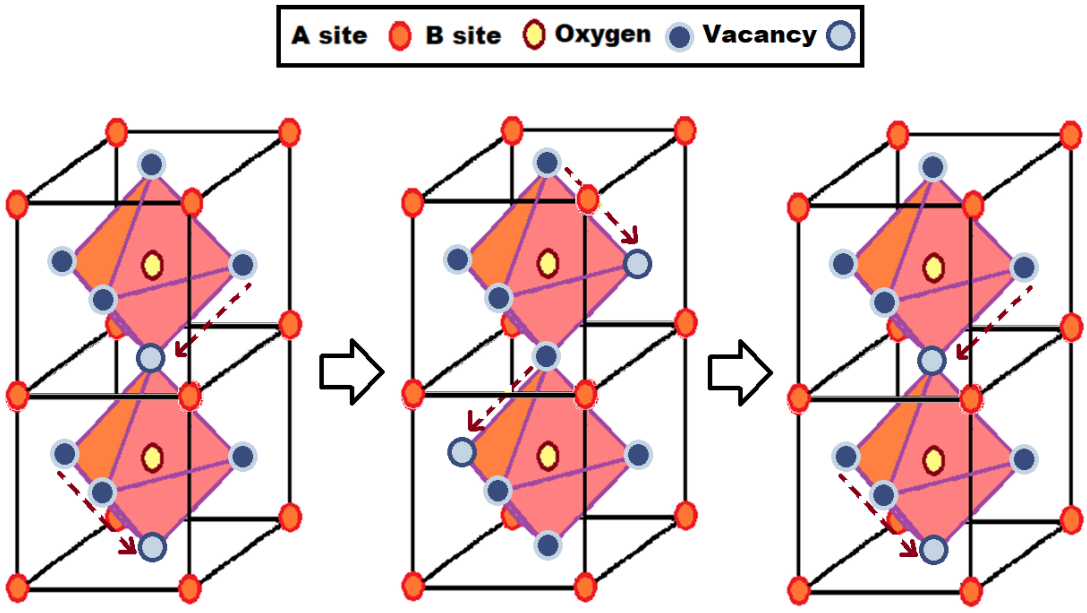

Figure 3.1 Schematic of oxygen ion transport through perovskite structures

However, determining the oxygen ion diffusivity of perovskite-type materials is challenging. Perovskite-type oxides are mixed ionic and electronic conductors, in which the electronic conductivity is orders of magnitude greater than ionic conductivity, making it difficult to determine the oxygen ion mobility. One solution to characterize the oxygen ion diffusivity is using molecular dynamics simulation (MDS), which numerically studies the physical movements of atoms and molecules to calculate the transient behavior of ions in crystal systems. Additionally, the use of computational methods could potentially reduce the time and cost required to investigate newly developed materials.

Past MDS studies have demonstrated the ability to approximate oxygen ion diffusivity of materials, but have never been experimentally validated [125–129]. In this chapter, the oxygen ion diffusivity is investigated for a perovskite-type material using experimental and MDS approaches. The chemical structure and morphology of the perovskite-type material are examined to construct the MDS accurately. The oxygen ion diffusivity results found from the experimental and MDS approaches are also compared to identify critical factors that contribute to the oxygen ion mobility through the membrane.

3.2 Experimental methods

3.2.1 Powder synthesis and membrane fabrication

Recently a series of novel oxide ($SrSc_yCo_{1-y}O_{3-\delta}$) were investigated in which it was discovered that a minor doping of Sc^{3+} into the B-site of $SrCoO_{3-\delta}$ effectively stabilized the cubic phase structure, with the optimum doping levels found to be 10 mol% [43–45,130]. In comparison to other materials, $SrSc_{0.1}Co_{0.9}O_{3-\delta}$ (SSC) demonstrated a superior electronic conductivity than $Ba_{0.5}Sr_{0.5}Co_{0.8}Fe_{0.2}O_{3-\delta}$ (BSCF), a common studied materials [131]. For this purpose, SSC was selected as the investigated perovskite-type material in this chapter.

SSC was synthesized by a complexing sol-gel process. $Sr(NO_3)_2$, $Co(NO_3) \cdot H_2O$, and ScO_3 were selected as the raw materials needed to produce the metal ions in the SSC material. A weighted amount of Sc_2O_3 was dissolved in an HNO_3 heated aqueous solution. $Sr(NO_3)_2$ solid and $Co(NO_3)_2$ aqueous solution were added to the solution at the required stoichiometry as well as the weighted amounts of ethylenediaminetetraacetic acid (EDTA) and citric acid. The resulting gel was heated and stirred overnight and subsequently pre-calcined at 250°C. The pre-calcined material was broken down using a mortar and pestle and after that calcined at 800°C for 5 hours. The detailed process is further shown in Fig. 3.2. The synthesized powders were then ground down using a ball mill and subsequently pressed into bars with approximate dimensions of 1.5x0.4x0.4 cm using a dry pressing technique. The produced green bars were sintered at 1200°C for 5 hours at a ramp rate of 1°C/min using a Nabertherm High-Temperature Furnace.

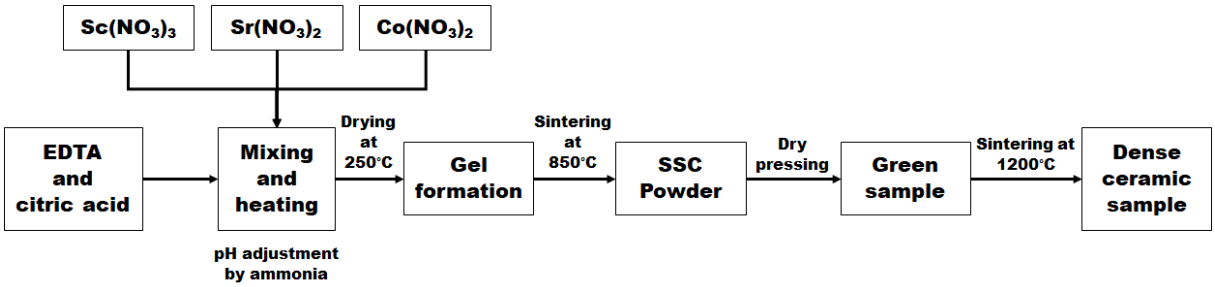

Figure 3.2 The process for SSC powder synthesis and membrane fabrication

3.2.2 X-ray diffraction and morphology

X-ray diffraction analysis (XRD) was performed at room temperature using a Bruker Axis D8 Advance diffractometer with Cu K_α radiation. Data sets were collected in a step-scan mode in the 2θ range of 15°-80° on an interval of 0.04° at a rate of 12 scans per second. The morphology features of the sintered bars were examined using a scanning electron microscope (SEM, JEOL 5600 SEM). Grain boundaries of the sintered bar were studied using electron backscatter diffraction (EBSD) associated with the SEM [132–134].

3.2.3 Experimental investigation of the oxygen chemical diffusion and average oxygen diffusion coefficients

As discussed in Chapter 2, the ionic conductivity (σ_{ion}) can be linked to the average oxygen diffusion coefficient using Nernst-Einstein relation (Eq. 2.5). Alternative to finding the average oxygen diffusion coefficient (D_O) directly, it can be determined using the oxygen chemical diffusion coefficient (D_{Chem}) and thermodynamic factor (Eq. 2.6). The oxygen chemical diffusion coefficient and thermodynamic factor were determined using an electrical conductivity relaxation technique (ECR) and thermogravimetric analysis (TGA), respectively.

ECR was used to characterize the oxygen chemical diffusion coefficient as well as the surface exchange coefficient (K_{ex}) of the SSC bar samples. ECR curves were generated by measuring the normalized conductivity of the sintered bar held at a constant membrane temperature, while abruptly reducing the partial pressure of oxygen in the surrounding atmosphere. The total conductivity of the SSC bar samples was measured by a four-probe D.C. method using a Keithley 2420 Sourcemeter (Fig. 3.3). Four silver wires were sealed around the bar's cross section (A) using silver paste spaced apart by distance L. After sealing the bar samples, they were heated in a tubular furnace while maintaining the partial pressure in the surrounding atmosphere. The resistance was measured by delivering a step current from 10μA to 2A, to two of the four wires, while simultaneously measuring the voltage across the other two sealed wires. The total resistance (K) of the sample was determined by the slope of the current/voltage curve. The total conductivity (σ) of the SSC bar was then calculated using Eq. 3.1:

$$\sigma = \frac{L}{AK} \qquad \text{(Eq. 3.1)}$$

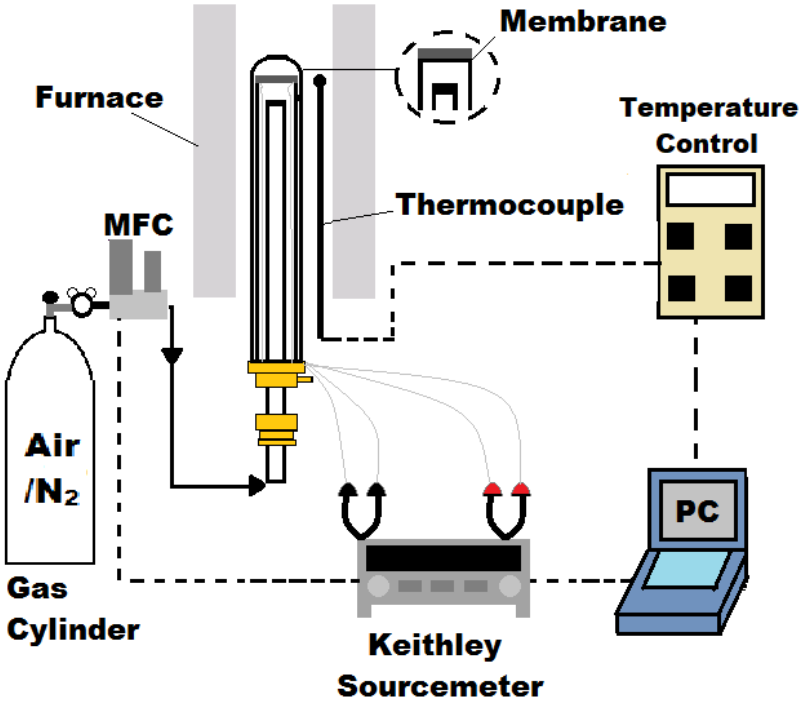

Figure 3.3 Experimental setup for ECR

ECR testing was conducted at membrane temperatures ranging from 600°C to 900°C at intervals of 25°C. Initially, air (0.21atm) was introduced to the surrounding atmosphere of the sample, prompting the initial conductivity measurement. The atmosphere was then abruptly changed to a lower oxygen concertation (0.01 atm) by flooding the surrounding environment with nitrogen, while periodically measuring the material's conductivity. This process was a reduction step in which oxygen is released from the structure, reducing the total conductivity of the material by Fick's second law and Eq. 2.1 [135]. D_{Chem} and K_{ex} were then obtained by fitting the normalized ECR curves into Eq. 3.2, where σ_0, σ_t, and σ_∞ are the initial, transient, and final conductivities, respectively [136,137].

$$\frac{\sigma_t-\sigma_0}{\sigma_\infty-\sigma_0} = 1-\sum_{p=1}^{\infty}\frac{2L_x^2}{\beta_x^2(\beta_x^2+L_x^2+L_x)}\exp\left(\frac{-\beta_x^2 D_{Chem}t}{l_x^2}\right)\times \sum_{q=1}^{\infty}\frac{2L_y^2}{\beta_y^2(\beta_y^2+L_y^2+L_y)}\exp\left(\frac{-\beta_y^2 D_{Chem}t}{l_y^2}\right)\times\sum_{r=1}^{\infty}\frac{2L_z^2}{\beta_z^2(\beta_z^2+L_z^2+L_z)}\exp\left(\frac{-\beta_z^2 D_{Chem}t}{l_z^2}\right) \quad \text{(Eq. 3.2)}$$

L_x, L_y, and L_z are defined in Eq 3.3, where l_x, l_y, and l_z are the respective lengths of the SSC bar.

$$L_x = l_x \frac{K_{ex}}{D_{Chem}}; L_y = l_y \frac{K_{ex}}{D_{Chem}}; L_z = l_z \frac{K_{ex}}{D_{Chem}} \quad \text{(Eq. 3.3)}$$

β are the positive roots determined by the equation

$$\beta_i \tan \beta_i = L_i \text{ with i=x, y, z} \quad \text{(Eq. 3.4)}$$

The normalized ECR plots were fitted using a developed MATLAB software package that applied an asymptotic statistical approach to reduce the uncertainty for estimating D_{Chem} and K_{ex} [138].

The thermodynamic factor was determined using powder samples of approximately 30 mg in a TGA. Samples were heated at a rate of 5°C/min to a set temperature corresponding to the membrane temperatures used for the ECR testing (600°C to 900°C on intervals of 25°C). Once the desired temperature was achieved, the powder samples were exposed to air until the weight stabilized (±5 μg). Afterwards, the partial pressure of oxygen was dropped down to 0.01 atm and held there until the sample reached stabilization again. The oxygen nonstoichiometric coefficient (δ) was determined using Eq. 3.5:

$$\frac{m_1}{MW_{SrSc_{0.1}Co_{0.9}O_{3-\delta}}} = \frac{m_2}{MW_{SS(air/nitrogen)}} \quad \text{(Eq. 3.5)}$$

where m_1 and $MW_{SrSc_{0.1}Co_{0.9}O_{3-\delta}}$ represent the mass and molecular weight at room temperature, respectively; m_2 and $MW_{SS(air/nitrogen)}$ are the steady-state mass and molecular weight, respectively, of the heated SSC material at a constant temperature in air or nitrogen atmospheres. The molecular weight of SSC at room temperature was previously reported in the literature, in which the nonstoichiometric coefficient of oxygen was determined to be 0.475 based on the valence of the cobalt ions obtained from the titration process [139]. After obtaining the thermodynamic factor, the average oxygen diffusion coefficient was determined by dividing the chemical diffusion coefficient by the thermodynamic factor Eq. 3.6.

$$\frac{D_{Chem}}{\left(\frac{\partial \ln(pO_2)}{2\partial \ln(C_O)}\right)} \approx D_O \qquad \text{(Eq. 3.6)}$$

3.2.4 MDS study to determine the average oxygen ion diffusivity

The MDS of SSC was provided by the Quantum Nanoscale Flow Systems Laboratory from the Institute of Fluid Science at Tohoku University. The simulation method used in this chapter is based on the Coulomb-Buckingham potential, in which the energy between ions (φ_{ij}) is calculated by partitioning it into long-range coulombic and short-range repulsive dispersive terms [140,141]. As shown in Eq. 3.7, q_i and q_j are the charges of the two ions i and j, respectively, separated by distances r_{ij}. A_{ij}, ρ_{ij}, C_{ij} are the potential parameters for each ion interaction shown in Table 3.1. The potential parameters were used to generate the SSC perovskite structure. Calculations were carried out using the MD simulation software LAMMPS [142,143].

$$\varphi_{ij}(r) = \frac{q_i q_j}{r_{ij}} + A_{ij} \exp\left(\frac{-r_{ij}}{\rho_{ij}}\right) - \frac{C_{ij}}{r_{ij}^6} \qquad \text{(Eq. 3.7)}$$

Table 3.1 Interatomic Potentials for $SrSc_{0.1}Co_{0.9}O_{3-\delta}$

Interaction	***A* (eV)**	***ρ* (Å)**	***C* (eV/Å^6)**	**Ref.**
$Sr^{+2} \cdots O^{-2}$	959.10	0.3721	0.000	[144]
$Co^{+3} \cdots O^{-2}$	1329.82	0.3087	0.000	[145]
$Sc^{+3} \cdots O^{-2}$	1575.85	0.3211	0.000	[146]
$O^{-2} \cdots O^{-2}$	22764.3	0.1490	43.00	[144]

The SSC material was simulated at temperatures corresponding to the same membrane temperature conditions used for ECR (600°C to 900°C at intervals of 25°C). In all cases, Co and Sc ions were assumed to be trivalent, while Sr was divalent. Simulation boxes for all investigated

conditions were constructed from 9x9x9 $ABO_{3-\delta}$ unit cells, in which the Sc dopant and vacancy sites were randomly distributed throughout the entire structure to maintain a neutral charge. Investigated systems were equilibrated under constant temperature and constant pressure (NPT) held at 1 bar. A time step and cutoff distance of 1.0 fs and 10 Å were used to ensure accurate integration of the equations of motion and conservation of energy.

To investigate the oxygen ion diffusivity properties of SSC, the mean square displacement (MSD) of the oxygen ions within the system was calculated as a function of time. The MSD of oxygen is defined as:

$$MSD(t) = \frac{1}{NN_t}\sum_{n=1}^{N}\sum_{t_0}^{N_t}[r(t+t_0) - r(t_0)]^2 \qquad \text{(Eq. 3.8)}$$

where N is the total number of ions of the species, r(t) is the position of ion i at time t and N_t is the total number of initial time steps the average is taken over [140]. The average oxygen diffusion coefficient (D_o) was calculated from the slope of its MSD vs. time plot using the Einstein relation:

$$\frac{d(MSD)}{dt} = B + 6Dt \qquad \text{(Eq. 3.9)}$$

where B is twice the square of the mean vibrational amplitude of oxygen [140].

3.3 Results and discussion

3.3.1 Phase structure and morphology

Figure 3.4 shows the X-ray diffraction patterns of the as-synthesized SSC oxide calcined at 800°C for 5 hours in air. The XRD pattern suggests that the 10 mol % of scandium doping into the B-site of the $SrCoO_{3-\delta}$ structure can stabilize the cubic perovskite structure. Similar results concerning the lattice structure of SSC have been reported in previous works [44]. From the XRD data and Bragg's Law, the lattice parameter of the cubic perovskite structure was found to be 3.91 Å and was used to construct the simulated model.

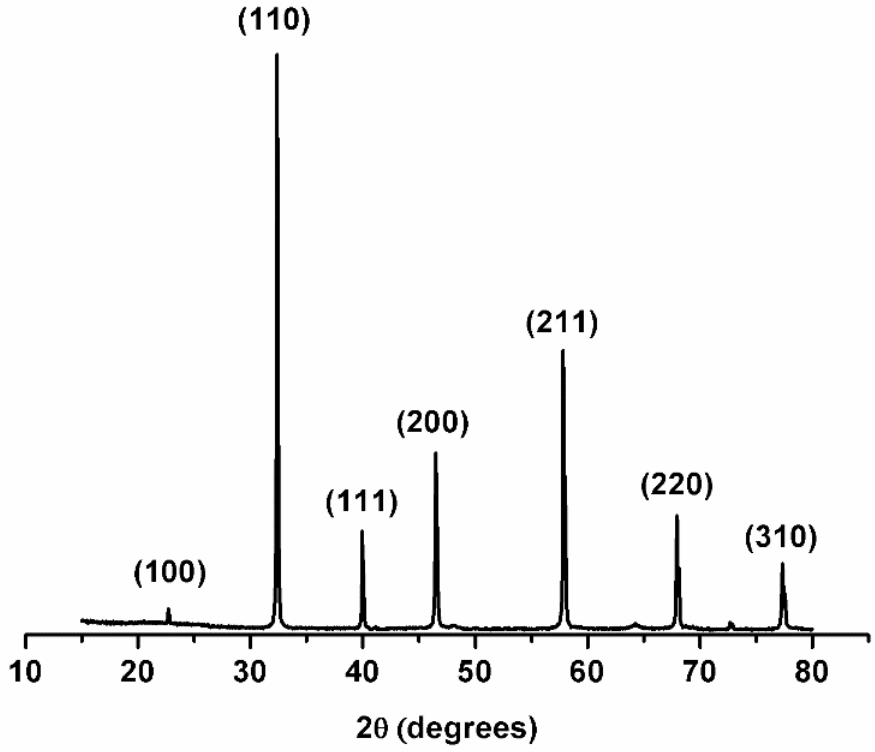

Figure 3.4 XRD pattern of SSC powder indicating a cubic perovskite structure

To be applied as an air separation unit, OTMs must possess a dense structure needed to prevent all nitrogen on the air feed side from reaching the permeation side. Figure 3.5 shows the SEM images of the surface and cross-section of a sintered SSC ceramic bar. In both images, the surface and cross section exhibit no pores or cracks throughout its entire structure, indicating that 1200°C is an appropriate sintering temperature for producing a dense ceramic membrane.

The membrane structure is also shown to exhibit grain boundaries, formed at the interface between grains of different sizes. In grain boundaries, the chemical structure of the materials composition is maintained but presents a shift in the lattice structure's orientation relative to the adjacent grain [147]. This inconsistency in the atomic structure at the interface between two grains could influence oxygen ion mobility through the OTM. The EBSD analysis provides a deeper insight into the misorientation angle throughout the entire structure, and the results are shown in

Fig. 3.6. It can be seen in Fig. 3.6 that most angles found in the SSC membrane are at high angle orientations, which could modify the diffusivity of the oxygen ions through the membrane.

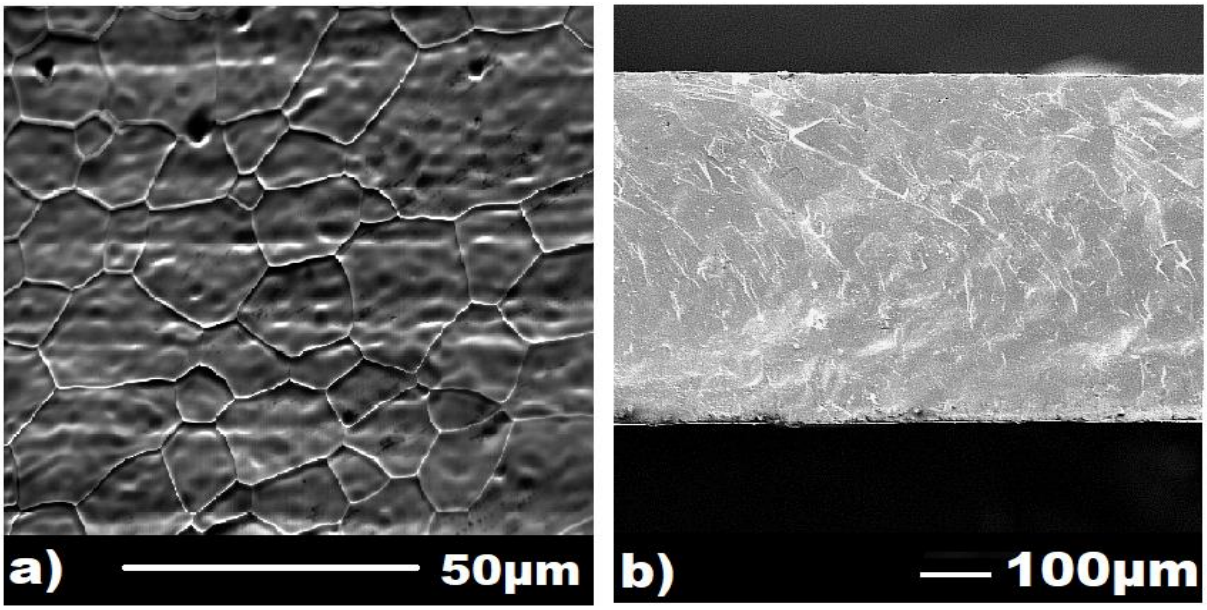

Figure 3.5 SEM images of the surface (a) and cross section (b) of SSC after sintering at 1200°C for 5 hours.

3.3.2 Oxygen chemical diffusion and surface exchange coefficients

The oxygen chemical diffusion and surface exchange coefficients were determined using ECR. Fig. 3.7 shows the ECR curves at various membrane temperatures generated by a sudden change in the oxygen partial pressure from 0.21 to 0.01 atm. As expected, the normalized total conductivity can achieve unity faster as the membrane temperature increases, signifying an enhancement of the oxygen diffusivity and surface exchange properties of the SSC material. The oxygen chemical diffusion and surface exchange coefficients were then determined from the fitted curves. The findings are displayed in Fig. 3.8.

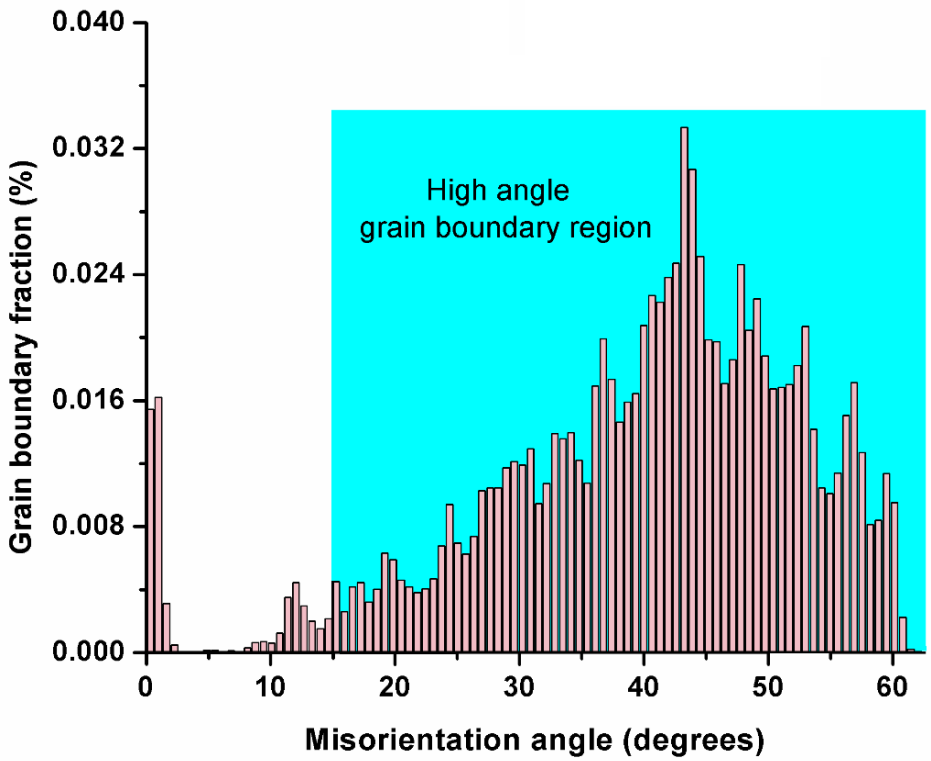

Figure 3.6 Misorientation angle of grain boundaries in SSC membrane sintered at 1200°C

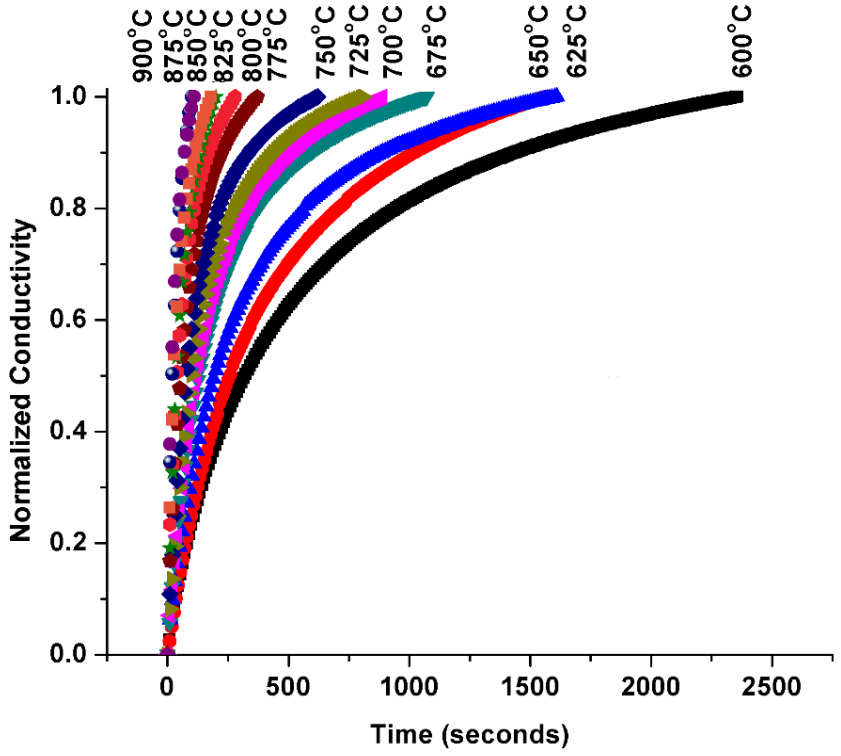

Figure 3.7 ECR curves for SSC ranging from 600°C to 900°C after abruptly reducing the oxygen partial pressure in the surrounding atmosphere from 0.21 atm to 0.01 atm

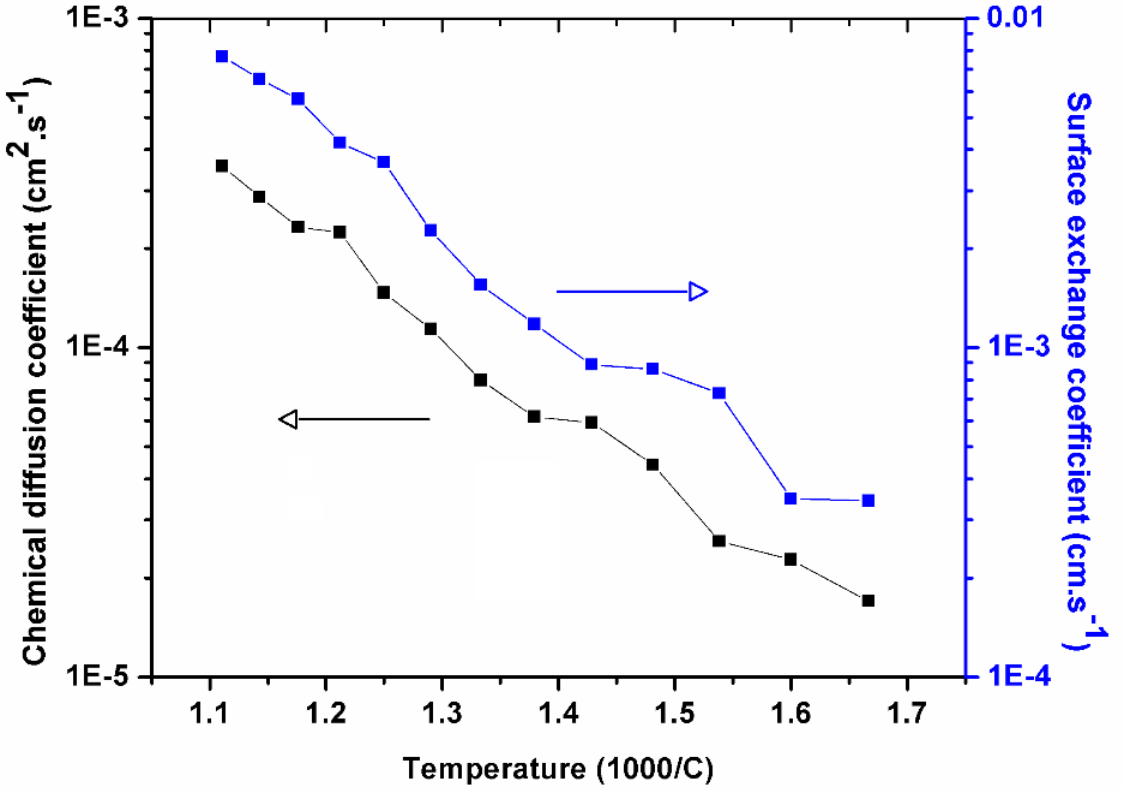

Figure 3.8 Oxygen chemical diffusion and surface exchange coefficients of SSC ranging from 600°C to 900°C obtained from ECR during the reduction process

Figure 3.8 shows the increase of the SSC material's oxygen chemical diffusion and surface exchange coefficients with an increase in membrane temperature. Compared to other perovskite-type materials, SSC is found to exhibit superior oxygen diffusivity and surface exchange properties. For example, at 750°C, the oxygen chemical diffusion and surface exchange coefficients of $La_{0.}Sr_{0.4}Co_{0.2}Fe_{0.8}O_{3-\delta}$ (LSCF) was 6.4E-6 $cm^2.s^{-1}$ and 1.3E-5 $cm.s^{-1}$, respectively, compared to SSC's coefficients found to be 7.96E-5 $cm^2.s^{-1}$ and 1.55E-3 $cm.s^{-1}$, respectively [148]. Another example is with $B_{0.5}Sr_{0.5}Co_{0.8}Fe_{0.2}O_{3-\delta}$ (BSCF) which at 600°C had an oxygen chemical diffusion and surface exchange coefficient of 5.01E-6 $cm^2.s^{-1}$ and 3.16E-4 $cm.s^{-1}$ which is lower compared to the respective SSC coefficients of 1.75E-5 $cm^{2}.s^{-1}$ and 3.43E-4 $cm.s^{-1}$ at the same membrane temperature [149].

The thermodynamic factor was determined using TGA, and the results are shown in Table 3.2. As previously discussed the thermodynamic factor accounts for the concentration of oxygen present in the perovskite-type material as the membrane temperature or the surrounding partial pressure of oxygen varies. The thermodynamic factor was determined using the data presented in the middle columns of Table 3.2 and using Eq. 2.6. As seen from Table 3.2, the oxygen nonstoichiometric coefficient (δ) decreases with an increase in membrane temperature, indicating the formation of more oxygen vacancies in the perovskite-type material. The oxygen nonstoichiometric coefficient is also observed to be higher when subjected to atmospheres with higher concentrations of oxygen. The higher nonstoichiometric coefficient indicates a higher fraction of occupied vacancy sites in the presence of air compared to depleted oxygen atmospheres. The thermodynamic factor, in the last column of Table 3.2, is observed to be consistent at lower membrane temperatures, but then decline as the membrane temperature increases beyond 750°C. The minor variation in the thermodynamic factor at low membrane temperatures suggests that the difference between the number of vacancy sites in air and nitrogen are similar at membrane temperatures below 750°C. As the membrane temperature rises beyond 750°C, the difference between the number of occupied oxygen vacancies in air and nitrogen atmospheres becomes more substantial, thus reducing the thermodynamic factor as the membrane temperature increases. Past studies have reported similar results [57].

Table 3.2 Oxygen stoichiometry coefficient (3-δ) and thermodynamic factor for SSC as a function of temperature and oxygen partial pressure

Temperature (°C)	**P_{O_2}**	**3-δ**	**Thermodynamic Factor**
600	0.21	2.384	63.78
	0.01	2.322	
625	0.21	2.364	71.06
	0.01	2.314	
650	0.21	2.355	64.34

	0.01	2.300	
675	0.21	2.351	65.13
	0.01	2.296	
700	0.21	2.346	65.97
	0.01	2.293	
725	0.21	2.342	65.92
	0.01	2.289	
750	0.21	2.338	64.84
	0.01	2.284	
775	0.21	2.333	63.22
	0.01	2.278	
800	0.21	2.330	60.56
	0.01	2.272	
825	0.21	2.326	57.67
	0.01	2.266	
850	0.21	2.323	54.27
	0.01	2.259	
875	0.21	2.320	50.44
	0.01	2.251	
900	0.21	2.317	46.72
	0.01	2.243	

3.3.3 Average oxygen diffusion coefficient

Once obtained, the thermodynamic factor and oxygen chemical diffusion coefficient were combined to determine the average oxygen diffusion coefficient using Eq. 3.5. The determined average oxygen diffusion coefficient, including the MDS's calculated average oxygen diffusion coefficient, are shown in the Arrhenius plot in Fig. 3.9. As described in Chapter 2, the average oxygen diffusion coefficient is considered constant over the thickness of the membrane while the chemical diffusion coefficient accounts for the variation of occupied vacancies within the perovskite structure. Thus, the oxygen chemical diffusion coefficient is higher than the experimental and MDS results.

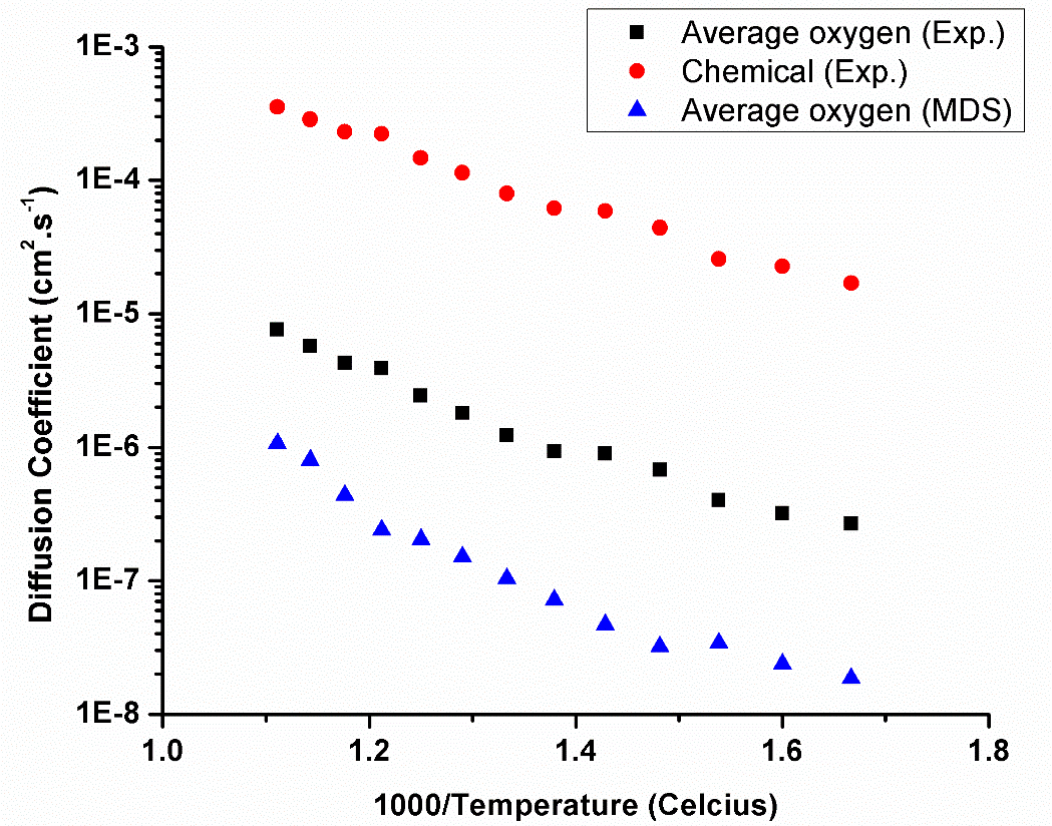

Figure 3.9 Average oxygen diffusion coefficient and oxygen chemical diffusion coefficient SSC ranging from 600°C to 900°C determined using MDS and experimental methods

The characteristic thickness of SSC at varying temperature was determined using Eq. 2.7 by combining the experimental average oxygen diffusion and surface exchange coefficients. The characteristic thickness of SSC was found to be consistent with an average of thickness 8.2E-4 cm at all investigated temperatures. The determined characteristic thickness indicates that the rate-determining step of SSC membranes is oxygen ion bulk diffusivity as opposed to the surface exchange reactions. This limitation signifies that bulk diffusion primarily limits SSC material due to the required membrane thickness needed to preserve mechanical integrity (>3.2E-2 cm).

Figure 3.9 also shows an order of magnitude difference between the average oxygen diffusion coefficient determined experimentally and through MDS. Both the experimental and simulation results demonstrate an increase in the average oxygen diffusion coefficient with an increase in temperature, but the experimental results are observed to be an order of magnitude higher. One

potential explanation for the difference in the calculated oxygen diffusivity is the morphology of the SSC membrane. The MDS constructed model examined the bulk diffusivity of oxygen through a perovskite system, not accounting for the presence of grain boundaries. As previously shown in Fig 3.6, fabricated SSC membranes exhibit multiple grain boundaries, in which the majority are considered high angle grain boundaries (>15°). In past studies, high angle grain boundaries have been shown to enhance the average oxygen diffusion coefficient due to lower coordination numbers at the grain interface [150–152]. Therefore, it can be theorized that the order of magnitude difference between the experimental and MDS average oxygen diffusion coefficients is attributed from the presence of high angle grain boundaries in the experimentally investigated SSC membrane, whereas the constructed fails to account for the grain boundary morphology.

3.4 Conclusion

In this chapter, SSC's structure, morphology, oxygen diffusion and surface exchange properties are investigated. SSCs structure is shown to exhibit a stabilized cubic phase structure with 10 mol% Sc^{3+} with a lattice parameter of 3.91 Å. After sintering at 1200°C, the surface and cross-section of the fabricated SSC membrane are found to have a dense structure with no observed pores or cracks. The sintered SSC membrane is also observed to consist of several grain boundaries, in which the majority were found to be high angle grain boundaries (>15°).

The oxygen chemical diffusion and surface exchange coefficients of SSC are discovered to be superior to highly regarded materials such as LSCF and BSCF under a wide range of temperatures. The determined thermodynamic factor and oxygen chemical diffusion coefficient are combined to calculate the average oxygen diffusion coefficient. The characteristic thickness of SSC at varying temperature is determined using the surface exchange and average oxygen diffusion coefficient and demonstrates SSC's rate-limiting step to be bulk diffusivity since the average characteristic

thickness was found to be 8.2E-4 cm, which is smaller than the required thickness needed to maintain the mechanical integrity of the membrane. The average oxygen diffusion coefficient determined experimentally is shown to be an order of magnitude higher than the values found in MDS. The difference between the average oxygen diffusion coefficients is potentially attributed to the previously mentioned high angle grain boundaries which have been previously reported to improve the oxygen diffusivity through the membrane.

Chapter 4 Investigation of oxygen transport membrane reactors for oxy-fuel combustion and carbon capture purposes

4.1 Introduction

Currently, fossil fuels are the primary source of energy that satisfies the increasing energy demand of almost every major country throughout the world [5]. However, it is projected that by combusting fossil fuels, an estimated 30 Gt of carbon dioxide (CO_2) is produced per year, making fossil fuels the primary source of CO_2 emissions [2,3]. In order to mitigate the amount of carbon entering our atmosphere, there is increasing pressure on industry to reduce and contain emissions from combustion processes, while still meeting current and future energy needs. Therefore, different techniques and practices are being developed to capture and sequester carbon from energy production processes [115,116,153].

Over the past few years, there has been a significant focus on oxygen transport membrane reactors (OTMs) and their potential to transform the way oxygen is supplied and used in combustion processes. When the membrane is placed under elevated temperatures ($\geq$800°C), fuel can be introduced to one side of the membrane while exposed to air on the other side. This forces the positively charged oxygen vacancy to become disordered, creating a chemical potential gradient across the membrane and allowing oxygen to permeate through the material and react with the fuel on the other side. The motion of oxygen vacancies, which gives rise to the nature of oxygen permeability of perovskite membranes, is charge compensated by the transport of electron-holes in the reverse direction [58]. Due to the lack of nitrogen, the combustion process is simplified to elementary reactions, eliminating nitrogen oxide and producing an exhaust primarily composed of carbon dioxide and water vapor. The CO_2 from the exhaust can then be captured and sequestered for further use.

As previously shown in Table 2.1, several studies have demonstrated dense perovskite ceramic membranes' oxygen permeability performance primarily using a helium sweeping gas. However, there have been limited studies done concerning the integration of OTM technology with methane combustion for carbon capture purposes. In this chapter, the performance of OTMs is investigated through modifying the reactor's composition, membrane temperature, sweeping gas flow rate, and shape configuration. Oxy-fuel combustion performance is evaluated by determining the OTM reactor's oxygen permeability and CO_2 selectivity from the flue gas.

4.2 Experimental methods

4.2.1 Material selection

To document the OTM's operation and performance, selecting a material that exhibits high oxygen permeation performance (>1 $ml.min^{-1}.cm^{-2}$) is crucial. Since Teraoka et al. first reported the remarkable high oxygen permeation flux through the ceramic disks based on the $La_{0.6}Sr_{0.4}Co_{0.2}Fe_{0.8}O_{3-\delta}$ (LSCF) perovskite oxides in the 1980s, cobalt-contained perovskite membranes have been widely investigated [29]. The LSCF membrane is currently cited as a typical example of the mixed conductive ceramics with moderate oxygen permeability and chemical/mechanical stability, consequently making it the most common material studied [154–162]. Alternatively, Zeng et al. have developed and reported a new perovskite system $SrSc_{0.1}Co_{0.9}O_{3-\delta}$ (SSC) which exhibits remarkably high oxygen fluxes and chemical stability [43–45]. The comparison between these two materials can provide a gage as to the development of OTM technologies, mainly focusing on the feasibility of using commercially available materials to demonstrate a high oxygen permeation flux SSC oxide was synthesized by a combined EDTA-citrate complexing sol-gel process as described in detail in Chapter 3. LSCF powder was purchased from Fuel Cell Materials, USA [163].

4.2.2 Oxygen permeation testing

Selected powders were pressed into disk-shaped green membranes with a diameter of 15 mm, which were subsequently sintered at 1200°C for SSC and 1250°C for LSCF to achieve a dense membrane structure. The sintered membranes had a diameter of 12-13 mm and a thickness of 0.44 mm or 1.1 mm. The densely sintered disk membranes were then applied as an OTM to study the reaction of methane combustion using the planar experimental setup shown in Fig. 4.1. A planar reactor was fixed onto a dense quartz tube using silver paste as a sealant, leaving an effective surface area of 0.65 cm^2. The fixed membrane was then placed in the center of a vacuum split furnace. A methane sweeping gas was fed underneath the planar OTM at standard temperature and pressure (STP), allowing for oxygen to permeate through the reactor, while the opposite side of the membrane was exposed to ambient air. Permeated oxygen would then react with methane, and the existing products would be fed into a gas chromatograph (GC) to quantify the exhaust composition. The gas flow rates were monitored with a digital flow meter. The integrity of the membrane seals was monitored by the nitrogen concentration in the product stream.

To characterize the performance of the OTMs, two significant parameters were examined: oxygen permeation flux and CO_2 selectivity. The oxygen permeation flux was calculated using carbon balance. As stated before, the reactor exhaust was analyzed using a GC which identified the component mole fractions of each product. When using a methane sweeping gas, the compositions in the product stream of converted fuel consisted of carbon dioxide (CO_2), carbon monoxide (CO), and ethane (C_2H_6). The combustion between the incoming fuel and permeated oxygen is described below, in molar flow rates ($\dot{n}$) of each species $\dot{n}_i$:

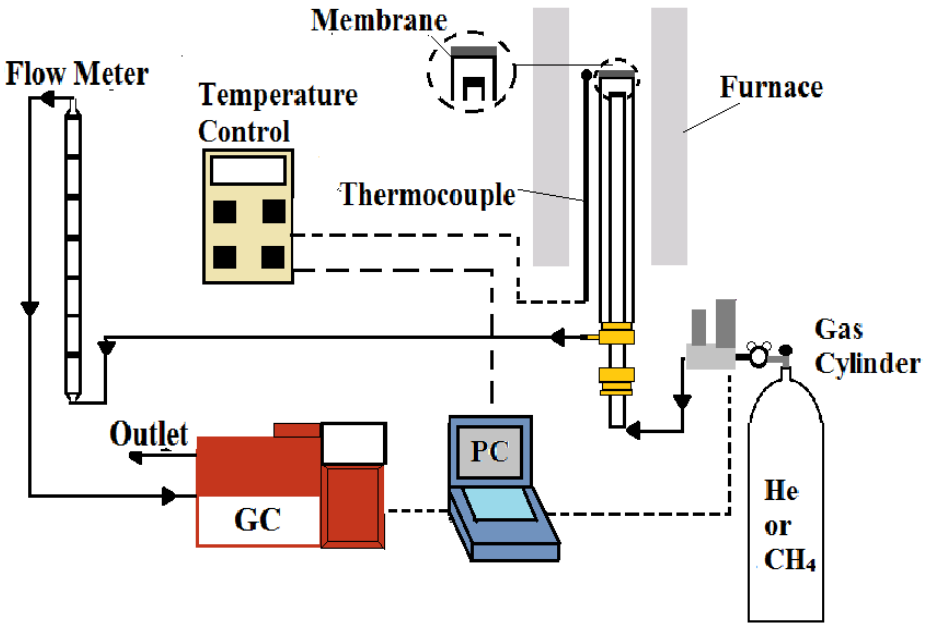

Figure 4.1 Experimental setup for oxygen permeation test for planar membrane OTMs

$$\dot{n}'_{CH_4}CH_4 + \dot{n}'_{O_{2,perm}}O_2 \rightarrow \dot{n}''_{CO_2}CO_2 + \dot{n}''_{CO}CO + \dot{n}''_{C_2H_6}C_2H_6 + \dot{n}''_{CH_4}CH_4 + \dot{n}''_{O_2}O_2 + \dot{n}''_{H_2O}H_2O \quad \text{(Eq. 4.1)}$$

The elemental conservation of C, O, and H results in:

$$\textbf{C: } \dot{n}'_{CH_4} = \dot{n}''_{CO_2} + \dot{n}''_{CO} + 2\dot{n}''_{C_2H_6} + \dot{n}''_{CH_4} \quad \text{(Eq. 4.2)}$$

$$\textbf{H: } 4\dot{n}'_{CH_4} = 6\dot{n}''_{C_2H_6} + 4\dot{n}''_{CH_4} + 2\dot{n}''_{H_2O} \quad \text{(Eq. 4.3)}$$

$$\textbf{O: } 2\dot{n}'_{O_{2,perm}} = 2\dot{n}''_{CO_2} + \dot{n}''_{CO} + 2\dot{n}''_{O_2} + \dot{n}''_{H_2O} \quad \text{Eq. 4.4)}$$

$$\dot{n}_{total} = \dot{n}''_{CO_2} + \dot{n}''_{CO} + \dot{n}''_{C_2H_6} + \dot{n}''_{CH_4} + \dot{n}''_{O_2} + \dot{n}''_{H_2O} \quad \text{(Eq. 4.5)}$$

$$X''_i = \dot{n}''_i / \dot{n}_{total} = \dot{F}''_i / \dot{F}_{total} \quad \text{(Eq. 4.6)}$$

where single and double primes refer to reactant and product values, $\dot{n}'_{O_{2,perm}}$ is the oxygen permeation flux, $\dot{n}_{total}$ and $\dot{F}_{total}$ are the total molar and volumetric flow rate, X_i is the mole and volumetric fraction of the i^{th} species, and i refers to the species carbon dioxide (CO_2), carbon monoxide (CO), ethane (C_2H_6), methane (CH_4), oxygen (O_2), detected from the GC. From a

combination of Eq. 4.4 and 4.6, and dividing by the effective surface area (S), the oxygen permeation flux (J_{O_2}; mol.min^{-1}.cm^{-2} or ml.min^{-1}.cm^{-2}) can be defined as:

$$J_{O_2} = (\dot{n}_{total}(2X''_{CO_2} + 1.5X''_{CO} + X''_{O_2} + 0.5X''_{C_2H_6}))/(2S) \quad \text{(Eq. 4.7)}$$

or since the molar fraction is equivalent to the volumetric fraction (Eq. (4.6)) of each species, the oxygen permeation flux can be re-written as:

$$J_{O_2} = (\dot{F}_{total}(2X''_{CO_2} + 1.5X''_{CO} + X''_{O_2} + 0.5X''_{C_2H_6}))/(2S) \quad \text{(Eq. 4.8)}$$

A derivation of Eq.4.7 can be found in Appendix A. The performance of the OTM relative to the permeated oxygen delivered to the fuel can be characterized regarding CO_2 selectivity as defined below:

$$CO_2(selectivity) = \dot{F}_{CO_2}/(\dot{F}_{CO} + \dot{F}_{CO_2} + 2\dot{F}_{C_2H_6}) \quad \text{(Eq. 4.9)}$$

Additionally, to further examine reactor geometry's influence on OTM performance, LSCF ceramic hollow fiber membranes were extruded from the plastic mass through an in-house designed die with an outer diameter (O.D.) of 3.6 mm and an inner diameter (I.D.) of 2 mm placed on a RAM extruder. After sintering the sintered tube, the O.D./I.D. of the hollow fiber membrane shrank from 3.6 mm/2 mm to 2.15 mm/1.05 mm. The sintered were cut to 0.90 cm, resulting in an effective surface area of 0.65 cm^2, not including the additional area needed to seal the membrane. The sintered dense hollow fiber membrane was fixed between two quartz tubes using silver paste to study the performance of methane combustion. The fixed membrane was placed in the center of a horizontal vacuum split furnace. Similar to the planar test, the experimental conditions were maintained for consistency, where again a methane sweeping gas was introduced into the reactor while the other side was exposed to the surrounding atmosphere. During these experiments, the instant temperature in the furnace was measured using a K-type thermocouple which was placed at the center of the membrane.

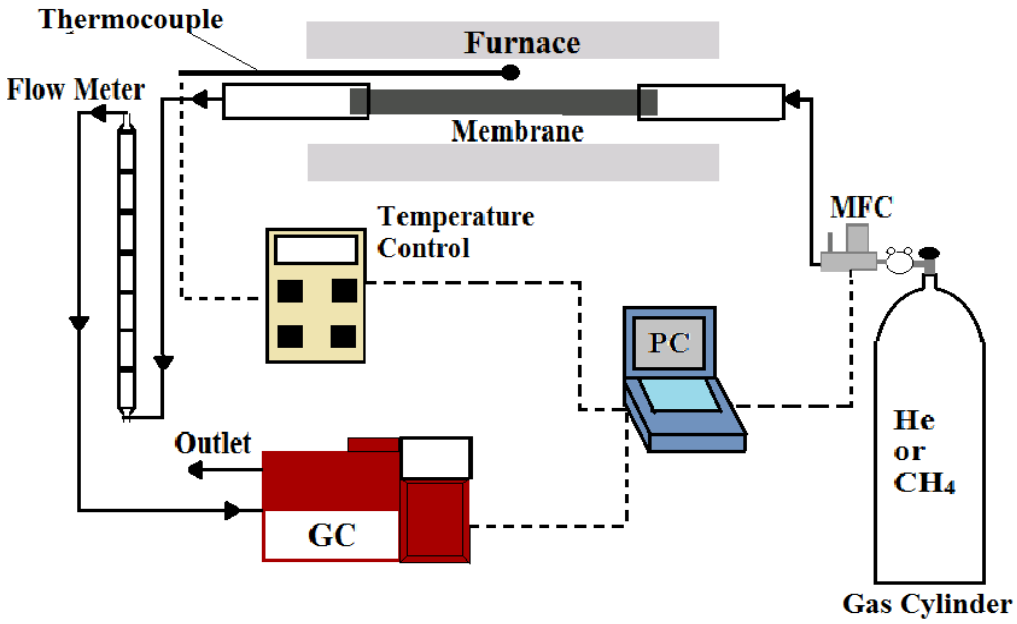

Figure 4.2 Experimental setup for oxygen permeation test for tubular OTMs

4.3 Results and discussion

4.3.1 Planar OTM investigation

The oxygen permeation flux of SSC and LSCF OTMs was investigated using pure methane at varying sweeping gas flow rates, from 2 to 20 $mL \cdot min^{-1}$ and different membrane temperatures ranging from 800°C to 900°C, on increments of 50°C. The results are shown in Fig. 4.3, displaying the influence of temperature and methane flow rate on the oxygen permeation performance of OTMs with different compositions. More importantly, Fig. 4.3 shows a significant comparison between the performance of LSCF and SSC reactor compositions.

First, due to the increased methane flow rate, there is a higher content of fuel introduced to the sweeping side of the planar OTM. The higher volume of fuel on the permeation side improves the chemical gradient across the OTM and resulting in the oxygen permeation flux increasing. During the permeation test, no oxygen was found in the product stream, signifying that all oxygen was utilized and the partial pressure of oxygen on the sweeping side was maintained at approximately

zero. Additionally, during the oxygen permeation test, no nitrogen was detected in the GC, indicating a hermetically sealed dense ceramic membrane.

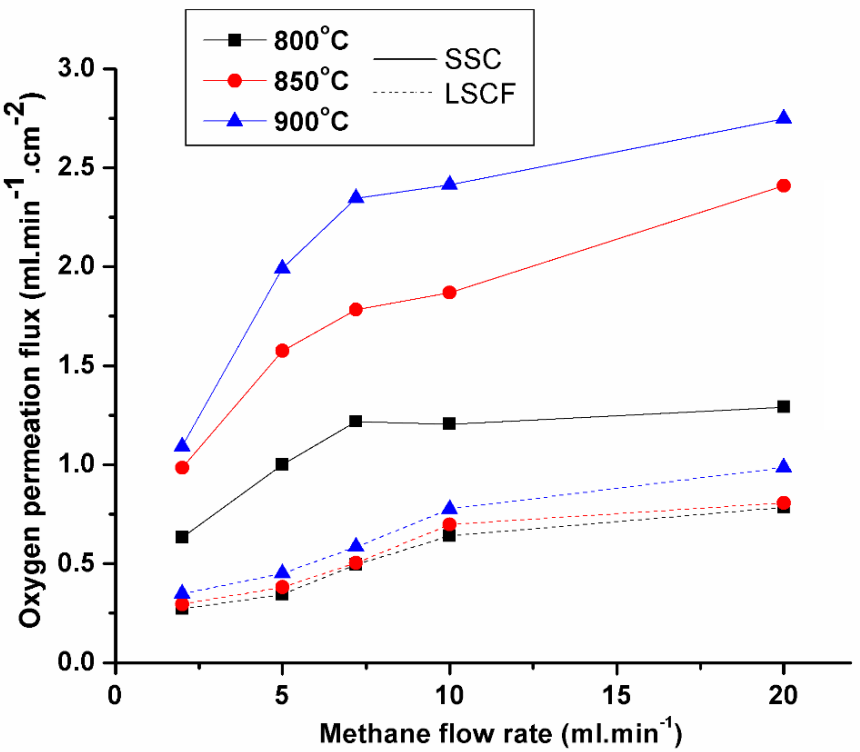

Figure 4.3 Oxygen permeation flux of LSCF and SSC planar OTMs with membrane thicknesses of 0.44 mm subjected to methane flow rates ranging from 2 to 20 ml.min^{-1} while held at membrane temperatures ranging from 800 to 900°C

Second, the increased temperature enhanced the oxygen diffusion and surface exchange coefficients of the membrane, thus improving the oxygen permeation rate. These differences can be seen more clearly for the SSC reactor composition, since the SSC reactor showed a significantly higher oxygen permeation flux compared to the LSCF reactor, over a wide range of methane flow rates and membrane temperatures. It is also interesting to note that SSC varies greatly with changes in membrane temperature at the same flow rate, while LSCF shows little variation as the operating temperature increases. The SSC OTM reached a maximum oxygen permeation flux of 2.75 mL·min^{-1}·cm^{-2} at a membrane temperature of 900°C and methane flow rate of 20 ml.min^{-1} and a minimum oxygen permeation flux of 0.63 mL·min^{-1}·cm^{-2} at a membrane temperature of 800°C

and methane flow rate of 2 ml.min^{-1}. The LSCF reactor reached a maximum oxygen permeation flux of 0.99 mL·min^{-1}·cm^{-2} at a membrane temperature of 900°C and methane flow rate of 20 ml.min^{-1} and a minimum oxygen permeation flux of 0.27 mL·min^{-1}·cm^{-2} at a membrane temperature of 800°C and methane flow rate of 2 ml.min^{-1}.

The significant difference between the achieved oxygen permeation flux results of the LSCF and SSC reactors is attributed to the composition of SSC, which exhibits higher oxygen diffusivity and surface exchange coefficients compared to LSCF, as discussed in Chapter 3. The superior properties allow for a higher oxygen permeation flux in the SSC OTM. The significant difference between the SSC and LSCF reactor performances raises concern over the current state of OTM technology used for carbon capture purposes. Theoretically, if LSCF membranes were to be used in a large-scale power generation facility, the total number of membranes required to produce a substantial amount of heat would be significantly higher compared to the recently developed SSC. Therefore, Fig. 4.3 not only depicts the trends associated with enhancing oxygen permeation fluxes but also provides a commentary on the importance that material investigation has in the development of OTM technology.

Due to the poor performance of the LSCF membrane, the study shifted focus onto enhancing the reactor design using SSC material. To further improve the performance of the reactor, a porous catalyst layer, with a thickness of 10 μm and an average pore size 4 μm, was applied onto the oxygen feed side of the membrane to increase the amount of exposed surface area and encourage a higher oxygen permeation flux. The same conditions used to obtain the oxygen permeation flux results shown in Fig. 4.3 were applied to the SSC OTM with the additional catalyst layer to see if the oxygen permeation flux could be improved. The oxygen permeation flux of the SSC OTM with the additional catalyst layer is shown in Fig. 4.4.

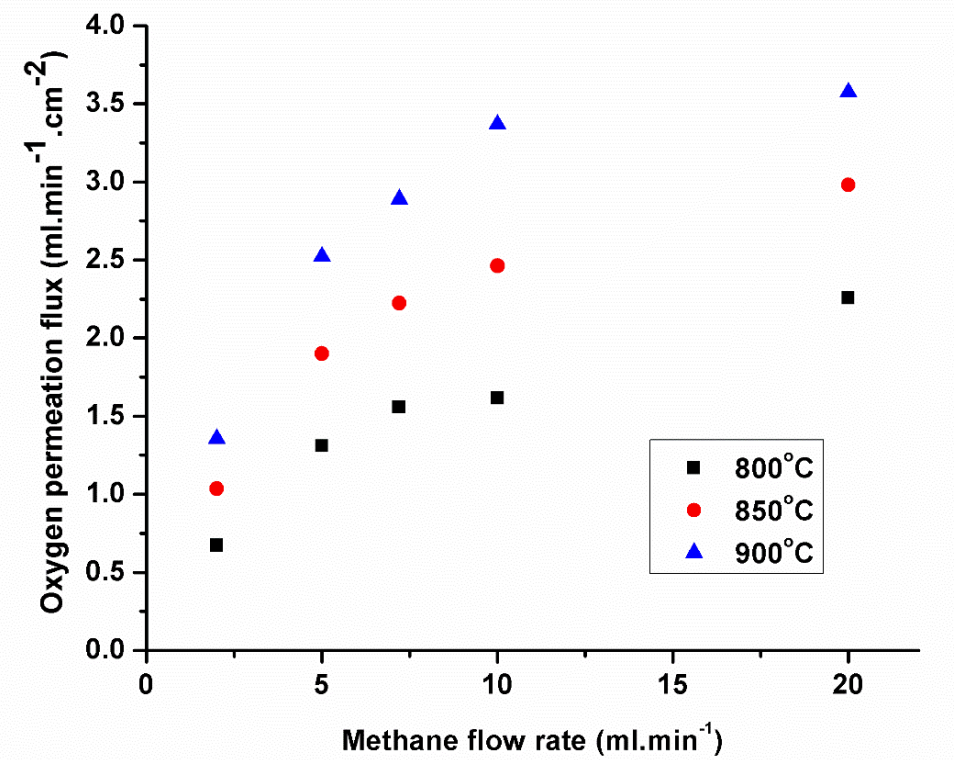

Figure 4.4 Oxygen permeation flux of SSC planar OTM with an additional porous catalyst layer subjected to methane flow rates ranging from 2 to 20 ml.min^{-1} while held at membrane temperatures ranging from 800 to 900°C

Similar to the results in Fig. 4.3, Fig. 4.4 shows the oxygen permeation flux increasing with an increase in membrane temperature and methane flow rate. At a constant temperature of 900°C, the membrane with an applied porous catalyst layer was able to achieve an oxygen permeation flux of 3.57 ml.min^{-1}.cm^{-2} at a methane flow rate of 20 ml.min^{-1}. The oxygen permeation flux of the SSC OTM with the additional catalyst layer is a slightly higher value compared to the SSC membrane without a catalyst, which only achieved an oxygen permeation flux of 2.75 mL·min^{-1}·cm^{-2} at 900°C while subjected to a methane flow rate of 20 ml.min^{-1}. The higher oxygen permeation flux obtained by the SSC OTM with the additional catalyst layer compared to the blank SSC planar OTM is due to the porosity of the applied catalyst layer enhancing the surface exchange reaction sites on the air feed side of the OTM.

Figure 4.5 shows the improvement of CO_2 selectivity of the SSC planar OTM with the additional catalyst layer with an increase in membrane temperature and a decrease in methane flow rate. For example, the SSC planar reactor with a catalyst layer achieved a maximum CO_2 selectivity of 98% under a membrane temperature of 900˚C and methane flow rate of 2 $mL \cdot min^{-1}$ A minimum CO_2 selectivity of 84% was discovered at a membrane temperature of 800˚C with a methane flow rate of 20 $mL \cdot min^{-1}$. As the membrane temperature increases, the CO_2 selectivity increases due to the improvement in the oxygen permeation flux while maintaining a constant methane flow rate. As the methane flow rate increases, while maintaining a constant membrane temperature, the volume ratio between then incoming methane and permeating oxygen becomes disproportionate, signifying a richer combustion and a decrease in the CO_2 selectivity.

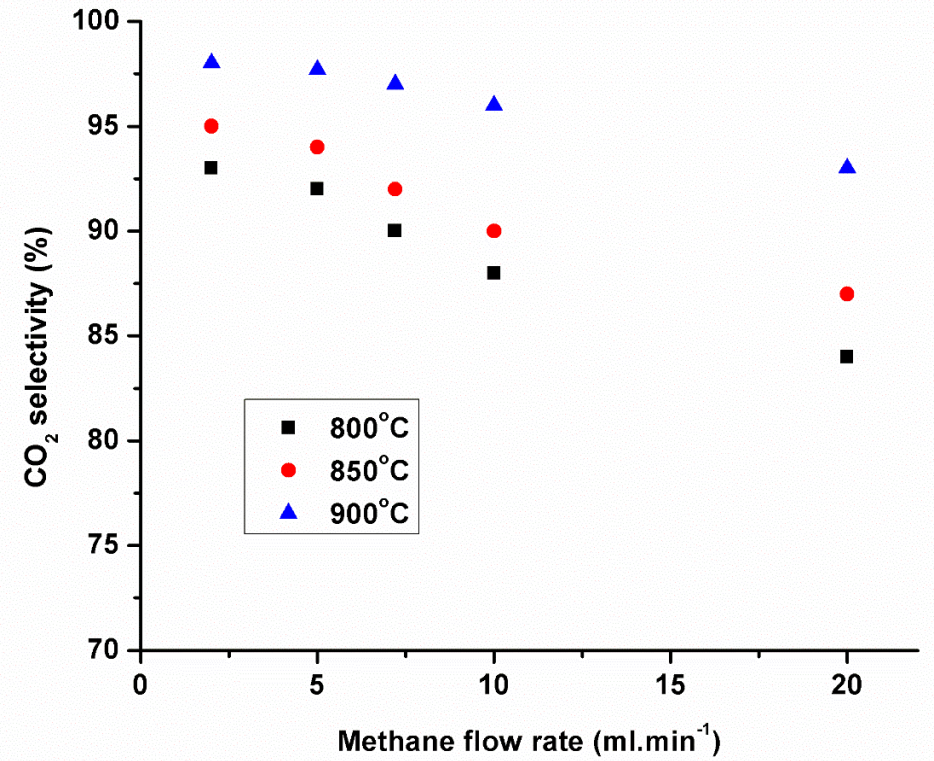

Figure 4.5 CO_2 selectivity of SSC planar OTM with an additional porous catalyst layer subjected to methane flow rates ranging from 2 to 20 $ml.min^{-1}$ while held at membrane temperatures ranging from 800 to 900°C

4.3.2 Tubular OTM Investigation

Planar OTMs is a simple configuration to determine the oxygen permeation flux and CO_2 selectivity of perovskite-type materials utilized for the application of oxy-fuel combustion. However, planar OTMs are not a practical solution when implemented in power generation facilities due to the substantial costs and size needed to provide sufficient volumes of oxygen for complete combustion. Alternative to planar OTMs used for experimental investigation, tubular OTMs are a practical approach when implementing this technology and already have been in some instances [116]. OTMs in a tubular configuration has the major advantage of delivering large volumes of oxygen within compact spaces because of the improved surface to volume ratio; a planar membrane with a large surface area would occupy a larger space compared to a membrane with a tubular structure with the same surface area. Therefore, tubular OTMs were fabricated using an LSFC composition. Although SSC showed a superior oxygen permeation performance, LSCF was selected material to determine the impact of OTM configurations due to its abundance and availability.

Figure 4.6 depicts the difference between tubular and planar LSCF membranes with the same effective surface area (0.65 cm^{-2}) and membrane thickness (1.1 mm). The membranes were held at a constant temperature of 900°C and fed methane at varying flow rates ranging from 2 to 20 $ml.min^{-1}$ onto the permeation side of the OTM. Similar to previous figures, the increase of methane flow rate enhances the oxygen permeation performance by improving the oxygen chemical gradient across the membrane and maintaining a low oxygen partial pressure on the permeation side. At the same thickness and effective surface area, the planar and tubular OTMs are shown to exhibit consistent oxygen permeation flux results. However, the oxygen permeation flux for the planar membrane in Fig 4.6 (thickness 1.1 mm) is lower compared to the planar OTM results

shown in Fig. 4.3 (thickness 0.44). The difference in the oxygen permeation flux is a result of the increased membrane thickness of LSCF OTMs. The increased membrane thickness reduces the chemical gradient across the OTM and diminishes the oxygen permeation flux. Although the planar OTMs can be fabricated with a thinner membrane thickness, tubular OTMs require a greater membrane thickness to maintain their mechanical integrity.

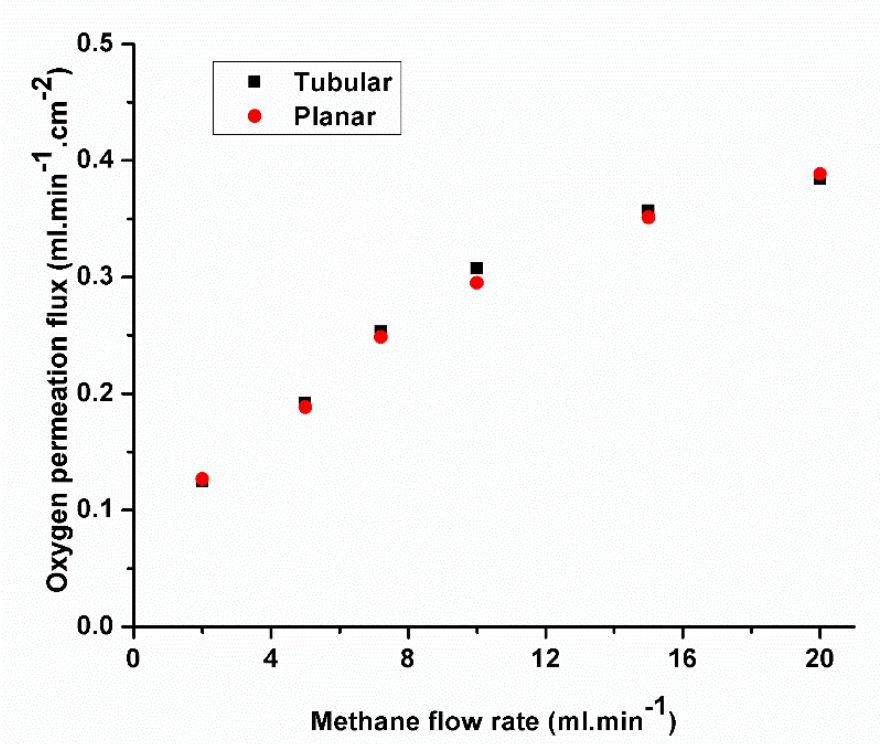

Figure 4.6 Oxygen permeation flux of LSCF planar and tubular OTM subjected to methane flow rates ranging from 2 to 20 ml.min^{-1} while held at membrane temperatures of 900°C

The difference in the oxygen permeation flux reveals a critical limitation of tubular OTMs. OTM performance is driven by the oxygen chemical gradient across the reactor, wherein the case of an increased membrane thickness would diminish the gradient and reduce the oxygen permeation flux. Since the tubular reactor exhibited a uniform thickness of 1.1 mm, while the initial planar reactor had a thickness of 0.44 mm, the oxygen permeation flux was diminished. The thickness of tubular membranes could be reduced using the fabrication techniques described previously, but heighten the risk of fracturing when subjected to high temperatures. Therefore,

despite tubular membranes having the potential to exhibit higher surface to volume ratios, in this study, they are limited by the thickness needed to maintain their mechanical structure, thus sacrificing the oxygen permeation of the reactor.

Despite the lower oxygen permeation flux compared to the planar reactor, the tubular reactor exhaust composition provided some insight into the feasibility of integrating OTM technology into combustion systems. The LSCF tubular OTM with a thickness of 1.1 mm was investigated using the same conditions applied to previously studied planar OTMs. The membrane temperature was varied from 800 to 900°C while the methane flow rate ranged from 2 to 20 $ml.min^{-1}$. As seen in Fig. 4.7, the oxygen permeation flux of the LSCF tubular OTM directly increases with membrane temperature and methane flow rate, similar to the trends seen in previous figures. The oxygen permeation performance of the LSCF tubular reactor is still lower than the LSCF planar reactor with the thinner membrane thickness. At a membrane temperature of 900°C while subjected to a methane flow rate of 20 $mL \cdot min^{-1}$, the LSCF tubular OTM achieved a maximum oxygen permeation flux of 0.38 $mL \cdot min^{-1} \cdot cm^{-2}$.

Although the oxygen permeation flux was lower for the LSCF tubular OTM compared to the thinner LSCF planar OTM, the LSCF tubular OTM was able to exhibit a similar CO_2 selectivity to the SSC planar OTM with an additional catalyst layer. Fig 4.8 shows the CO_2 selectivity of the LSCF tubular OTM subjected to the same conditions corresponding to the oxygen permeation flux result found in Fig. 4.7. It can be seen from Fig. 4.8 that the membrane temperature and methane flow rate influences the CO_2 selectivity, similar to trends seen in Fig. 4.5.

The CO_2 selectivity is found to increase directly with an increase in membrane temperature. However, the CO_2 selectivity is found to decrease with an increase in methane flow rate indirectly. At 900°C and a methane flow rate of 2 $ml.min^{-1}$, the maximum CO_2 selectivity was found to be

88%, while found to be 70% for a methane flow rate of 20 mL·min^{-1}. The difference in the CO_2 selectivity with a change in methane flow rate stems from the combustion occurring between the permeating oxygen and incoming methane. As the methane flow rate is lowered, the volume of permeated oxygen becomes enough to cause a leaner reaction. This allows the OTM to host a combustion with a more equalized ratio between the fuel and oxidant, hence the increase in CO_2 selectivity. As the flow rate is increased, the flow stream becomes rich and the CO_2 selectivity decreases. Furthermore, in comparison to the CO_2 selectivity results of the SSC planar OTM with the additional catalyst layer, the tubular LSCF OTM still demonstrates a CO_2 exhaust with most the converted methane being CO_2. The combustion performance of the tubular OTM indicates that although the tubular cell sacrifices oxygen permeation performance needed for maintaining its mechanical structure, it can still produce an exhaust in which the majority of the converted methane is CO_2, signifying the potential to achieve a complete combustion if designed appropriately.

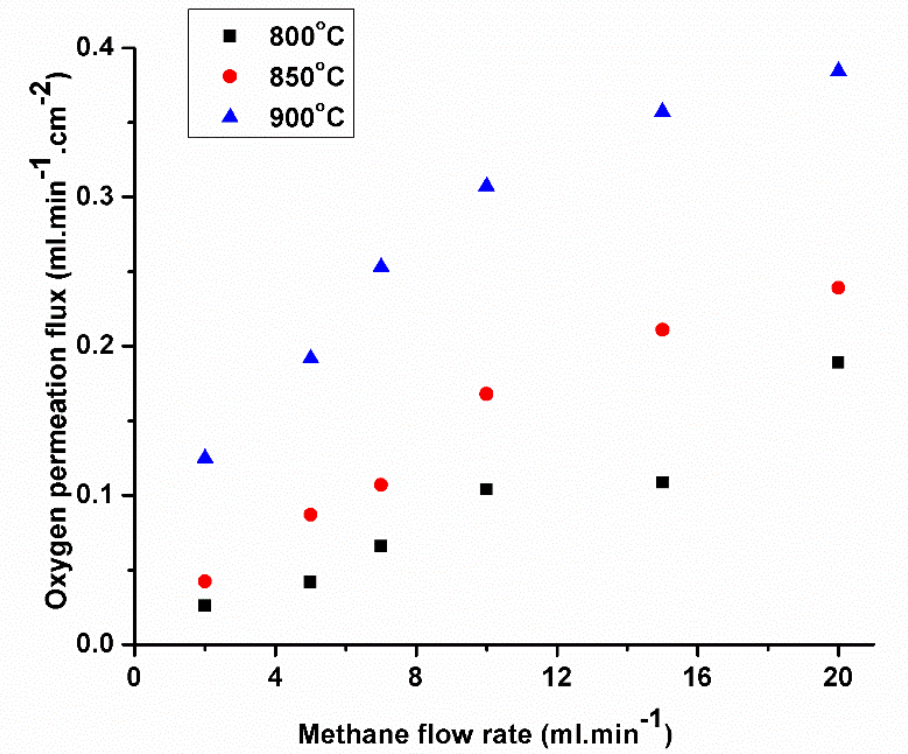

Figure 4.7 Oxygen permeation flux of LSCF tubular OTM subjected to methane flow rates ranging from 2 to 20 ml.min^{-1} while held at membrane temperatures ranging from 800 to 900°C

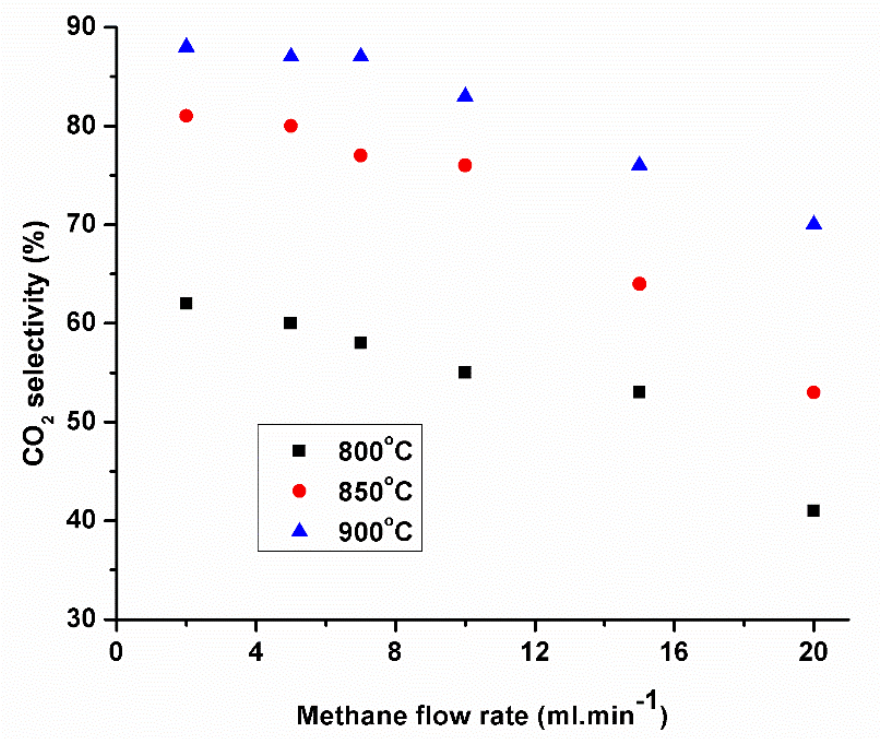

Figure 4.8 CO_2 selectivity of LSCF tubular OTM subjected to methane flow rates ranging from 2 to 20 ml.min^{-1} while held at membrane temperatures ranging from 800 to 900°C

4.4 Conclusion

The presented work in this chapter introduces an OTM used for methane combustion processes with the purpose of capturing carbon from the exhaust stream. This work provides a detailed analysis of critical components and practical limitations that influence the oxygen permeation flux and CO_2 selectivity performance including membrane temperature, methane flow rate, reactor configuration, and material composition. It was shown that for both planar and tubular reactor designs both temperature and sweeping gas flow rates improved the oxygen permeation flux.

At the same membrane thickness and the effective surface area, it was revealed that the oxygen permeation flux of the SSC planar OTM, under all operating conditions, was higher than the oxygen permeation performance of LSCF planar OTM, a commonly studied composition. The application of a catalyst layer also enhanced the performance of an SSC planar OTM, achieving an oxygen permeation flux of 3.57 mL·min^{-1}·cm^{-2} and a CO_2 selectivity of 98%.

Tubular OTMs were explored using a commonly available material. It was discovered that due to the tubular reactor's greater thickness, needed to maintain the mechanical structure; the oxygen permeation flux was lower than the results found in the thinner LSCF planar reactor. However, at the same thickness, the planar and tubular LSCF OTMs were found to exhibit the same oxygen permeation flux, signifying the advantage of the lower surface to volume ratio of the tubular OTM. Upon further examination, the tubular OTM was found to exhibit similar effects of the varying methane flow rates and membrane temperatures on the oxygen permeation and CO_2 selectivity. This work provides the foundation needed to further the development of OTM technology for oxy-fuel combustion processes and carbon capture purposes.

Chapter 5 Studying the behavior of dual-phase oxygen transport membranes with high concentrations of CO_2 exposure

5.1 Introduction

Oxygen transport membrane reactors (OTMs) have the potential to reduce oxygen production costs due to their ability to permeate oxygen without the need for external circuitry. As shown in Chapter 4, oxygen permeability is achieved when the OTM is held at elevated temperatures ($\geq$800°C), while introducing fuel onto the permeation side of the dense OTM. The permeated oxygen then combusts with the incoming fuel in a nitrogen-free environment, thus separating the CO_2 in the product stream from nitrogen in the surrounding atmosphere and simplifying the carbon capture process. Despite its novelty, OTMs have some restrictions that could potentially limit its application.

As previously discussed, OTMs are comprised of perovskite materials with the chemical structure ($ABO_{3-\delta}$) in which the partial substitution of both A and B cations in its lattice structure enhances the electronic and ionic conductivity of the material. The improved ionic and electronic conductivity allows oxygen ions and electrons to move through the membrane and maintain the permeation process. In the presence of abundant CO_2 atmospheres, the A cation, mainly comprised of alkaline earth metals, has the potential to form carbonate with the surrounding environment, ultimately jeopardizing the stability of OTMs. Consequently, the formation of carbonates also causes the B site ion to create an additional oxide structure which could preserve electron transmissions [97]. In some studies, the A or B sites in the perovskite structure have been modified to produce OTMs with a high chemical stability when exposed to CO_2 atmospheres [164–166]. For these newly developed materials, a CO_2-tolerant material is created, but at the expense of the

ionic and electronic conductivity, ultimately eliminating the potential to be implemented for the application of oxy-fuel combustion.

An alternative approach is dual-phase OTMs, which have the potential to sustain an oxygen permeation flux in a CO_2 atmosphere without jeopardizing the chemical or mechanical integrity of the membrane. As discussed in Chapter 2, dual-phase OTMs combine a high performing perovskite-type oxide with a CO_2-tolerant and ionically conductive additive material. The additive ionic conductive material provides a pathway for oxygen ions when the perovskite materials are compromised. The electron conductivity is still preserved in the compromised perovskite-type material through the -O-B-O-B-O- pathways (Fig 2.3). In this instance, OTMs could provide an oxygen permeation flux and chemical stability while exposed to a high concentration of CO_2.

In this chapter, the effect of CO_2 sweeping gases on dual-phase OTM's properties, such as morphology, phase structure, conductivity, and oxygen permeation flux is reported. The objectives of this chapter are as follows: (1) investigate the influence that CO_2 atmospheres have on the perovskite-type structure; (2) understand how the addition of a CO_2-tolerant and ionically conductive additive material enhances the oxygen permeation performance and chemical stability of the OTM; and (3) examine the oxygen permeation flux using a CO_2 sweeping gas while modifying the surrounding conditions (i.e. membrane temperature and sweeping gas flow rate).

5.2 Experimental methods

Chapters 3 and 4 demonstrated $SrSc_{0.1}Co_{0.9}O_{3-\delta}$'s (SSC) superior oxygen permeation flux and electrochemical properties compared to other commonly studied perovskite-type materials. Therefore, SSC was selected as the perovskite-type material in this chapter. $Sm_{0.2}Ce_{0.8}O_{1.9-\delta}$ (SDC), was selected as the additive material due to its previously reported CO_2 tolerance, ionic conductivity, and compatibility with perovskite-type materials [47,113,114]. SSC powders were

synthesized by a combined EDTA-citrate complexing sol-gel process as described in detail in Chapter 3. SDC powders were purchased from an external source (i.e., fuelcellmaterials.com) [167].

After obtaining both powders, a portion of SDC was added based on a weight percentage (wt.%) of the total powder mixture. The wt.% of SDC was varied in increments of 10 wt.%, ranging from 0 to 50 SDC wt.%. The proportioned SDC and SSC materials were mixed using a ball-milling technique that produced a well-mixed blended powder. The mixed powder was pressed into thin disk shape membranes to be used for oxygen permeation testing with a diameter of 12~13 mm and thickness of 0.44 mm. Additionally, mixed SSC and SDC powders were pressed into bar samples of approximate dimensions 15x4x4 mm for total conductivity testing. All fabricated samples were sintered in a Nabertherm High-Temperature Furnace at 1200°C for 5 hours in an air atmosphere.

The total conductivity of a pure SSC OTM was measured using the same four-probe method set-up as described in Chapter 3. The total conductivity of the pure SSC bar sample was measured before and after exposure to a CO_2 atmosphere while held at a constant temperature of 900°C for 60 hours. The total conductivity was measured in air with an increase in temperature ranging from 300°C to 900°C at a rate of 1°C/min.

The oxygen permeation flux of OTMs with varying dual-phase compositions, including a pure SSC composition, was investigated using a pure CO_2 sweeping gas. The experimental setup is shown in Fig. 5.1, demonstrating a similar permeation test setup as used in Chapter 4. The oxygen permeation flux was investigated at varying membrane temperatures ranging from 800°C to 900°C and at different pure CO_2 sweeping gas flow rates ranging from 20 to 80 $ml.min^{-1}$. The feed side of the membrane sample was exposed to ambient air. All oxygen permeation tests were conducted over a 50 or 60-hour period in which the membrane temperature and sweeping gas flow rate

remained constant. GC readings were collected every 12 minutes for the entire duration of the oxygen permeation tests. The oxygen permeation flux (J_{O_2}) was calculated using Eq. 4.1:

$$J_{O_2} = \dot{F}_{total}(X''_{O_2})/S \qquad \text{(Eq. 5.1)}$$

where, $\dot{F}_{total}$ is the volumetric flow rate of the sweeping gas defined by the mass flow controller, X''_{O_2} is the molar fraction of oxygen detected in the GC, and S is the effective surface area of the planar membrane.

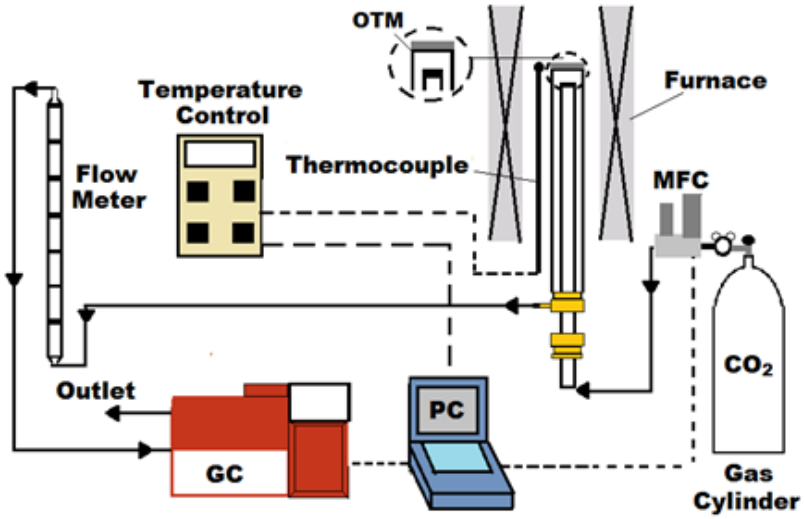

Figure 5.1 Experimental setup for oxygen permeation experiments with a CO_2 sweeping gas

After oxygen permeation testing, investigated samples were examined using an SEM, which studied the membrane permeation surface and cross-section. Furthermore, the chemical structure of the investigated sample's permeation surface was analyzed using an XRD. In some instances, oxygen permeation experiments were repeated using the same membrane composition, membrane temperature, and CO_2 sweeping gas flow rate while modifying the CO_2 exposure times. The produced OTMs samples with different CO_2 exposure times were investigated using an SEM and XRD, therefore providing a deeper insight into the carbonate formation on the membrane over time.

5.3 Results and discussion

5.3.1 Oxygen permeation flux comparison of dual-phase OTM compositions when subjected to CO_2 atmospheres

Figure 5.2 shows the XRD pattern of an SSC OTM's permeation surface at different durations of exposure to a CO_2 sweeping gas with a flow rate of 80 ml.min^{-1} while maintained at a membrane temperature of 900°C. As displayed in Fig. 5.2, the $SrCO_3$ pattern matches well with the additional peaks that appear in the diffraction pattern of the SSC OTM's permeation surface after exposure to CO_2. The presence of additional peaks in the diffraction patterns, identified as $SrCO_3$, confirm the phase transformation on the pure SSC OTM's permeation surface from the CO_2 sweeping gas.

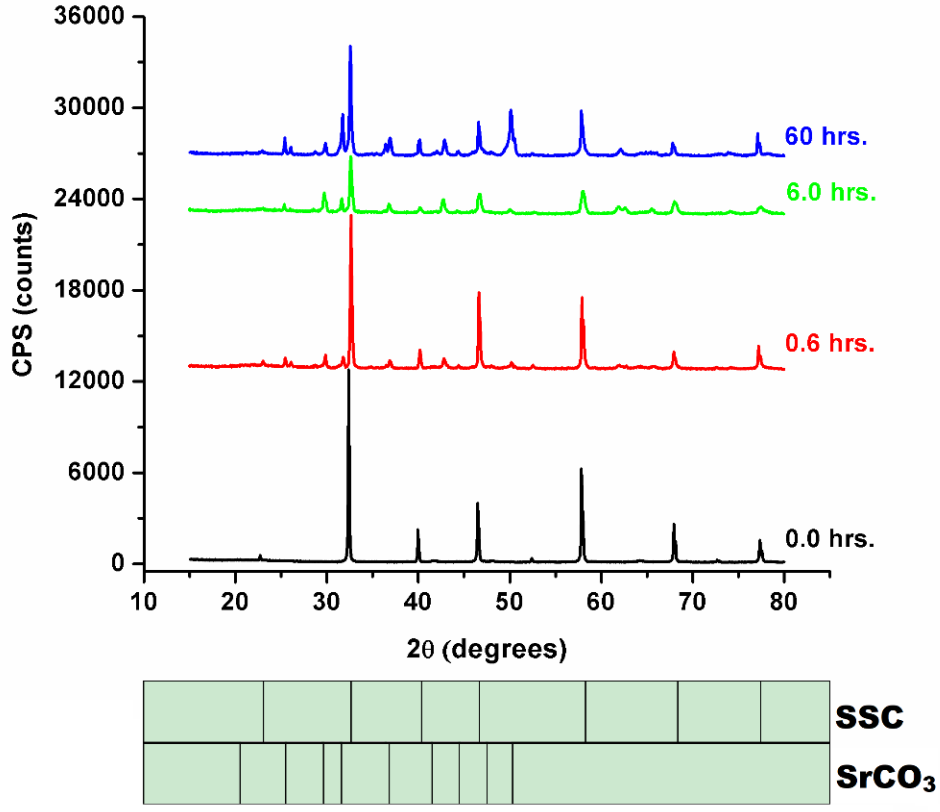

Figure 5.2 XRD diffraction patterns of the pure SSC permeation surface after exposure to a CO_2 sweeping gas with flow rate 80 ml.min^{-1} while held at 900°C for 0.0, 0.6, 6.0, and 60 hours

The carbonate formation on the permeation was observed to modify the morphology of the SSC material after exposure to CO_2. Figure 5.3 displays the surface and cross sections of a pure

SSC OTM before and after exposure to a CO_2 sweeping gas with a flow rate of 80 ml.min^{-1} while held at a membrane temperature of 900°C for 60 hours. The permeation surface, shown in Fig 5.3b, corresponds to the XRD pattern shown in Fig 5.2 after 60 hours of CO_2 exposure, indicating the degraded surface morphology is a result of the phase transformation from CO_2 exposure. Compared to the permeation surface of an untested pure SSC OTM (Fig 5.3a), the permeation surface of a pure SSC OTM after exposure to CO_2 for 60 hours is observed to be an uneven porous surface that lacks the dense mechanical integrity needed to separate oxygen from the surrounding air. Furthermore, the pure SSC OTMs thickness is shown to have increased to approximately 1.6 mm after exposure to CO_2 at a flow rate of 80 ml.min^{-1} while held at a membrane temperature of 900°C. In comparison, an untested pure SSC OTM's cross section (Fig. 5.3c) is approximately 0.44 mm. The modified morphology observed in Fig. 5.3b and 5.3d indicate that the carbonate formation on the SSC material caused inflammation throughout the entire membrane, ultimately compromising the overall structure.

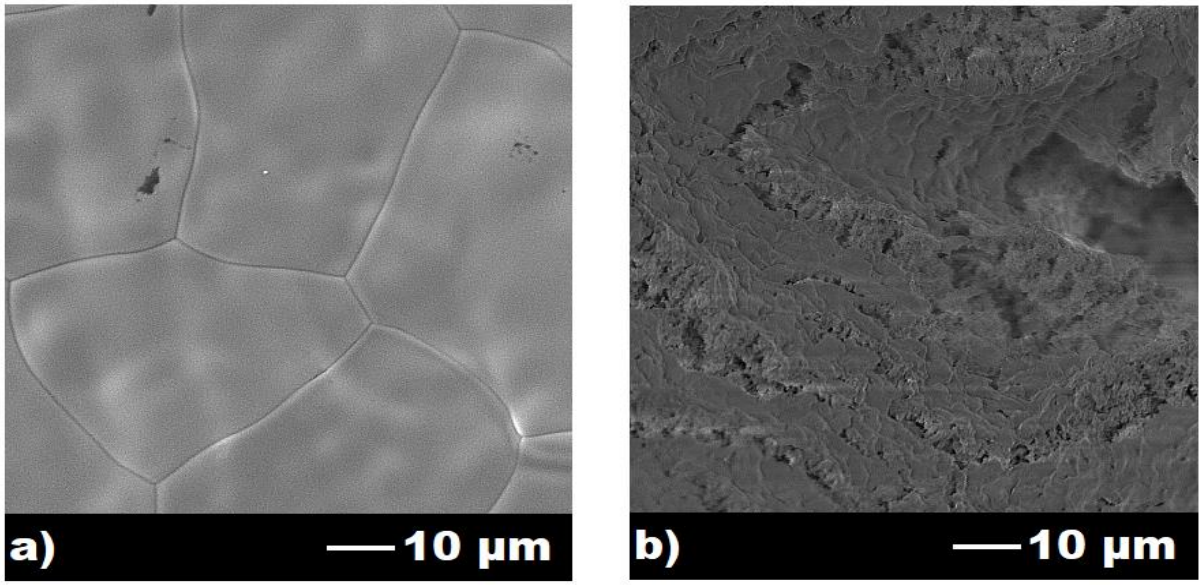

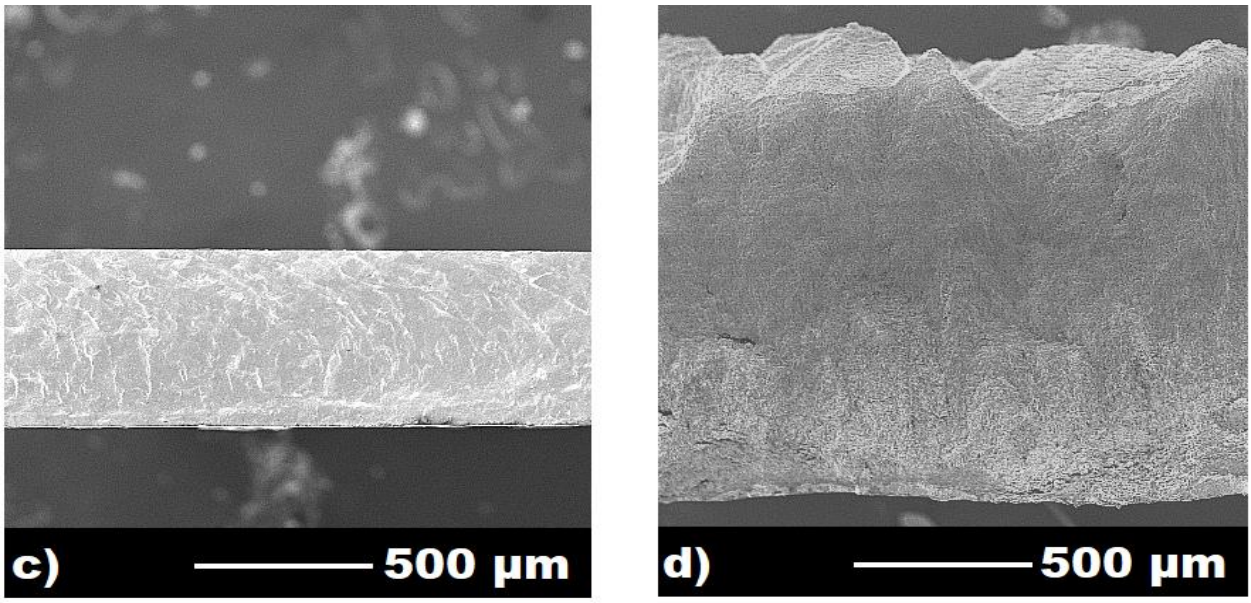

Figure 5.3 SEM images of newly sintered SSC OTM's surface (a) and cross section (b) and a pure SSC OTM's surface (b) and cross section (d) after exposure to a CO_2 sweeping gas with a flow rate of 80 ml.min^{-1} while held at a membrane temperature of 900°C for 60 hours

The carbonate formation throughout the entire SSC membrane is also shown to impact the perovskite-type material's total conductivity (ionic and electronic conductivity). Figure 5.4 shows the total conductivity of the pure SSC membrane before and after exposure to a CO_2 atmosphere at 900°C for 60 hours. The total conductivity before and after CO_2 exposure is found to initially increase, reaching a maximum total conductivity of 225.99 S.cm^{-1} at 454°C and 32.77 S.cm^{-1} at 401°C, respectively. The initial rise in conductivity up to approximately 450°C is attributed to the perovskite membranes p-type semi-conductivity, of which there is a transition at high temperature due to the reduction of Co^{+4} to Co^{+3} or Sc^{+3} to Sc^{+2} [168,169]. For higher temperatures, the perovskite-type material deviates from p-type semi-conductivity to a metal-like conductivity for which the total conductivity decreases. Figure 5.4 also shows that after exposure to a CO_2 atmosphere for 60 hours at 900°C, the total conductivity of the SSC material decreases. The difference between the total conductivity before and after CO_2 exposure suggests that the carbonate formation on the SSC material compromises the perovskite structures ability to needed to maintain electronic pathways. Although the total conductivity is reduced after the SSC material is exposed

to a CO_2 atmosphere, it is not completely diminished, suggesting the preservation of some electron pathways and justifying the use of dual-phase OTMs to improve the oxygen permeation flux in CO_2 atmospheres.

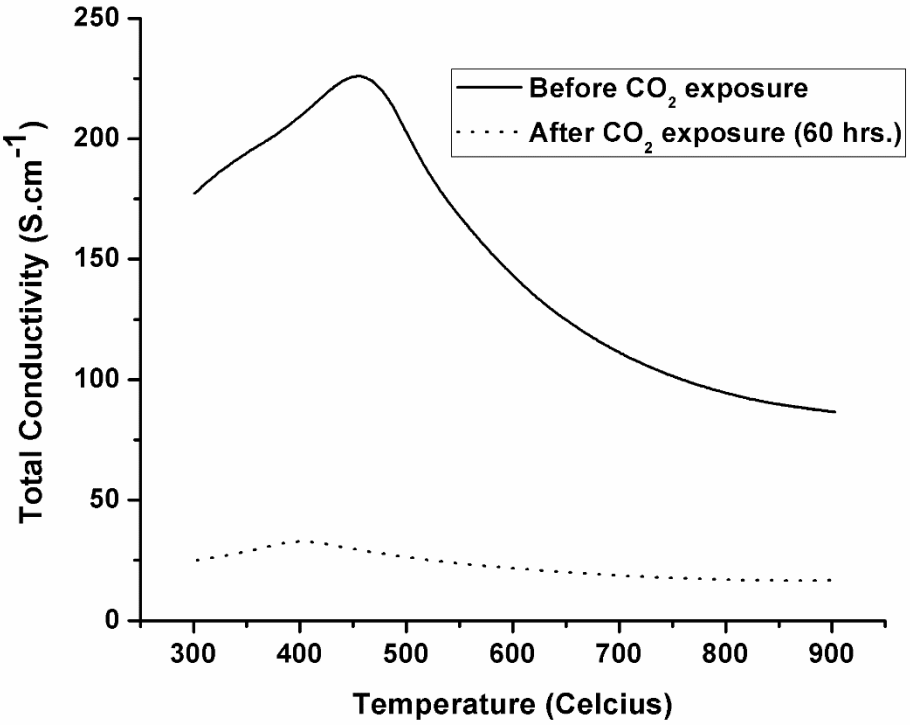

Figure 5.4 Temperature dependence of total conductivity in air of a pure SSC sample before and after exposure to a CO_2 atmosphere at 900°C

The oxygen permeation flux of SSC/SDC dual-phase OTMs comprised of varying SDC wt.% ranging from 0 to 50 wt.% SDC was investigated for 60 hours using a pure CO_2 sweeping gas with a flow rate of 80 ml.min^{-1} while held at membrane temperature of 900°C. The resulting oxygen permeation fluxes are shown in Fig. 5.5 for each dual-phase OTM composition including the pure SSC OTM. The highest oxygen permeation flux after the 60-hour permeation test was achieved by the 30 wt.% SDC-70 wt.% SSC (30SDC-70SSC) dual-phase OTM which exhibited a steady oxygen permeation flux of 0.73 ml.min^{-1}.cm^{-2} for the last 30 hours of the experiment. Compared to other oxygen permeation fluxes reported in the literature, the steady oxygen permeation flux of the 30SDC-70SSC dual-phase OTM, achieved after the 60-hour permeation test, is higher

[49,58,80,83–90,92–95,98–112,170–173]. The superior and steady oxygen permeation flux of the 30SDC-70SSC dual-phase OTM indicates a relatively high performing composition which could potentially be utilized for the application of oxy-fuel combustion.

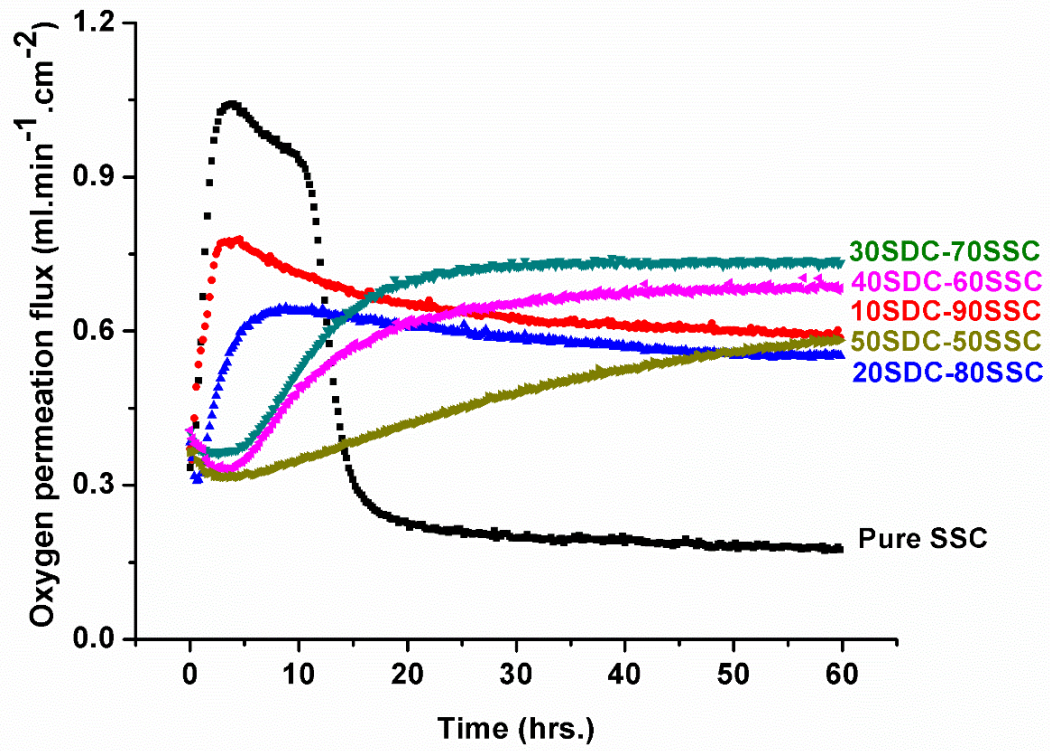

Figure 5.5 Unsteady oxygen permeation flux of dual-phase OTMs with varying compositions ranging from 0 to 50 wt.% SDC while subjected to a CO_2 sweeping gas with a flow rate of 80 $ml.min^{-1}$ while held at a membrane temperature of 900°C for 60 hours

Looking further into Fig. 5.5, it is difficult to determine the effect that the additional SDC wt.% in the dual-phase OTM composition has on the oxygen permeation flux exposed to a pure CO_2 sweeping gas. Figure 5.6 offsets the oxygen permeation flux curves shown in Fig 5.5 of each dual-phase OTM composition subjected to a pure CO_2 sweeping gas with a flow rate of 80 $ml.min^{-1}$ while held at a membrane temperature of 900°C for 60 hours. The offset oxygen permeation flux curves shown in Fig. 5.6 provide a deeper insight into how the oxygen permeation flux is modify with varying dual-phase compositions while exposed to a CO_2 atmosphere. In Fig. 5.6, it is observed that the oxygen permeation flux curves for each dual-phase OTM composition consists

of two regions: 1) a rise in the oxygen permeation flux and 2) a fluctuating period in which the oxygen permeation flux declines or remains steady. The oxygen permeation flux results for the pure SSC, 10SDC-90SSC, and the 20SDC-80SSC OTMs are found to decline after achieving a maximum flux. The 30SDC-70SSC and 40SDC-60SSC OTMs are found to achieve a steady oxygen permeation flux at their respective maximum fluxes after approximately 30 hours into the permeation test. The 50SDC-50SSC OTM is shown to continually increase during the duration of the permeation test, reaching a maximum oxygen permeation flux at 60 hours.

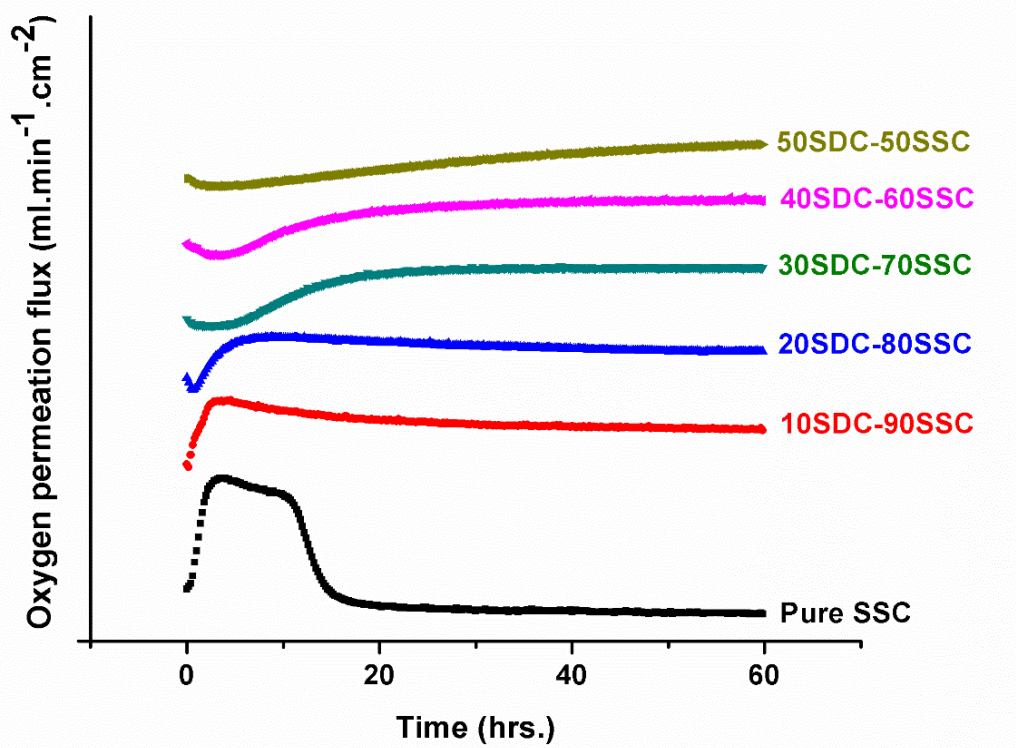

Figure 5.6 The offset curves of the unsteady oxygen permeation flux of dual-phase OTMs with varying compositions ranging from 0 to 50 wt.% SDC while subjected to a CO_2 sweeping gas with a flow rate of 80 ml.min^{-1} while held at a membrane temperature of 900°C for 60 hours

The fluctuating oxygen permeation performances of the various OTM compositions is linked to the membrane morphology of the OTM. Figure 5.7 displays the cross sections of SSC/SDC dual-phase OTMs comprised of varying SDC wt.% ranging from 10 to 50 wt.% SDC subjected to a pure CO_2 sweeping gas with a flow rate of 80 ml.min^{-1} while held at membrane temperature of

900°C for 60 hours. The compositions in which exhibited a declining oxygen permeation flux after reaching a maximum value (10SDC-90SSC and 20SDC-80SSC dual-phase OTMs) are shown to have most of their internal cross-section compromised by the phase transformation. The compromised cross sections of the 10SDC-90SSC (Fig 5.7a) and 20SDC-80SSC (Fig 5.7b) dual-phase OTMs are similar to the cross-section of the pure SSC OTM under the same conditions (Fig. 5.3d). The cross-sections of the 30SDC-70SSC and 40SDC-60SSC dual-phase OTMs after 60 hours of CO_2 exposure are observed to have a defined carbonate layer in which much of the uncompromised dual-phase membrane remains intact. The 50SDC-50SSC dual-phase OTM is found to have limited sites of which portions of the permeation surface is compromised.

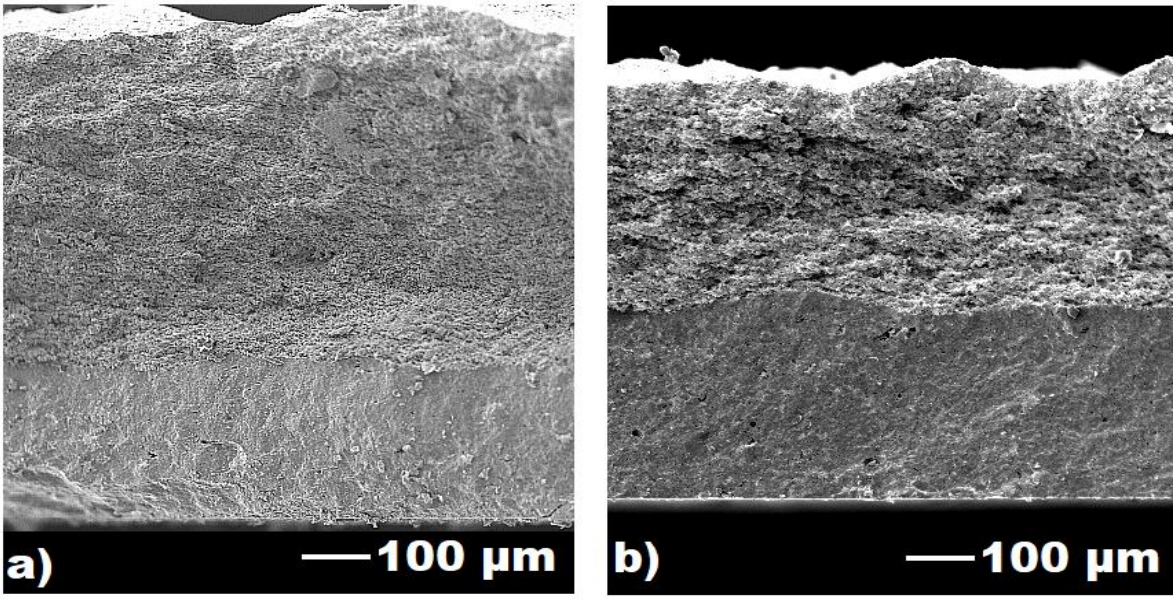

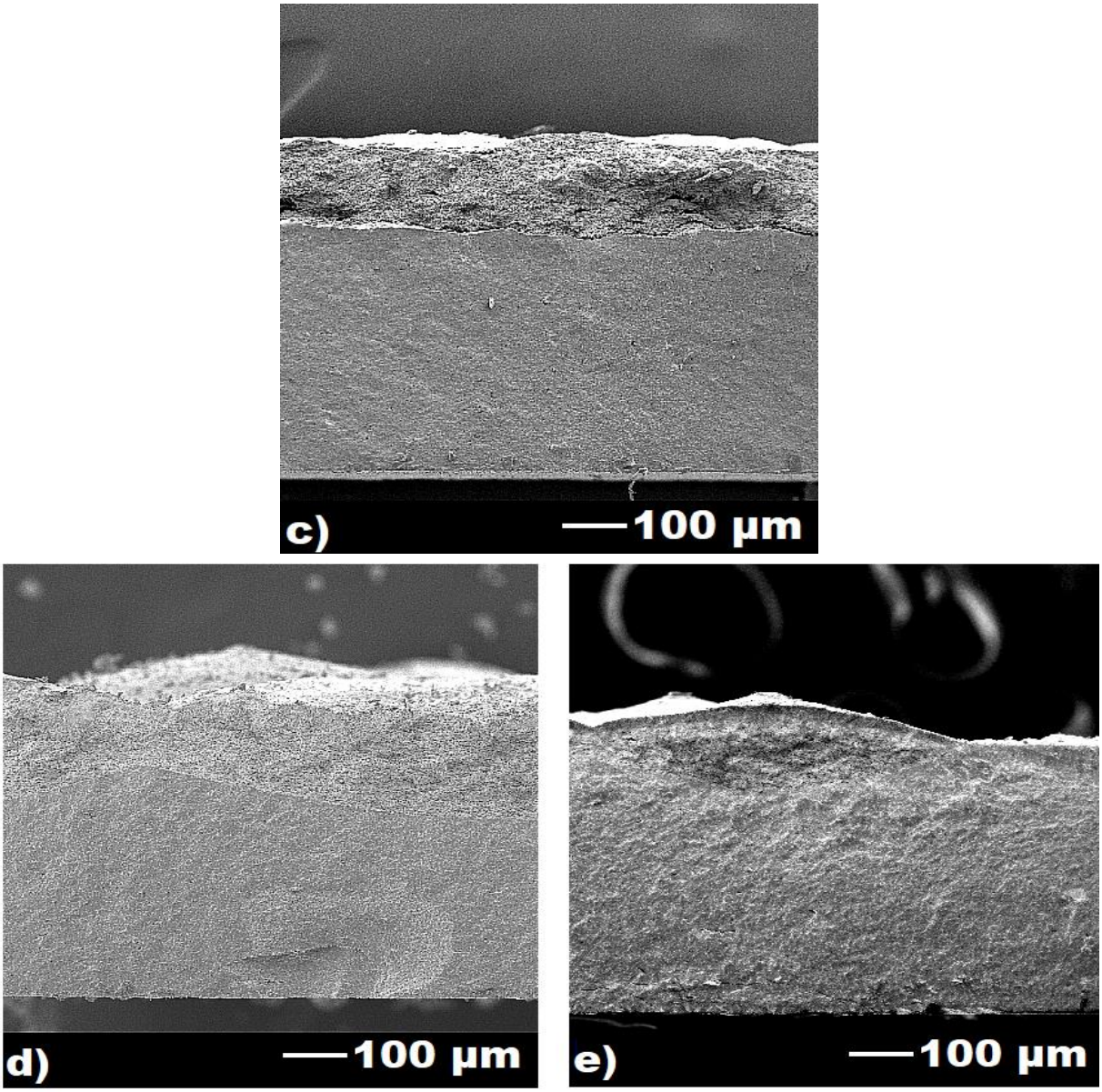

Figure 5.7 SEM images of the cross sections of all dual-phase membrane compositions (10SDC-90SSC (a) to 50 SDC-50SSC (e)) after subjected to a CO_2 sweeping gas with a flow rate of 80 $ml.min^{-1}$ while held at a membrane temperature of 900°C for 60 hours

The variation in the uncompromised membrane thickness also contributes to the oxygen permeation flux. As the carbonate forms on the permeation surface, the uncompromised membrane thickness decreases, thus gradually improving the oxygen chemical gradient across the uncompromised membrane. Therefore, the initial rise of the oxygen permeation flux shown in Fig.

5.5 and 5.6, hereby referred to as the rise region, is attributed to the formation of the carbonate layer on the permeation surface.

The growth of the carbonate layer (i.e., phase transformation) on the permeation surface of the OTM is a result of heterogeneous nucleation. Initially, heterogeneous nucleation occurs on the OTM surface, in which the SSC material exposed to the CO_2 atmospheres begins to form into $SrCO_3$, as observed from the XRD pattern in Fig. 5.2. Once the newly created structure is large enough, the carbonate will start to grow new phase particles by combining with the SSC material within the OTM, ultimately creating an additional carbonate layer on the permeation surface that protrudes into the internal cross-section. As the carbonate layer grows larger the inner cross-section of the membrane decreases, thus reducing the chemical gradient across the OTM and increasing the oxygen permeation flux observed in the rise region of Fig. 5.5 and 5.6.

A more in-depth insight into the relationship between the carbonate growth and dual-phase composition can be seen in Table 5.1, which shows the rate at which the oxygen permeation flux increases within the rise region. From Table 5.1, the rate at which the oxygen permeation flux increases in the rise region is found to decrease with the addition of SDC in the dual-phase composition. As previously discussed, the increase in the oxygen permeation flux is a result of the carbonate formation reducing the uncompromised membrane thickness and thus increasing the oxygen chemical gradient across the OTM. The presence of SDC in the dual-phase OTM composition reduces the nucleation sites between the CO_2 sweeping gas and permeation surface. This is supported in Fig. 5.7e which shows the cross-section of the 50SDC-50SSC dual-phase OTM after exposure to CO_2 sweeping gas with a flow rate of 80 $ml.min^{-1}$ while held at a membrane temperature of 900°C for 60 hours. As previously described, the 50SDC-50SSC dual-phase OTM is observed to have limited regions of the carbonate formation on the permeation surface while

maintaining some of the internal uncompromised membrane structure after exposure to CO_2 for 60 hours. As a result of the delayed formation, the rise region duration is found to be relatively long compared to other dual-phase compositions, since the additional SDC in the composition is delaying the carbonate growth on the permeation surface.

Table 5.1 The rate of change in the oxygen permeation flux of the dual-phase OTMs with varying compositions ranging from 0 to 50 wt.% SDC within the rise region

	Pure SSC	**10SDC-90SSC**	**20SDC-80SSC**	**30SDC-70SSC**	**40SDC-60SSC**	**50SDC-50SSC**
$\frac{dJ_{O_2}}{dt}$	2.1E-1	1.1E-1	4.1E-2	1.1E-2	6.6E-3	4.9E-3

The additional SDC in the dual-phase composition is also observed to mitigate the carbonate growth from protruding into the internal membrane structure. Fig. 5.8 shows the cross sections of a 30SDC-70SSC dual-phase OTM after subjected to a CO_2 sweeping gas with a flow rate of 80 $ml.min^{-1}$ while held at a membrane temperature of 900°C for 50 and 60 hours. At both 50 hours (Fig. 5.8a) and 60 hours (Fig. 5.8b) of CO_2 exposure, the cross sections are observed to exhibit uncompromised layers with the same approximate thickness (~448.5μm). However, the carbonate layer is found to have continually grown over the 10-hour, forming a thick layer on the permeation surface of the 30SDC-70SSC dual-phase OTM after 50 (Fig. 5.9a) and 60 hours (Fig 5.9b) of CO_2 exposure. The thick carbonate layer prevents the interaction between the uncompromised membrane and the CO_2 sweeping gas, eliminates any further nucleation from occurring on the uncompromised material. Thus, a substantial portion of the permeation surface is consistently maintained resulting in a steady oxygen permeation flux. Furthermore, the preserved uncompromised membrane thickness along with the high SSC composition results in the 30SDC-70SSC to exhibit the highest oxygen permeation flux when subjected to CO_2 atmospheres.

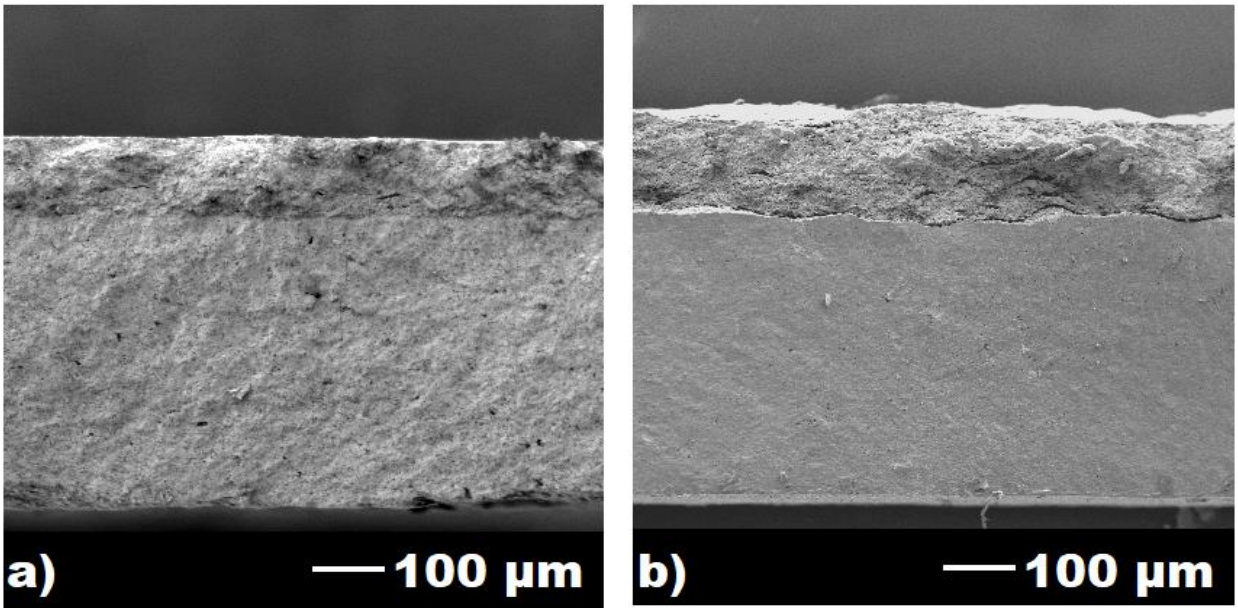

Figure 5.8 SEM images of a 30SDC-70SSC dual-phase OTM's cross section after exposure to a CO_2 sweeping gas with a flow rate of 80 ml.min^{-1} while held at a membrane temperature of 900°C for 50 (a) and 60 (b) hours

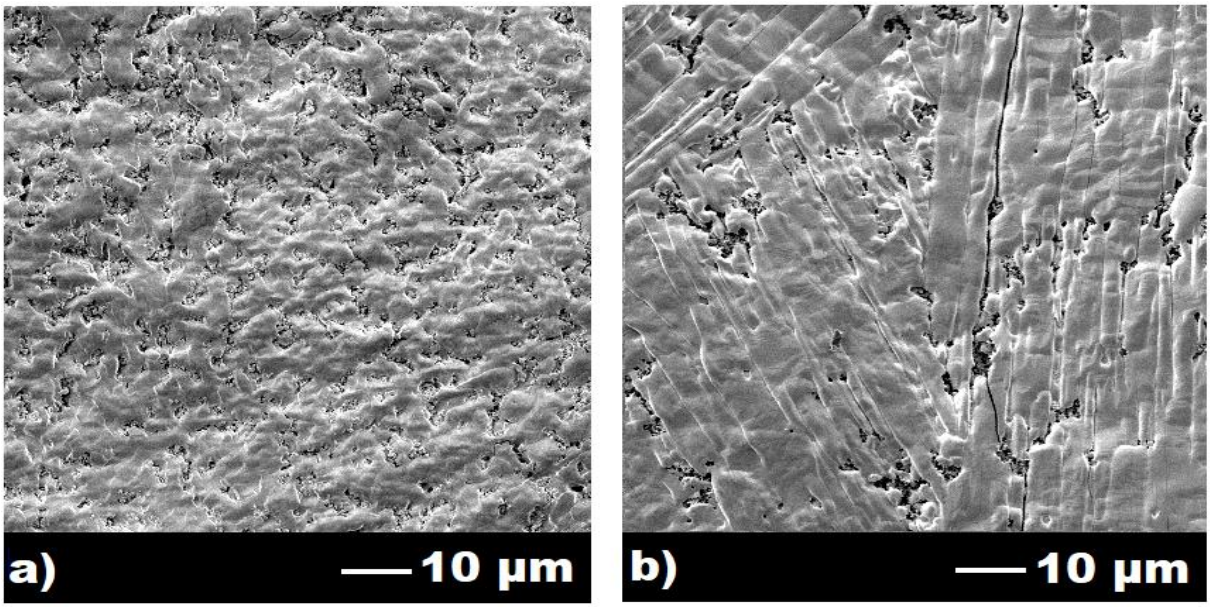

Figure 5.9 SEM images of a 30SDC-70SSC dual-phase OTMs surface after exposure to a CO_2 sweeping gas with a flow rate of 80 ml.min^{-1} while held at a membrane temperature of 900°C for 50 (a) and 60 (b) hours

5.4 Oxygen permeation flux under modified CO_2 sweeping gas flow rates and membrane temperatures

Chapter 4 demonstrated the effects of membrane temperature and sweeping gas flow rate on an OTM's oxygen permeation flux. It was shown that as the membrane temperature increased, while exposed to a constant sweeping gas flow rate, the oxygen permeation flux increased due to the enhancement of oxygen diffusivity throughout the membrane. Furthermore, as the sweeping gas flow rate increased, while held at a constant membrane temperature, the oxygen permeation flux increased due to the higher sweeping gas flow rate improving the oxygen chemical gradient across the OTM. In this chapter, after determining the effect of dual-phase compositions on the oxygen permeation flux in CO_2 atmospheres, additional long-term studies were administered for 50 hours. These long-term oxygen permeation tests were conducted by modifying the membrane temperature to either 800°C, 850°C, or 900°C and CO_2 sweeping gas flow rate to 20 $ml.min^{-1}$, 40 $ml.min^{-1}$, or 80 $ml.min^{-1}$ on the permeation side of a 30SDC-70SSC dual-phase OTM.

Figure 5.10 shows the oxygen permeation flux of a 30SDC-70SSC dual-phase OTM at varying membrane temperatures while exposed to a pure CO_2 sweeping gas flow rate of 20 $ml.min^{-1}$ (Fig. 5.10a), 40 $ml.min^{-1}$ (Fig. 5.10b), and 80 $ml.min^{-1}$ (Fig. 5.10c) for 50 hours. In each sub-figure of Fig. 5.10, the oxygen permeation flux is observed to increase with an increase in membrane temperature. For example, at a constant CO_2 sweeping gas flow rate of 80 $ml.min^{-1}$ the highest and lowest oxygen permeation fluxes were found to be 0.30 $ml.min^{-1}.cm^{-2}$ and 0.73 $ml.min^{-1}.cm^{-2}$ at a membrane temperature of 800°C and 900°C, respectively.

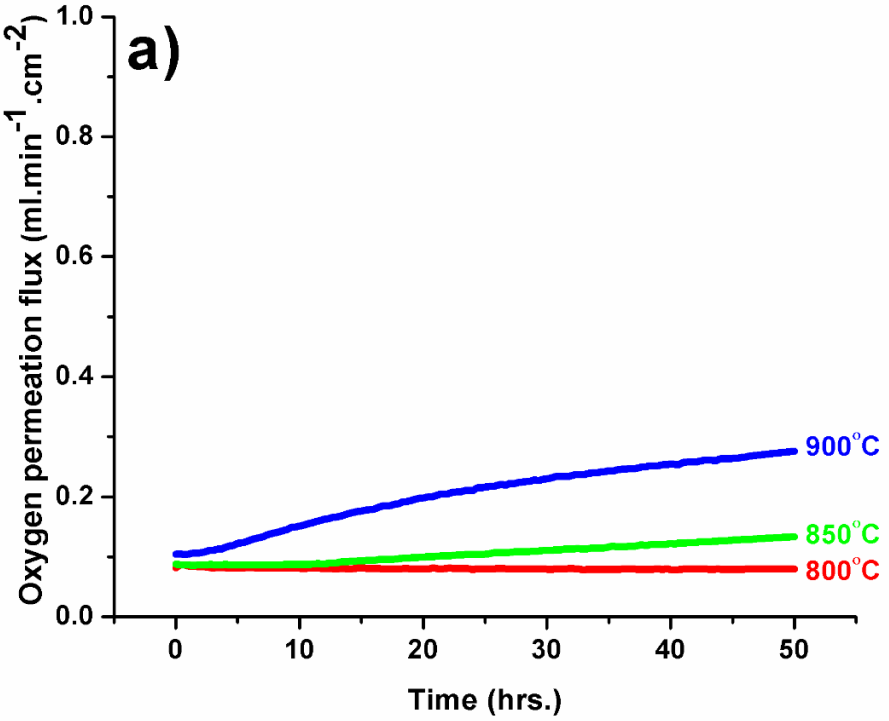
a)
Oxygen permeation flux (ml.min-1.cm-2)
1.0
0.8
0.6
0.4
0.2
0.0
0
10
20
30
40
50
Time (hrs.)
900°C
850°C
800°C

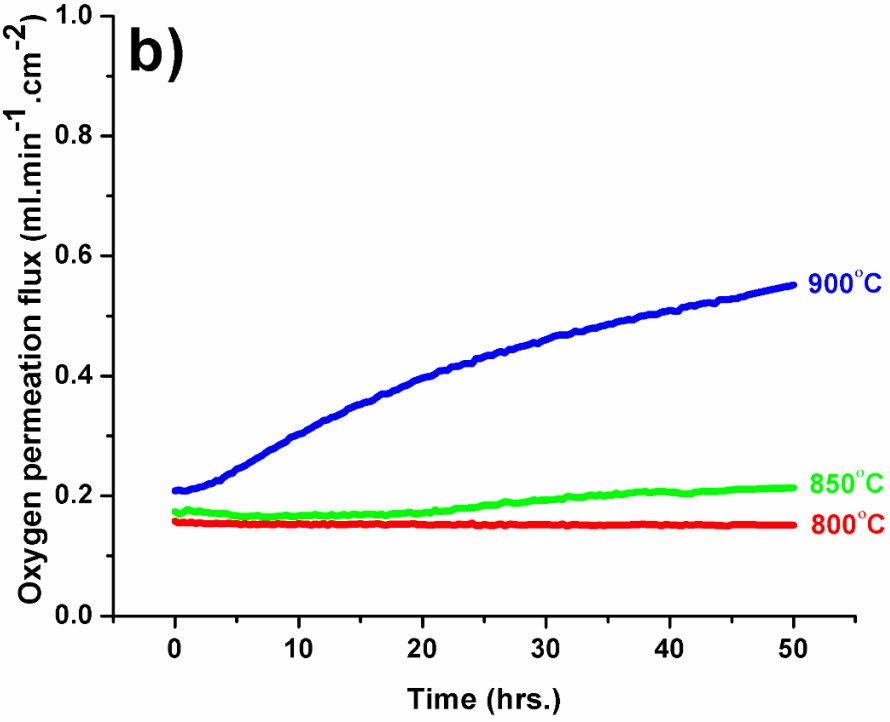
b)
Oxygen permeation flux (ml.min-1.cm-2)
1.0
0.8
0.6
0.4
0.2
0.0
0
10
20
30
40
50
Time (hrs.)
900°C
850°C
800°C

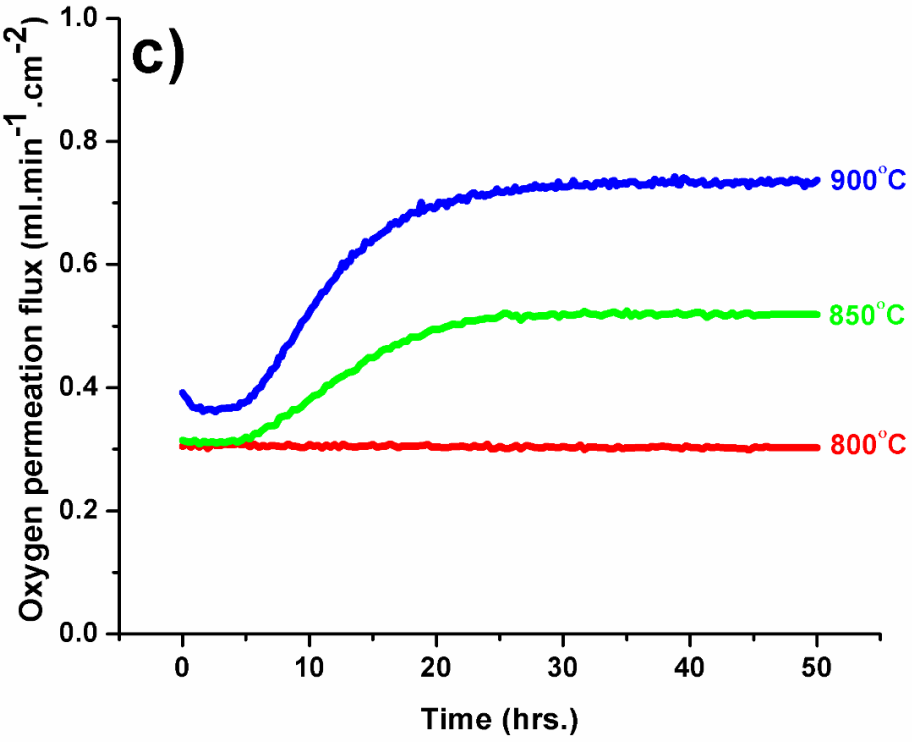

Figure 5.10 Unsteady oxygen permeation flux of a 30SDC-70SSC dual-phase OTM while subjected to a CO_2 sweeping gas with a flow rate of 20 (a), 40 (b), or 80 (c) $ml.min^{-1}$ while held at a membrane temperature of 800°C, 850°C, or 900°C for 50 hours

The 30SDC-70SSC dual-phase OTM held at a membrane temperature of 800°C demonstrates at steady oxygen permeation flux for entire permeation test when exposed to a CO_2 sweeping gas flow rate of 20 $ml.min^{-1}$, 40 $ml.min^{-1}$, and 80 $ml.min^{-1}$. The steady oxygen permeation flux of the 30SDC-70SSC dual-phase OTM is a result of the maintained internal structure of the membrane. Figure 5.11 displays the surface and cross-section of a 30SDC-70SSC dual-phase OTM after an oxygen permeation test at a CO_2 sweeping gas flow rate of 80 $ml.min^{-1}$ while held at a membrane temperature of 800°C for 50 hours. The surface of the dual-phase 30SDC-70SSC dual-phase OTM after the permeation test is observed to exhibit minor carbonate formations that have grown on the membrane surface. The cross-section, however, is observed to have remained intact, signifying an uncompromised internal membrane structure which resulted in the steady oxygen permeation fluxes displayed in Fig. 5.10.

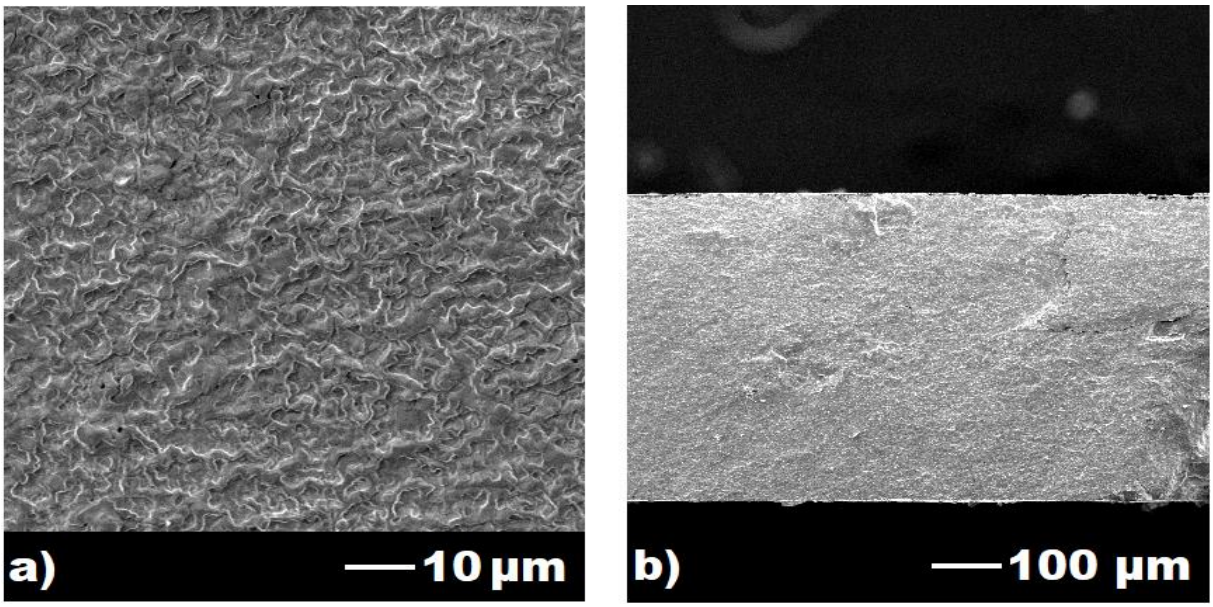

Figure 5.11 SEM images of a 30SDC-70SSC dual-phase OTMs surface and cross-section after exposure to a CO_2 sweeping gas with a flow rate of 80 ml.min^{-1} while held at a membrane temperature of 800°C for 50 hours

A difference in the carbonate formation is observed when comparing the cross sections of the 30SDC-70SSC dual-phase OTMs subjected to a CO_2 sweeping gas flow rate of 80 ml.min^{-1} while held at a membrane temperature of 800°C (Fig 5.11b) or 900°C (Fig 5.9a) for 50 hours. The difference in the membrane morphology suggests that the carbonate formation grows at a faster rate at higher membrane temperatures. The relation between the carbonate formation and membrane temperature can further be seen when examining Table 5.2. Table 5.2 shows the rate of change in the rise region of the oxygen permeation flux of a 30SDC-70SSC dual-phase OTM while subjected to a CO_2 sweeping gas with a flow rate of 20, 40, or 80 ml.min^{-1} while held at a membrane temperature of 800°C, 850°C, or 900°C for 50 hours.

Table 5.2 demonstrates that the rate of change in the oxygen permeation flux over time increases as the membrane temperature also increases. For example, at a CO_2 sweeping gas flow rate of 40 ml.min^{-1}, the oxygen permeation flux increases of a rate of 1.3E-3 [ml.min^{-1}.cm^{-2}].hr^{-1} at a membrane temperature of 850°C, which is a third of the rate at which the oxygen permeation

flux increases at a membrane temperature of 900°C (6.9E-3 [ml.min^{-1}.cm^{-2}].hr^{-1}). The increase in the oxygen permeation flux over time is a result of the carbonate formation on the membrane surface, which reduces the uncompromised membrane thickness, thus improving the oxygen permeation flux.

Table 5.2 also shows a faster rate of change in the oxygen permeation flux as the CO_2 sweeping gas flow rate increases. For example, at a constant membrane temperature of 900°C, the rate of change in the oxygen permeation flux within the rise region was observed to 3.4E-3, 6.9E-3, and 1.1E-2 [ml.min^{-1}.cm^{-2}].hr^{-1} at a CO_2 sweeping gas flow rate of 20, 40, and 80 ml.min^{-1}, respectively. The difference in the rate of change of the oxygen permeation flux within the rise region is a result of the growth of the carbonate formation of the permeation surface.

Table 5.2 The rate of change in the oxygen permeation flux of a 30SDC-70SSC dual-phase OTM while subjected to a CO_2 sweeping gas with a flow rate of 20, 40, or 80 ml.min^{-1} while held at a membrane temperature of 800°C, 850°C, or 900°C within the rise region

Membrane temperature (°C)	**CO_2 sweeping gas flow rate (ml.min^{-1})**	$\frac{dJ_{O_2}}{dt}$
800	20	0
	40	0
	80	0
850	20	9.2E-4
	40	1.3E-3
	80	6.6E-3
900	20	3.4E-3
	40	6.9E-3
	80	1.1E-2

Figure 5.12 shows the surface and cross-section of the 30SDC-70SSC dual-phase OTM exposed to a sweeping gas flow rate of 20 ml.min^{-1} while held at a membrane temperature of 900°C

for 50 hours. In comparison to the cross-section (Fig. 5.8a) and surface (Fig.5.9a) of the 30SDC-70SSC dual-phase OTM exposed to a sweeping gas flow rate of 80 ml.min^{-1} while held at 900°C for 50 hours, the cross-section and surfaces shown in Fig. 5.12 are observed to have limited regions on the permeation surface of which the carbonate formation occurs. The difference between the carbonate formation found in the cross-section images of the 30SDC-70SSC dual-phase OTM when subjected to a CO_2 sweeping gas flow rate of 20 ml.min^{-1} and 80 ml.min^{-1} is attributed to the larger volume of CO_2 introduced to the permeation surface during the 50-hour experiment. The larger volume of CO_2 exposed to the permeation surface of the dual-phase OTM enhances the growth rate of the carbonate formation, thus reducing the internal cross-section and improving the oxygen permeation flux as observed in Fig 5.10c.

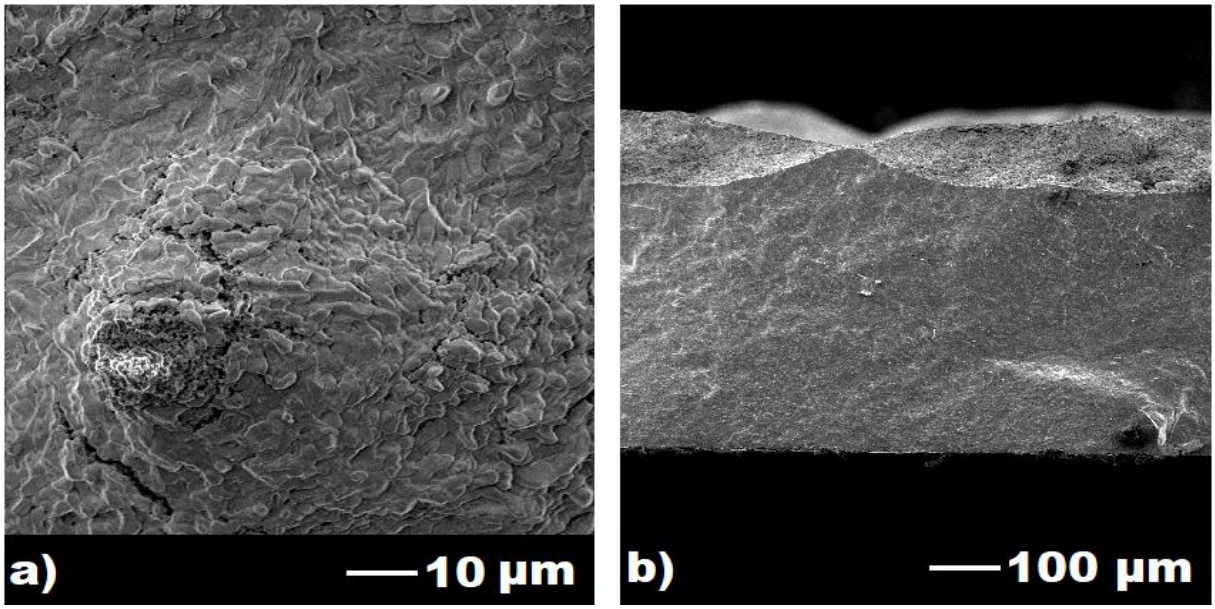

Figure 5.12 SEM images of a 30SDC-70SSC dual-phase OTMs surface and cross-section after exposure to a CO_2 sweeping gas with a flow rate of 20 ml.min^{-1} while held at a membrane temperature of 900°C for 50 hours

5.5 Conclusion

The work presented in this chapter studies the behavior of dual-phase OTMs in CO_2 atmospheres. The oxygen permeation flux and structure of dual-phase OTMs with varying

compositions ranging from 0 to 50 wt.% SDC on increments of 10 wt.% SDC were investigated using a CO_2 sweeping gas with a flow rate of 80 $ml.min^{-1}$ and membrane temperature of 900°C for 60 hours. A pure SSC OTM was found to have degraded entirely in structure and performance after exposure to CO_2 for 60 hours due to the formation of $SrCO_3$ throughout the membrane structure. Other dual-phase compositions exhibiting a higher wt.% SDC within their composition was found to reduce the carbonate formation rate throughout the membrane as observed by the gradual increase in the oxygen permeation flux about the CO_2 exposure time. At higher wt.% of SDC (>20 wt.%), the carbonate formation was found to subside leaving a consistent uncompromised membrane thickness that resulted in a steady oxygen permeation flux. The 30SDC-70SSC dual-phase OTM was found to exhibit the highest oxygen permeation flux (0.73 $ml.min^{-1}.cm^{-2}$) compared to other dual-phase OTMs when subjected to a CO_2 sweeping gas with a flow rate of 80 $ml.min^{-1}$ while held at a membrane temperature of 900°C.

The oxygen permeation flux using a CO_2 sweeping gas was also investigated through varying other vital factors such as membrane temperature and sweeping gas flow rate. The oxygen permeation flux was discovered to gradually increase slower at lower membrane temperatures and sweeping gas flow rate, suggesting that the carbonate growth rate on the membrane's permeation surface was enhanced by higher membrane temperatures and larger volumes of CO_2 swept across the OTM. Although most investigated conditions displayed some interaction between the SSC material and CO_2 sweeping gas, this chapter identified key factors that can improve the oxygen permeation flux and structure in rich CO_2 atmospheres.

Chapter 6 Exploring the performance of dual-phase oxygen transport membranes for carbon capture purposes

6.1 Introduction

There is a rising pressure on industry to meet the steady climb of energy demand while concurrently reducing harmful emissions exhausted into the atmosphere. For the past decade, oxygen transport membrane reactors (OTMs), have been receiving growing attention due to their ability to provide high volumes of pure oxygen that react with incoming fuel at minimal energy costs. However, one significant concern is the OTM's stability when exposed to high concentrations of CO_2, a potentially harmful acidic gas. To preserve the integrity of the OTM in acidic environments, many have adapted dual-phase OTMs, combining the advantages of the perovskite-type material's high oxygen permeation performance with a stable additive material's tolerance of CO_2.

As discussed in Chapter 2 and 5, dual-phase OTMs are comprised of two materials with different atomic structures, ionic and electronic conductive properties and resistances towards destructive gases. As demonstrated in Chapter 5, an SDC/SSC dual-phase OTM was fabricated to combine a mixed ionic and electronic conductive perovskite-type material with an exclusively ionic conductive material. The produced SDC/SSC dual-phase OTM was shown to transport oxygen ions through the OTM after exposure to a CO_2 atmosphere due to the preservation of the B-site ions within the perovskite-type structure exhibiting some electronic conductivity after the SSC phase transformation while the presence of SDC maintained ion transport pathways. The results shown in Chapter 5 suggest a possible composition that could be used to produce OTMs for the application of oxy-fuel combustion.

Although improving upon the performance and stability in CO_2 environments found downstream for the application of oxy-fuel combustion, dual-phase OTMs present the potential challenge of maintaining a high oxygen permeation flux (>1 $ml.min^{-1}.cm^{-2}$) in unconverted fuel rich atmospheres found upstream. An exclusively mixed ionic-electronic conductive OTM can reduce surrounding oxygen anywhere on the feed side surface and re-oxidize anywhere on the permeation side surface. However, the addition of an exclusively ionic conductive material (SDC) limits the number of reducing and re-oxidizing sites due to the reduced number of electronic pathways throughout the entire structure. This chapter aims to examine dual-phase OTM's oxygen permeation performances, with different OTM compositions while using different sweeping gases such as helium, methane, and CO_2.

6.2 Experimental methods

$SrSc_{0.1}Co_{0.9}O_{3-\delta}$ (SSC) was selected as the perovskite-type material due to previous chapters and previous research demonstrating a higher oxygen permeation performance and electronic conductivity compared to more popular materials such as $La_{0.6}Sr_{0.4}Co_{0.2}Fe_{0.8}O_{3-\delta}$ and $Ba_{0.5}Sr_{0.5}Co_{0.8}Fe_{0.2}O_{3-\delta}$ [131,174]. SDC was also selected as the additional material for the dual-phase OTM due to its high ionic conductivity and its resistivity to CO_2 atmospheres [47,48,113,175]. The SDC/SSC dual-phase planar OTMs were fabricated using the method described in Chapter 5. Phase structure of the material was determined using X-ray diffraction (XRD) while morphologies were observed using a scanning electron microscope (SEM). Relative density was calculated using Archimedes' method in distilled water [176,177]. The total conductivity of bar samples with dual-phase compositions ranging from 0 to 50 wt.% SDC was measured using the same four-probe method set-up as described in Chapter 3. Bar samples with varying weight ratios of SDC were mixed and fabricated using the techniques described in

Chapters 3 and 5. The total conductivity of each bar sample was measured in air with an increase in temperature ranging from 300°C to 900°C at a rate of 1°C/min.

The oxygen permeation flux of the dual-phase planar membranes was investigated using the experimental set-up shown in Fig. 6.1. The oxygen permeation flux was determined using the same experimental approach as described in Chapter 4 and 5 with the additional use of a helium sweeping gas. The oxygen permeation flux was calculated using Eq. 5.1 when using a helium sweeping gas and Eq. 4.8 when using a methane sweeping gas. Additionally, CO_2 selectivity was calculated using Eq.4.9.

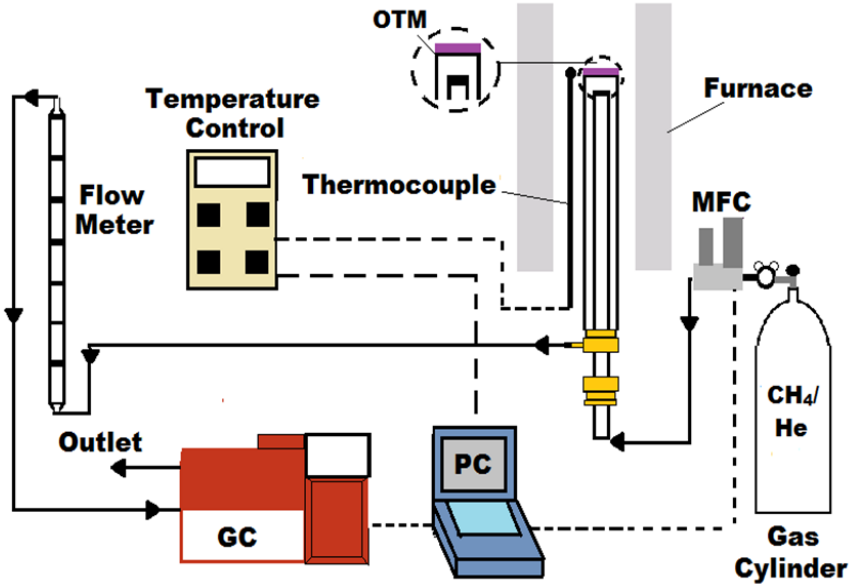

Figure 6.1 Experimental setup for oxygen permeation measurements with a methane or helium sweeping gas

6.3 Results and discussion

6.3.1 Structures of dual-phase OTMs

Figure 6.2 shows the XRD patterns of the sintered OTMs. All composite OTMs scans contain a fluorite-type (SDC) and perovskite-type (SSC) phase, showing no signs of any impurities. When compared to the pure SDC and SSC line scans, there is no interaction within the dual-phase composition during the sintering process. Therefore, both phases demonstrate chemical

compatibility for all composition ratios, regardless of additional SDC additive. This can be observed as the addition of SDC material to the OTM composition weakens the SSC peaks at 32.6°, 40.05°, 46.65°, 58.05°, 68.40° and 77.80°, which corresponds to the diminishing portion of SSC material in the OTM composition. This was further verified when examining the OTM morphology using the SEM.

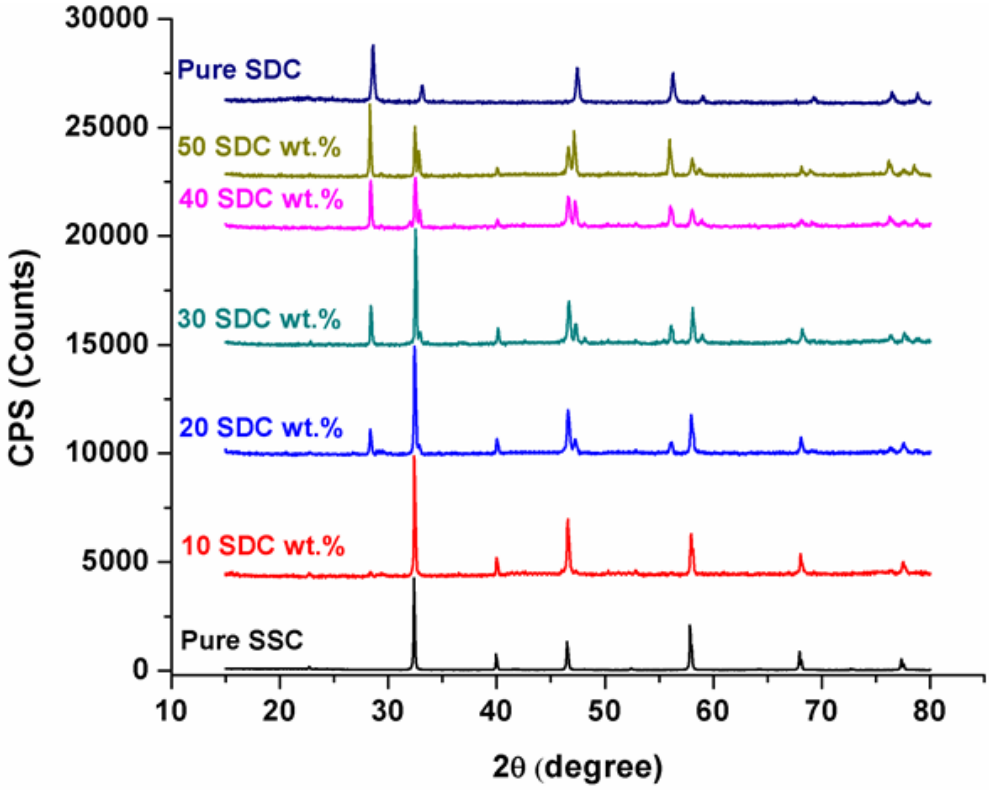

Figure 6.2 XRD patterns of SSC-SDC dual-phase OTMs with different weight ratios after sintering at 1200°C for 5 hours

The total conductivity of the single-phase perovskite and dual-phase composite oxides are shown in Fig. 6.3. The perovskite oxides have a higher total conductivity compared to the dual-phase composite oxides. As discussed in Chapter 5, the initial rise in the total conductivity attributes to the perovskite-type material's p-type semi-conductivity, of which there is a transition at high temperature due to the reduction of Co^{+4} to Co^{+3} or Sc^{+3} to Sc^{+2} [168,169]. The total conductivity of the dual-phase composite materials is much lower than the total conductivities of

the perovskite-type materials, since the fluorite phase oxide (SDC), is an exclusively ionic conductor and limits the electron mobility through the entire sample. Previous studies have shown similar trends when comparing the total conductivity of single and dual-phase compositions [114,178,179].

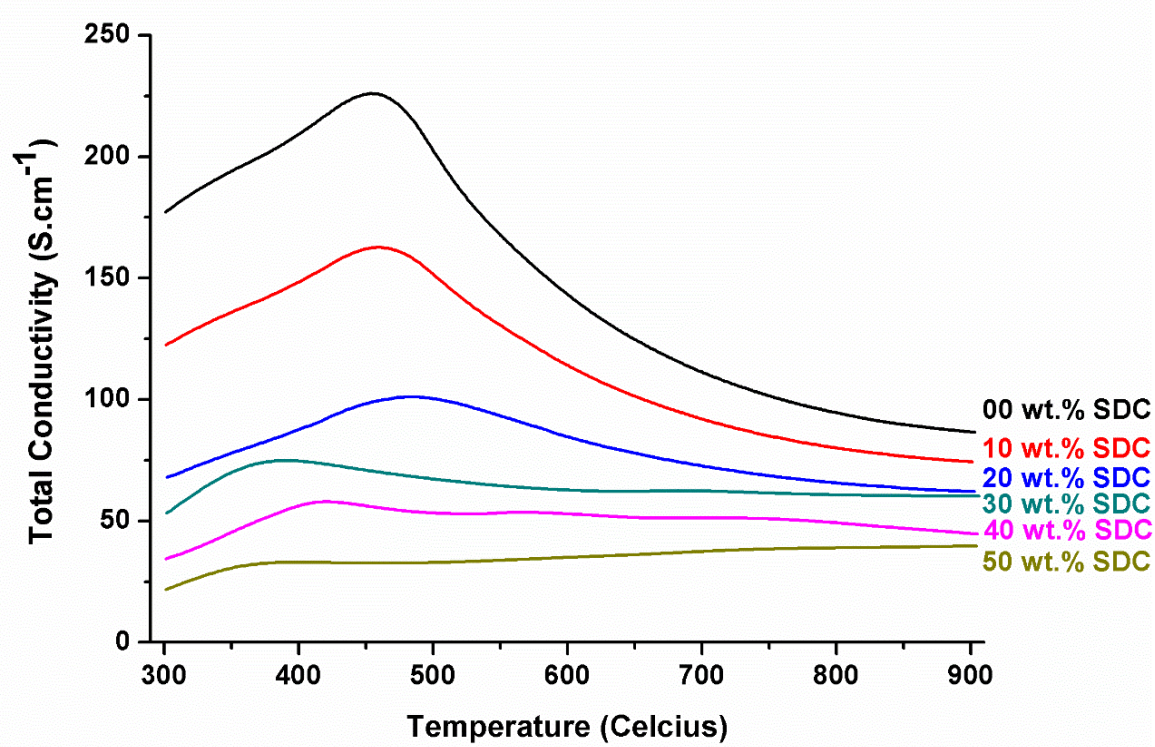

Figure 6.3 Total conductivity with respect to temperature of SDC-SSC dual-phase compositions varying from 0 to 50 wt.% SDC

The SEM images of the OTMs' surface area shown in Fig. 6.4, arranged in incremental order (a-f) of SDC additive (0-50 SDC wt.%). These images indicate that all composite OTMs were able to successfully achieve a high relative dense structure with some negligible areas of small pores. This relative density is further reported in Table. 6.1, showing an increase in the addition of SDC. The improvement in the relative density is primarily contributed to the difference in sintering temperature of the different materials. Typically, the sintering temperature for SSC is between 1100°C and 1200°C while SDC requires up to 1600°C to achieve a similar densification [45,180]. Because the dual-phase OTMs were sintered at 1200°C, the SSC material was able to densify while

the SDC additive was able to fill in any unoccupied gaps during the sintering process, thus improving the relative density of the overall OTM. Furthermore, the addition of SDC provided a more heterogeneous mixture, creating a division between SSC grains and promoting the reduction of SSC grain size. This can be particularly seen in Fig. 6.4a and Fig. 6.4e which show a decline SSC grain size with the addition of SDC material.

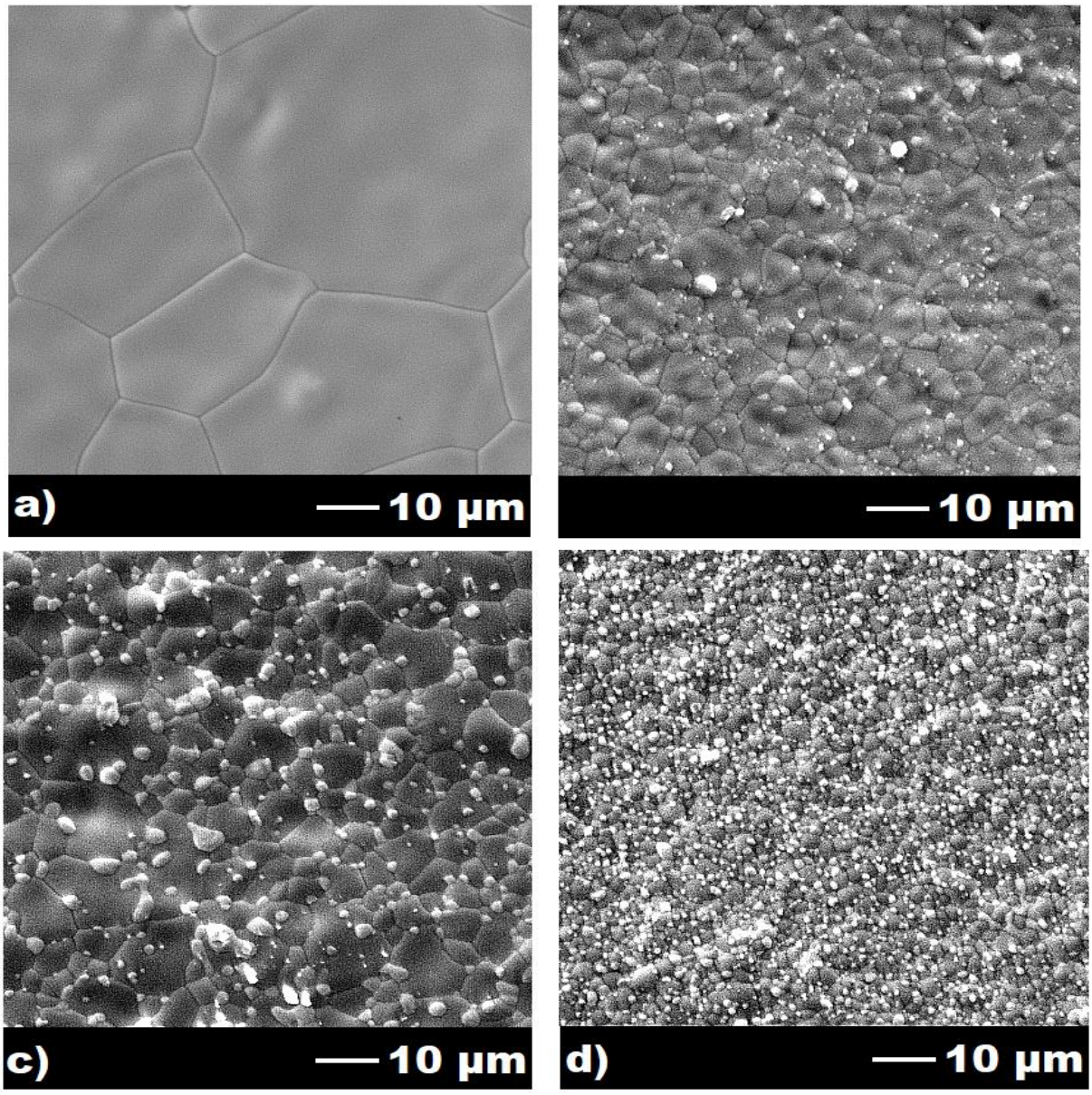

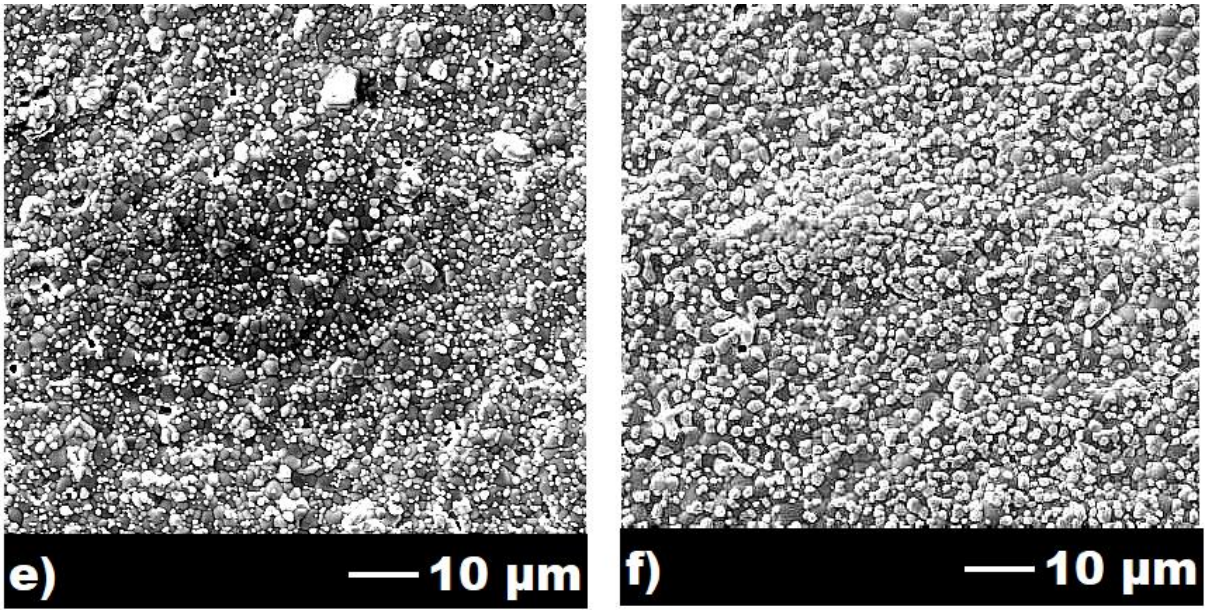

Figure 6.4 SEM images of the dual-phase OTM surfaces arranged in incremental order (a-f) of SDC additive (0-50 wt.%) after sintering for 5 hours at 1200°C

Table 6.1 Microstructural characteristics of SSC-SDC dual-phase OTM

SSC weight fraction	SDC weight fraction	SSC volume fraction	SDC volume fraction	% of relative density
1	0	1	0	90
0.9	0.1	0.92	0.08	90
0.8	0.2	0.84	0.16	91
0.7	0.3	0.76	0.24	92
0.6	0.4	0.66	0.34	94
0.5	0.5	0.57	0.43	96

6.3.2 Oxygen permeation performance of dual-phase OTMs with a helium sweeping gas

6.3.2.1 Temperature dependence of oxygen permeation flux

The oxygen permeation performance of the dual-phase SDC-SSC OTM was measured at a temperature range of 750 to 900°C with a helium sweeping gas flow rate of 100 $ml.min^{-1}$. All oxygen permeation data was collected after reaching steady state. As shown in Fig. 6.5, the oxygen permeation flux for all OTMs, regardless of composition, increases with temperature. The increase in the oxygen permeation flux relates to the improvement of the surface exchange properties of the

OTM as previously shown in Fig. 3.8. Due to the enhanced surface exchange coefficient with an increase in temperature, the membranes ability to reduce and re-oxidize oxygen on the feed and permeation sides, respectively, improves, thus enhancing the oxygen permeation flux. The pure SSC OTM exhibits the highest oxygen permeation flux, ranging from 0.78 $ml.min^{-1}.cm^{-2}$ and 2.11 $ml.min^{-1}.cm^{-2}$ at 750°C and 900°C. The pure SSC OTM was able to achieve the highest flux due to its ability to react with the surrounding oxygen on the entire feed side surface. As more SDC is introduced into the OTM composition, there are less available sites on the feed side for the perovskite-type material to reduce the surrounding oxygen, therefore diminishing the oxygen permeation flux. This trend is further seen with the increase in the wt.% of SDC. Specifically, the lowest and highest values of a 10 SDC wt.% OTM is 0.56 $ml.min^{-1}.cm^{-2}$ and 1.30 $ml.min^{-1}.cm^{-2}$ at 750°C and 900°C, while a 50 SDC wt.% OTM has a low and high value of 0.32 $ml.min^{-1}.cm^{-2}$ and 1.00 $ml.min^{-1}.cm^{-2}$ at the same temperatures.

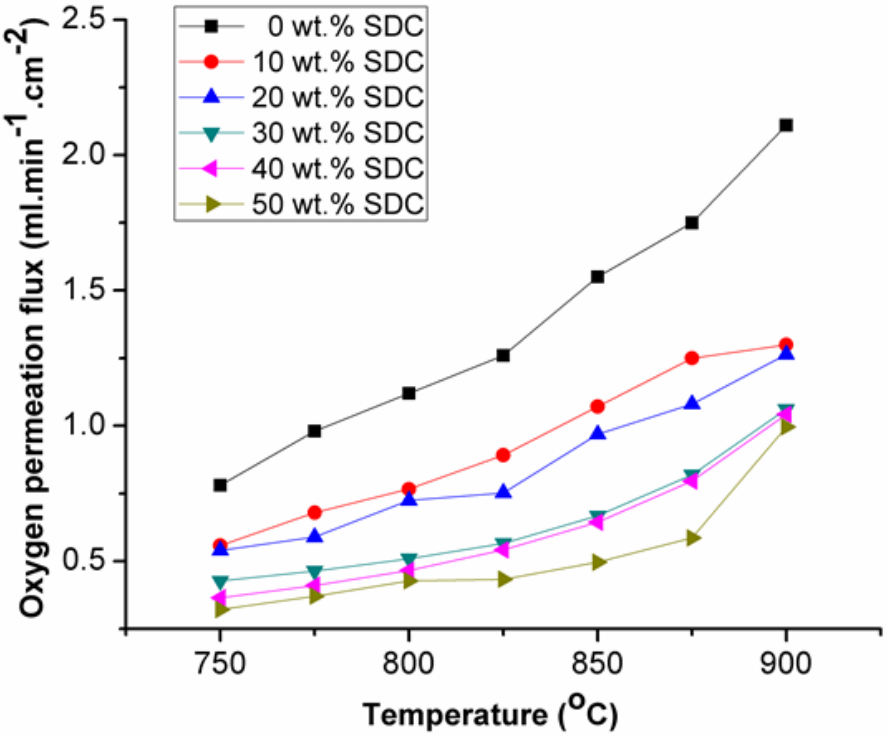

Figure 6.5 Temperature dependence of oxygen permeation fluxes through the SDC-SSC dual-phase membrane and SSC membrane with a helium sweeping gas flow rate of 100 $ml.min^{-1}$

6.3.2.2 Sweeping gas flow dependence of oxygen permeation flux

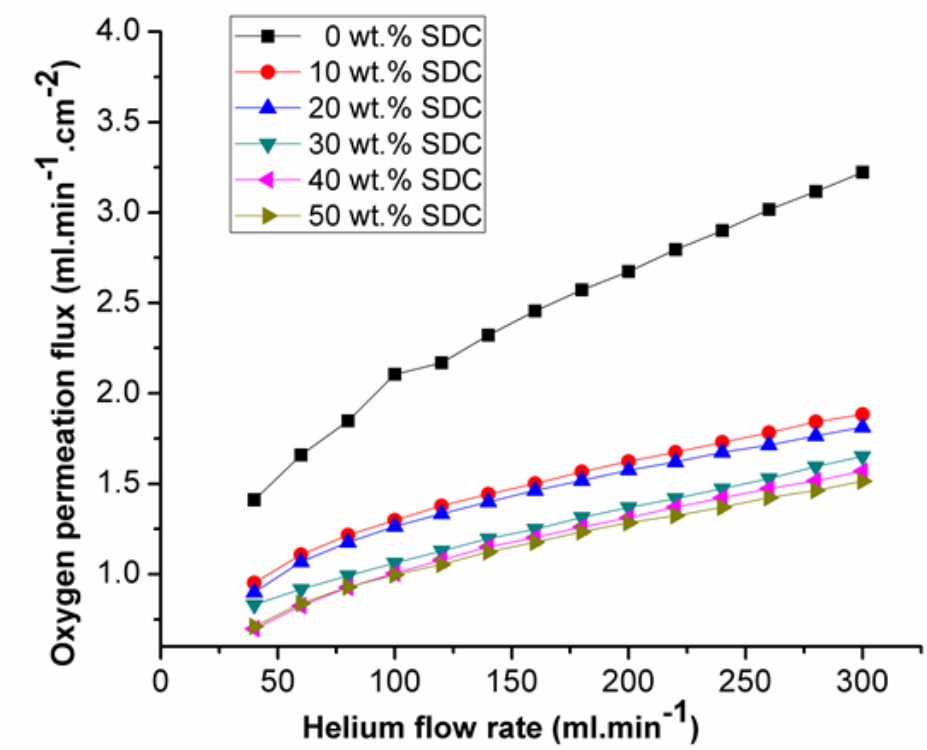

Figure 6.6 Effects of helium sweeping gas flow rates on oxygen permeation fluxes through the SDC-SSC dual-phase membrane and SSC membrane at 900°C

The oxygen permeation performance of the dual-phase SDC-SSC OTM was also measured at a helium flow rate ranging from 40 ml.min^{-1} to 300 ml.min^{-1} at 900°C. Figure 6.6 shows the direct relationship between the incoming sweeping gas flow rate and oxygen permeation flux for all OTM compositions. The oxygen permeation fluxes' dependency on sweeping gas flow rate is a result of the surface exchange properties of the OTM. The pure SSC OTM has the highest oxygen permeation flux for all flow rates ranging from 1.41 ml.min^{-1}.cm^{-2} at 40 ml.min^{-1} and 3.22 ml.min^{-1}.cm^{-2} at 300 ml.min^{-1}, respectively. As the wt.% of SDC increases, however, the oxygen permeation flux decreases. The OTM with a dual-phase composition of 50 SDC wt.% is only able to achieve an oxygen permeation flux of 0.51 ml.min^{-1}.cm^{-2} and 1.51 ml.min^{-1}.cm^{-2} at 40 ml.min^{-1} and 300 ml.min^{-1}, respectively. When the composition of SDC increases, the surface exchange properties are modified, diminishing the exchange rate of oxygen on both sides of the OTM. That

is, the growing presence of SDC on the OTM surfaces reduces the potential for the surrounding oxygen on the feed side as well as re-oxidizes on the permeation side, ultimately reducing the oxygen permeation flux.

6.3.2.3 Sweeping gas composition dependence of oxygen permeation flux

After examining the oxygen permeation flux with helium, methane was used to investigate the dual-phase oxygen permeation and combustion performance using a reactive sweeping gas. The methane flow rate ranged from 40 to 80 $ml.min^{-1}$ with a membrane temperature of 900°C. As previously stated, using a methane sweeping gas, the components detected in the GC were oxygen, CO_2, CO, C_2H_6, and methane (unreacted). To distinguish the difference in performance between methane and helium sweeping gases, the oxygen permeation fluxes were compared at the same flow rates and presented in Fig. 6.7. In comparison, the oxygen permeation flux is higher when using methane as opposed to helium; A pure SSC OTM exhibits a higher oxygen permeation flux of 5.27 $ml.min^{-1}.cm^{-2}$ at 80 $ml.min^{-1}$ compared to the 1.84 $ml.min^{-1}.cm^{-2}$ found using helium at the same flow rate. The performance variation is attributed to the methane sweeping gas' ability to react with the permeated oxygen compared to the inert sweeping gas. When using methane as a sweeping gas, the concentration of oxygen on the permeation side is maintained at a much lower value compared to using helium sweeping gas. The difference is oxygen concentration on the permeation sides signifies a higher oxygen chemical gradient for a methane sweeping gas across the dual-phase OTM, ultimately producing a greater oxygen permeation performance overall.

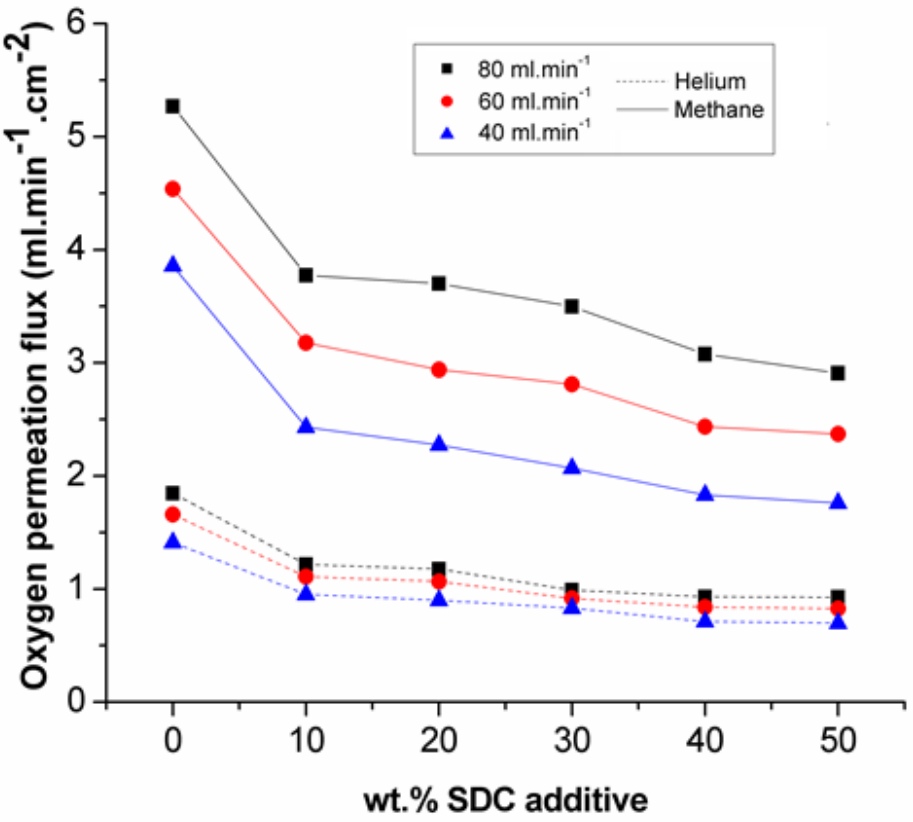

Figure 6.7 Sweeping gas comparison of oxygen permeation fluxes between helium and methane for the SDC-SSC dual-phase membranes and SSC membrane at 900°C

Despite the performance discrepancy between methane and helium sweeping gases, the oxygen permeation flux still decreases as the SDC wt.% increases, regardless of sweeping gas. At a flow rate of 80 $ml.min^{-1}$, the difference in the oxygen permeation flux between a pure SSC OTM and a dual-phase OTM 50 SDC wt.% for a methane sweeping gas is 2.91 $ml.min^{-1}.cm^{-2}$, while 0.92 $ml.min^{-1}.cm^{-2}$ for a helium sweeping gas. The steeper decline in the oxygen permeation flux is a result of the interaction between the sweeping gas and the OTM, specifically the perovskite-type material. Due to the methane sweeping gas' ability to react with permeated oxygen, the addition of SDC on the membrane surface reduces the number of permeation sites, thus limiting the reaction between methane and permeated oxygen.

6.3.3 Oxygen permeation and combustion performance with methane

6.3.3.1 Sweeping gas flow dependence of oxygen permeation flux

The oxygen permeation flux using a methane sweeping gas was further investigated by extending the minimum flow rate to 5 $ml.min^{-1}$. As shown in Fig. 6.8 the oxygen permeation flux increases with an increase in methane flow rate while decreasing with additional SDC wt.% within the OTM composition. A pure SSC OTM is shown to have the highest oxygen permeation flux for all flow rates with a maximum flux of 5.27 $ml.min^{-1}.cm^{-2}$ using a methane flow rate of 80 $ml.min^{-1}$. A 50 SDC wt.% is found to have the lowest oxygen permeation flux with a minimum flow rate of 0.71 $ml.min^{-1}.cm^{-2}$ using a methane flow rate of 5 $ml.min^{-1}$. Despite the decline in the oxygen permeation flux with the addition of SDC in the dual-phase membrane composition, for most of the results presented in Fig. 6.8, the oxygen permeation flux is still observed to be high (>1 $ml.min^{-1}.cm^{-2}$), signifying a superior oxygen permeability to most developed materials.

Additionally, the difference in the oxygen permeation flux within the range of SDC wt.% is shown to vary less as the flow rate decreases. Specifically, between a pure SSC OTM and a dual-phase OTM 50 SDC wt.%, the oxygen permeation flux decreases by 1.29 $ml.min^{-1}.cm^{-2}$ at a flow rate of 5 $ml.min^{-1}$, but decreases 2.37 $ml.min^{-1}.cm^{-2}$ at a flow rate of 80 $ml.min^{-1}$. The smaller variance in the oxygen permeation flux at low sweeping gas flow rates indicates that the dual-phase composition has less of an impact on the oxygen permeability as the sweeping gas flow rate decreases. However, the oxygen permeation flux is not completely independent of the OTM composition since the oxygen permeation flux still decreases as SDC wt.% increases at the lowest flow rate of 5 $ml.min^{-1}$.

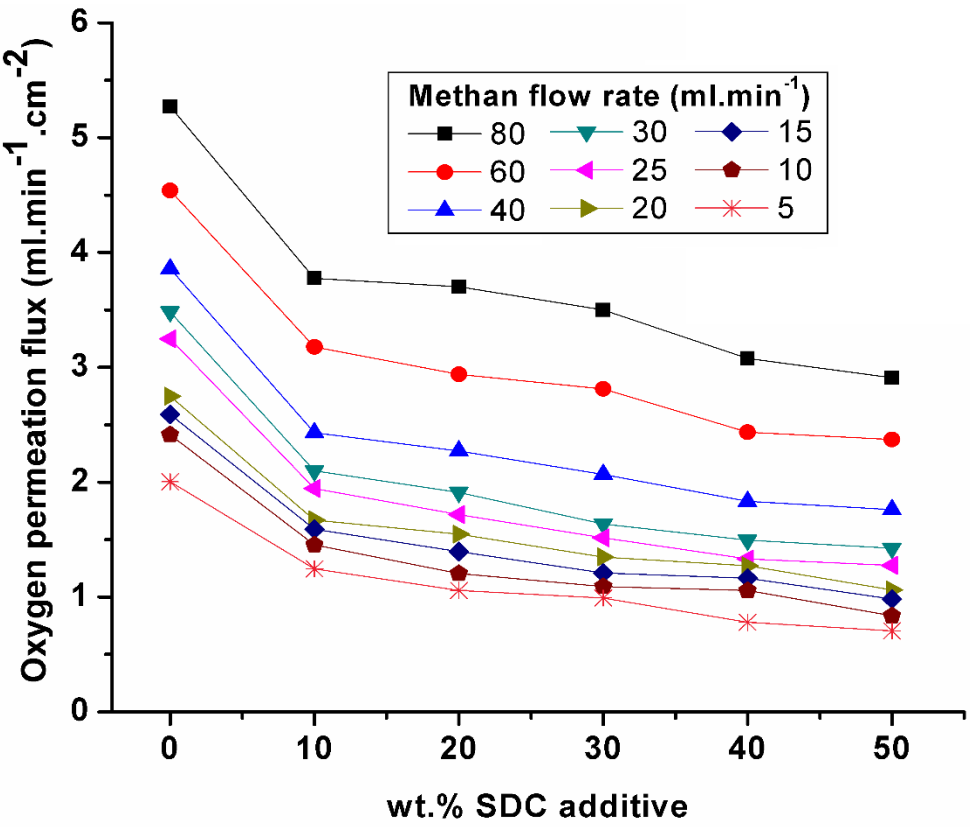

Figure 6.8 Methane sweeping gas flow rates influence on oxygen permeation fluxes through the SDC-SSC dual-phase membrane and SSC membrane at 900°C

6.3.3.2 Sweeping gas flow dependence of CO_2 selectivity

In addition to the oxygen permeation flux, the CO_2 selectivity was calculated using Eq. 4.9 and compared under varying flow rates and OTM compositions. It was found that a pure SSC OTM exhibits the highest CO_2 selectivity of 97.7% at a methane flow rate of 5 $ml.min^{-1}$. Although the oxygen permeation flux increases with an increase in methane flow rate, the CO_2 selectivity decreases, primarily caused by the volume of permeated oxygen relative to the volumetric flow rate of methane. As the methane flow rate increases, the surface exchange is enhanced, ultimately increasing the oxygen permeation flux. However, the increase in methane flow rate is not proportional to the permeated oxygen. This imbalance causes an oxygen-depleted reaction that decreases the concentration of CO_2 in the product stream. As the flow rate is lowered, the ratio between the permeated oxygen and incoming methane becomes more balanced, thus producing a

richer CO_2 concentration. Moreover, the addition of SDC within the OTM composition has a similar effect on the CO_2 selectivity. As shown in previous figures, the oxygen permeation flux decreases with an increase in SDC wt.% caused by the modified permeability properties of the dual-phase OTM. Thus, the further lack of permeated oxygen diminishes methane combustion and reduces the concentration of CO_2 within the exhaust stream. Furthermore, at methane flow rates lower than 20 $ml.min^{-1}$, the CO_2 selectivity is greater than 80% for all investigated dual-phase membrane compositions, indicating the potential to be used for the application of oxy-fuel combustion.

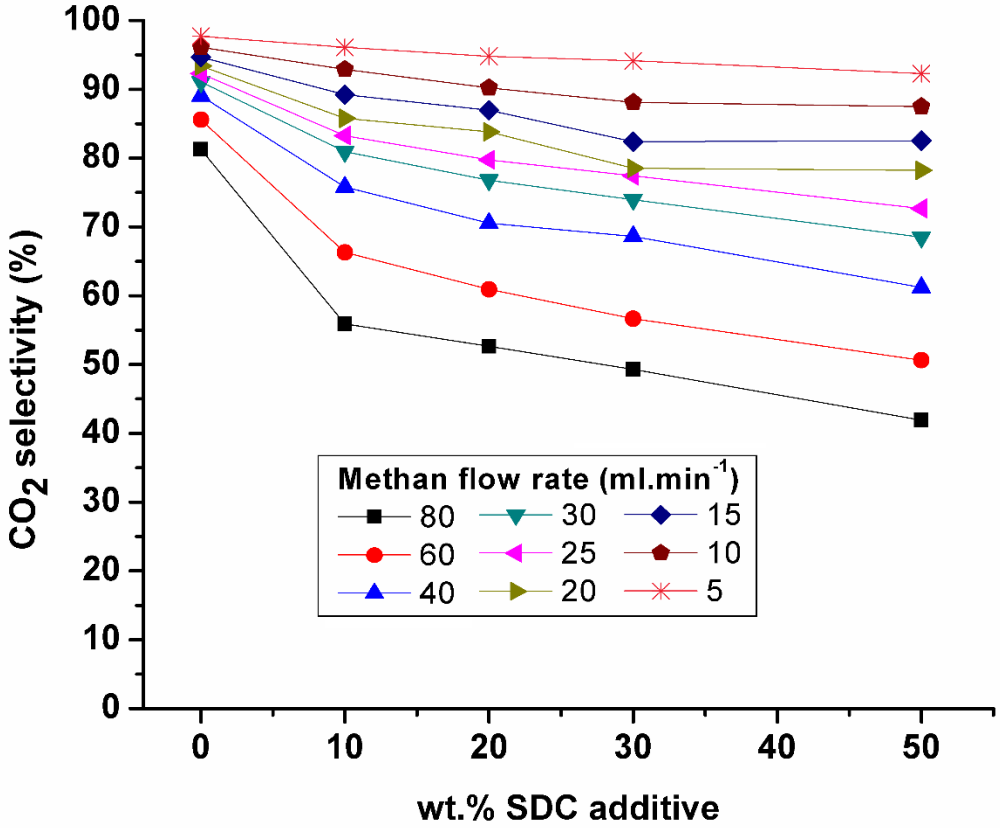

Figure 6.9 Methane sweeping gas flow rates influence on CO_2 selectivity through the SDC-SSC dual-phase membrane and SSC membrane at 900°C

6.4 Conclusion

This chapter's work sought to investigate the oxygen permeation and combustion performance of dual-phase OTMs comprised of SSC (perovskite-type) and SDC (fluorite-type) materials at

varying wt.% ratios. Material characterization (SEM and XRD) post sintering process, confirmed the feasibility of fabricating dense dual-phase OTMs. The total conductivity was found to decrease with an increase with the addition of SDC in the material composition. Dual-phase OTMs were shown to exhibit similar trends in inert (helium) gases; the oxygen permeation was found to increase with an increase in flow rate as well as an increase in temperature, but decrease with an increase in SDC wt.% within the OTM composition. Similar trends were confirmed using a methane sweeping gas, which enhanced the oxygen permeation flux compared to values achieved using helium. Furthermore, CO_2 selectivity was found to increase with a decrease in sweeping gas flow rate and SDC wt.% within the OTM composition.

Chapter 7 Approximating the performance and design of oxygen transport membrane reactors for the application of oxy-fuel combustion

7.1 Introduction

Previous chapters have demonstrated how operating conditions (e.g., membrane temperature, sweeping gas flow rate, and membrane compositions) can be modified to enhance OTM's oxygen permeation flux and maintain its chemical and mechanical structure. However, the work done in Chapters 3-6 are limited in scope by exclusively examining the oxygen permeation flux using a pure methane or CO_2 sweeping gas. As shown in Fig. 2.1, when an OTM is implemented for the application of oxy-fuel combustion, the incoming methane reacts with the permeating oxygen, converting a fraction of incoming methane in the sweeping gas to exhaust. As the sweeping gas moves downstream, its composition consists of unconverted fuel and exhaust which can influence the oxygen permeation flux of the OTM.

Despite previous chapters demonstrating OTMs with high oxygen permeation fluxes (>1 $ml.min^{-1}.cm^{-2}$) using a methane sweeping gas or CO_2-tolerant membrane, they fail to account for the overall application of implementing OTM technology for oxy-fuel combustion. As previously discussed in Chapter 2, a major contributing factor to the development of OTM technology is its financial cost (i.e., the overall performance of the OTM and size of the reactor). If current research only focuses on developing new materials, while disregarding OTMs application for oxy-fuel combustion, then it is difficult to determine the value of OTMs.

Alternative to building a scaled-up working demonstration, this chapter provides a simplified method for estimating an OTM's overall oxygen permeation flux for the application of oxy-fuel

combustion. The oxygen permeation flux of a dual-phase OTM is investigated under localized conditions that correspond to different regions of an applied OTM utilized for the application of oxy-fuel combustion in power generation facilities. Localized conditions are replicated by modifying the fuel to exhaust ratio in the sweeping gas composition.

The first objective in this chapter is to distinguish trends in the oxygen permeation flux as the sweeping gas composition is modified while maintaining the operating conditions of the OTM, such as reactor temperature and total flow rate of the sweeping gas. The second objective of this chapter is to establish the oxygen permeation flux as a function of the methane fraction in the sweeping gas composition. The determined function can be used to calculate the average oxygen permeation flux and approximate effective surface area of the OTM. Additionally, this chapter examines the potential advantage of repurposing the exhaust gases from the combustion to increase the incoming sweeping gas flow rate and improve the oxygen permeation performance of the OTM.

7.2 Experimental methods

Chapter 5 demonstrated a dual-phase OTM with a composition of 30 wt.% SDC and 70 wt.% SSC (30SDC-70SSC) exhibiting a steady oxygen permeability when subjected to pure CO_2 sweeping gases. Therefore, the 30SDC-70SSC dual-phase OTM is selected to be used as the investigated membrane composition in this work. The detailed fabrication processes of the 30SDC-70SSC dual-phase OTM is described in Chapter 5.

The oxygen permeation flux of the 30SDC-70SSC dual-phase OTM was studied using the experimental setup shown in Fig. 7.1. The experimental setup is similar to previous setups, as shown in Chapters 4-6, in which the fabricated planar membrane is sealed to quartz tubing using silver paste and subsequently heated in a vacuum split furnace to the desired temperature. Figure

7.1 differs from previous experimental setups by modifying the sweeping gas composition fed onto the OTM. After reaching the desired temperature, the membrane was fed a sweeping synthetic gas comprised of a varying methane fraction ranging from 0 to 1 on intervals of 0.25 while balanced with the addition of CO_2.

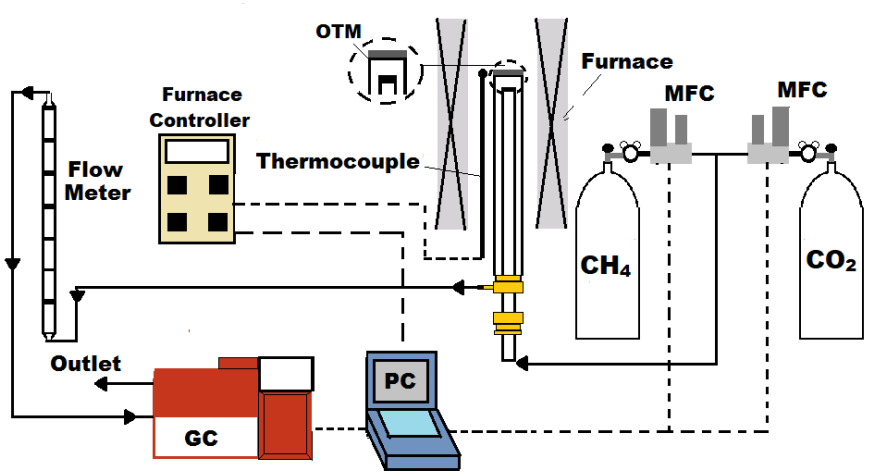

Figure 7.1 Experimental setup for planar OTM for estimating the overall oxygen permeation flux using a mixed sweeping gas composition

All oxygen permeation tests were conducted using a 30SDC-70SSC dual-phase composition. After fabrication, a dual-phase planar OTM was held at a fixed membrane temperature while subjected to a constant sweeping gas flow rate and sweeping gas composition. The oxygen permeation flux was studied at membrane temperatures of 800°C, 850°C, and 900°C, to simulate temperatures found in power generation facilities [28]. The oxygen permeation flux was also studied by varying the total flow rate of the sweeping gas from 10 to 40 ml.min^{-1} at intervals of 10 ml.min^{-1}. The previous calculation used to determine the oxygen permeation flux (Eq. 4.8) was adjusted to account for the additional CO_2 in the incoming sweeping gas composition:

$$J_{O_2} = (\dot{F}_{total}(2(X''_{CO_2} - X'_{CO_2}) + 1.5X''_{CO} + X''_{O_2} + 0.5X''_{C_2H_6}))/(2S) \quad \text{(Eq. 7.1)}$$

where X'_{CO_2} is the CO_2 fraction in the incoming sweeping gas composition introduced onto the OTM.

The calculated oxygen permeation flux results were fitted with respect to the methane fraction in the sweeping gas composition ($J_{O_2}(X_{CH_4})$). The data were fitted to a 2nd order polynomial using the Polyfit function in MATLAB, which returned a polynomial least-square regression. The average oxygen permeation flux ($J_{O_2}(\text{ave.})$) was calculated using the fitted function, bounded by the fraction of methane in the sweeping gas composition ranging from 0 to X'_{CH_4}, as shown in Eq. 7.2:

$$J_{O_2}(ave.) = \frac{\int_0^{X'_{CH_4}} J_{O_2}(X_{CH_4})\, dX_{CH_4}}{X'_{CH_4} - 0} \quad \text{(Eq. 7.2)}$$

where X'_{CH_4} is the fraction of methane introduced onto the permeation side of the 30SDC-70SSC dual-phase OTM. The average oxygen permeation flux was used to estimate the approximate effective surface area (AESA) needed to permeate a proportionate volume oxygen to permeation side for complete combustion with the fuel. Equation 7.3 shows the calculation for determining AESA where $\dot{F}_{total}$ is the total sweeping gas flow rate. The derivation of Eq. 7.3 can be found in Appendix B.

$$AESA = \frac{2(\dot{F}_{total} \times X'_{CH_4})}{J_{O_2}(ave.)} \quad \text{(Eq. 7.3)}$$

7.3 Results and discussion

7.3.1 Oxygen permeation flux under modified sweeping gas composition

The oxygen permeation flux was investigated by adjusting the membrane temperature, the total flow rate of the sweeping gas, and sweeping gas composition. Fig. 7.2 and 7.3 show the determined oxygen permeation flux results found using Eq. 7.1 and their respective fitted polynomial curves. All fitted polynomials exhibited an r^2 value higher than 0.97 indicating a well fit regression to the experimental data. Higher order polynomial fits displayed weaker r^2 value less than 0.97, meaning

a worse fit regression to the experimental data. The polynomial coefficients of the fitted curve can be found in Table 7.1 with their respective r^2 value.

Table 7.1 Polynomial coefficients of fitted curves of the oxygen permeation flux as a function of methane fraction in the sweeping gas compositions while subjected to varying sweeping gas flow rates and membrane temperatures

Temperature (°C)	**Flow Rate ($ml.min^{-1}$)**	**Coefficients**			**r^2**
800		*a*	*b*	*c*	
	10	-0.1836	0.7197	0.0486	0.9903
	20	-0.7426	1.4559	0.082	0.9990
	30	-0.5383	1.756	0.1204	0.9981
	40	-0.2523	1.7723	0.1838	0.9931
850		*a*	*b*	*c*	
	10	0.0831	0.5626	0.0959	0.976
	20	-0.5765	1.4376	0.1335	0.9811
	30	-0.1504	1.5606	0.1652	0.9995
	40	-0.328	1.9474	0.2237	0.9981
900		*a*	*b*	*c*	
	10	0.2454	0.7504	0.129	0.9745
	20	-0.1134	1.1725	0.2672	0.9899
	30	-0.236	1.4966	0.3996	0.9943
	40	-0.1522	1.7885	0.4927	0.9737

Figure 7.2 shows the oxygen permeation flux under varying sweeping gas compositions at a total flow rate of 20 $ml.min^{-1}$ while held at membrane temperature of 800, 850, and 900°C. The oxygen flux results for other cases in which the total sweeping gas flow rate was 10, 30, or 40 $ml.min^{-1}$ while held at a membrane temperature of 800, 850, and 900°C is shown in Appendix C. It can be observed that the oxygen permeation flux is found to decline with a decrease in reactor temperature or a decrease of the methane fraction in the sweeping gas composition. Although the

decrease in the methane fraction was offset by the increase in CO_2 in the sweeping gas, no membrane degradation was observed for any sweeping gas mixture, except for a pure CO_2 sweeping gas.

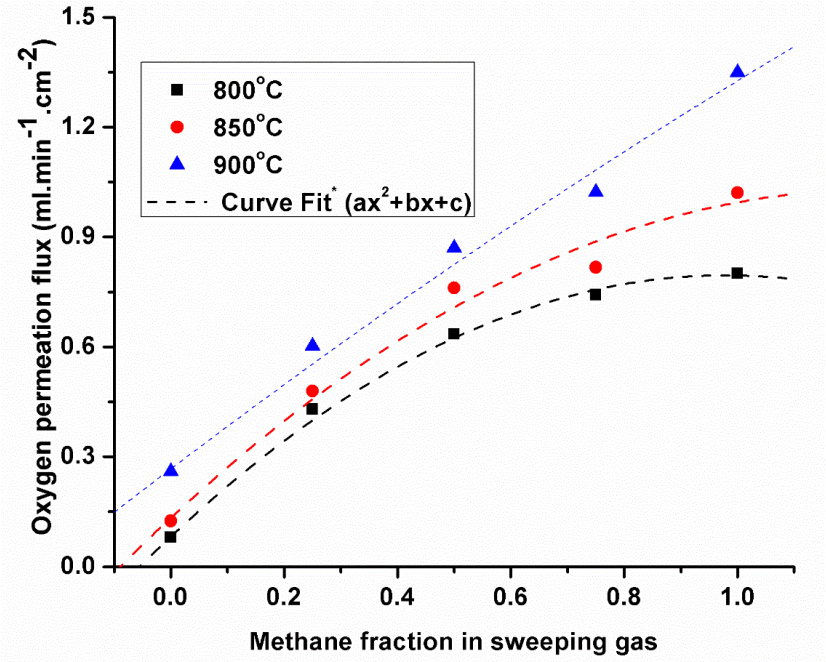

Figure 7.2 Oxygen permeation flux of 30SDC-70SSC dual-phase OTM subjected to varying membrane temperatures and sweeping gas compositions with a constant total sweeping gas flow rate of 20 $ml.min^{-1}$. *Polynomial curve fit coefficients can be found in Table 7.1

The highest oxygen permeation flux was found to be 1.35 $ml.min^{-1}.cm^{-2}$ at a membrane temperature of 900°C with a methane fraction of 1. The lowest oxygen permeation flux was found to be 0.08 $ml.min^{-1}.cm^{-2}$ at a reactor temperature of 800°C using at a methane fraction of 0. The decrease in the oxygen permeation flux with respect to temperature is a consequence of the change in the material's diffusion coefficient, previously discussed in Chapter 3. The observed decline in the oxygen permeation flux with a decrease in methane fraction indicates that the membrane's permeability is impacted by the increase of CO_2 in the sweeping gas composition. As shown in Chapter 6, as well as previous works, a methane sweeping gas can maintain a higher permeation flux due to its ability to react with the permeated oxygen and improve the oxygen chemical gradient across the OTM [36–38,52,61,174]. However, the additional presence of CO_2 in the sweeping gas

composition impedes the reaction between methane and permeated oxygen, thus decreasing the oxygen chemical gradient across the OTM and reducing the oxygen permeation flux.

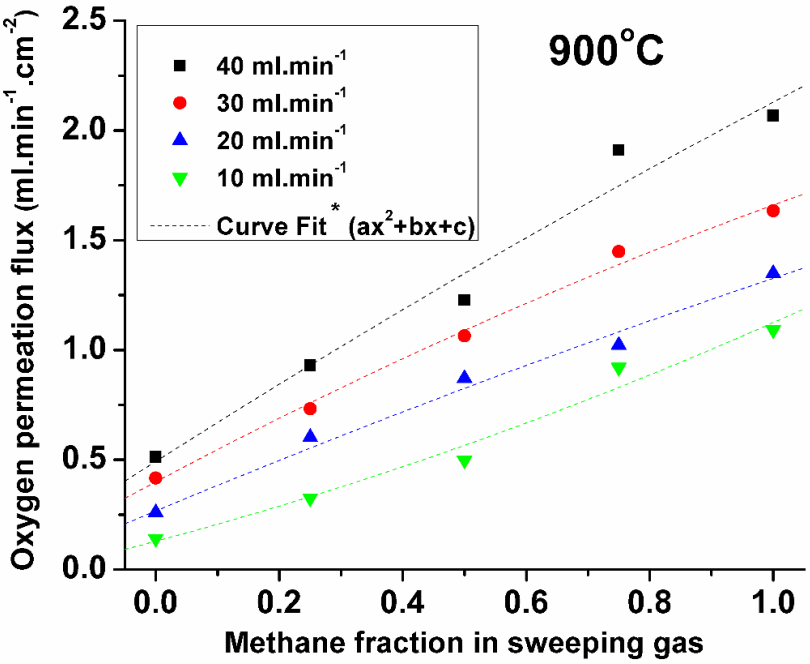

Figure 7.3 Oxygen permeation flux of 30SDC-70SSC dual-phase OTM subjected to varying sweeping gas compositions and flow rates while held at a constant membrane temperature of 900°C. *Polynomial curve fit coefficients can be found in Table 7.1

The direct correlation between the oxygen permeation flux and methane fraction in the sweeping gas is also observed in Fig. 7.3, which shows the oxygen permeation flux under varying total sweeping gas flow rates and compositions while maintained at a membrane temperature of 900°C. The oxygen flux results for other cases in which the membrane temperature was 800°C or 850°C while subjected to varying total sweeping gas flow rates and compositions is shown in Appendix D. The highest and lowest oxygen permeation fluxes were found to be 2.06 $ml.min^{-1}.cm^{-2}$ at a 40 $ml.min^{-1}$ flow rate of pure methane and 0.1448 $ml.min^{-1}.cm^{-2}$ at a 10 $ml.min^{-1}$ flow rate of pure CO_2. As stated before, the relationship between the oxygen permeation flux and methane fraction is a result of CO_2 in the sweeping gas composition impeding the reaction needed to maintain the oxygen chemical gradient across the OTM. Despite this, the oxygen permeation flux

still increases with an increase in the total flow rate of the sweeping gas, indicating that the oxygen chemical gradient across the OTM is improved with an increase in total sweeping gas flow rate, regardless of its composition.

The oxygen permeation flux results shown in Fig. 7.2 and 7.3 provide a clearer understanding of the overall oxygen permeation flux of OTMs. On a larger scale, implemented OTMs utilized for the application of oxy-fuel combustion in power generation facilities will exhibit a similar trend in which the oxygen permeation flux will be lower at regions farther away from the inlet. Similar findings have been observed in numerical studies [124,181,182]. Alternative to examining the oxygen permeation flux under localized conditions found at different regions of a large scale OTM, the average oxygen permeation flux could be estimated to provide a deeper insight into the OTM's overall performance.

7.3.2 Average oxygen permeation flux and AESA

Figure 7.4 shows the average oxygen permeation flux of the OTM at varying sweeping gas flow rates and membrane temperatures. The average oxygen permeation flux was calculated using Eq. 7.2 to describe the average oxygen permeability of the entire OTM when implemented for the application of oxy-fuel combustion. As shown in Fig. 7.4, the average oxygen permeation flux is observed to increase with the total sweeping gas flow rate and membrane temperature, as demonstrated in previous chapters. However, the average oxygen permeation flux is lower compared to the determined oxygen permeation flux of OTMs subjected to a pure methane sweeping gas. For example, as shown in Fig. 7.4, the average oxygen permeation flux of the OTM held at a constant temperature 900°C while subjected to a 30 $ml.min^{-1}$ total flow rate of the sweeping gas is 1.06 $ml.min^{-1}.cm^{-2}$. As shown in Fig. 7.3, the oxygen permeation flux subjected to the 30 $ml.min^{-1}$ flow rate of a pure methane sweeping gas while held at a membrane temperature

of 900°C is 1.63 ml.min^{-1}.cm^{-2}. The average oxygen permeation flux is lower since it accounts for the oxygen permeability throughout the entire reactor of which the methane fraction is declining as the sweeping gas moves downstream.

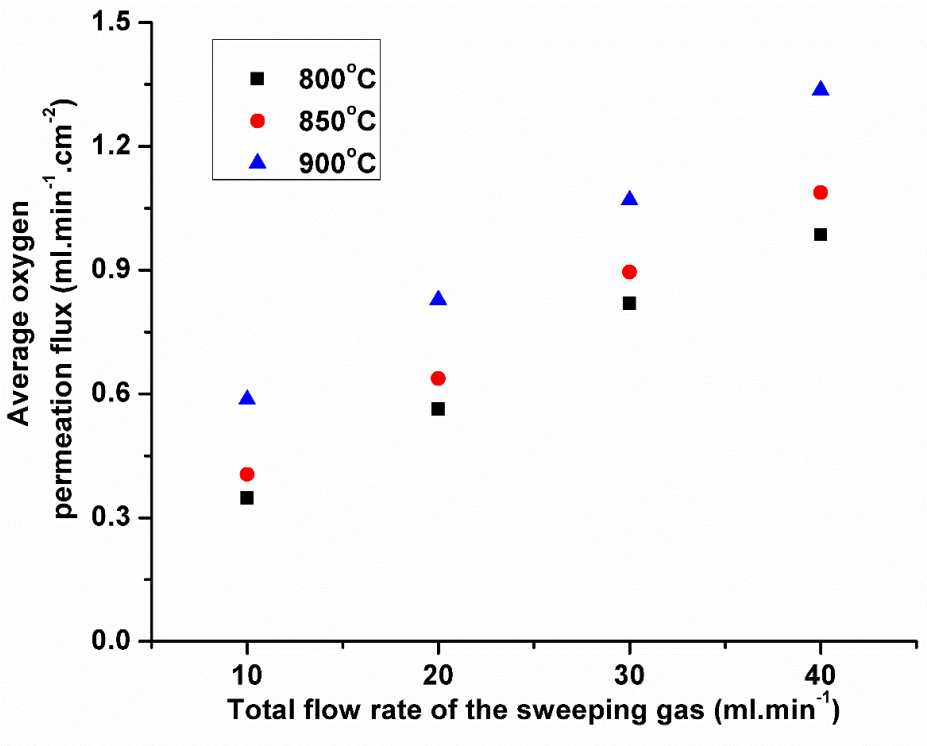

Figure 7.4 Average oxygen permeation flux of 30SDC-70SSC dual-phase OTM estimated at varying total sweeping gas flow rates and membrane temperatures

Despite exhibiting a lower oxygen permeation flux compared to the results determined using a pure methane sweeping gas, the average oxygen permeation flux is still higher than 1 ml.min^{-1}.cm^{-2} under certain operating conditions. The highest average oxygen permeation flux was found to be 1.33 ml.min^{-1}.cm^{-2} at 900°C with a total sweeping gas flow rate of 40 ml.min^{-1}. Furthermore, the average oxygen permeation flux for the 30SDC-70SSC dual-phase OTM is found to be higher than 1 ml.min^{-1}.cm^{-2} in all cases with a total flow rate 40 ml.min^{-1}, regardless of the membrane temperature.

Using a combination of the average oxygen permeation flux results shown in Fig. 7.4 and Eq. 7.3, the AESA of the OTM needed to provide a sufficient volume of oxygen for complete

combustion can be determined. Figure 7.5 shows the AESA at varying total flow rates of the sweeping gas and reactor temperatures. The results demonstrate that the AESA increases with the total flow rate of the sweeping gas, suggesting that the higher total flow rate requires a larger volume of permeated oxygen to react with the larger volume of fuel completely. Additionally, Fig. 7.5 shows the AESA decreases with an increase in reactor temperature, indicating that the enhanced oxygen permeation flux from the rise in the reactor temperature reduces the reactor size needed for a complete combustion. For example, the highest AESA of the OTM is 81.15 cm^2 at a 40 $ml.min^{-1}$ total flow rate of the sweeping gas and reactor temperature of 800°C. The lowest AESA is 34.32 cm^2 at a 10 $ml.min^{-1}$ total flow rate of the sweeping gas flow rate and a reactor temperature of 900°C. These estimations provide a deeper insight into the financial costs of implementing OTM design and operating them under certain conditions for the application of oxy-fuel combustion. Although most developed materials are compared based on their oxygen permeation flux, this AESA calculation allows a more practical comparison for evaluating the monetary value of implementing OTMs for the application of oxy-fuel combustion.

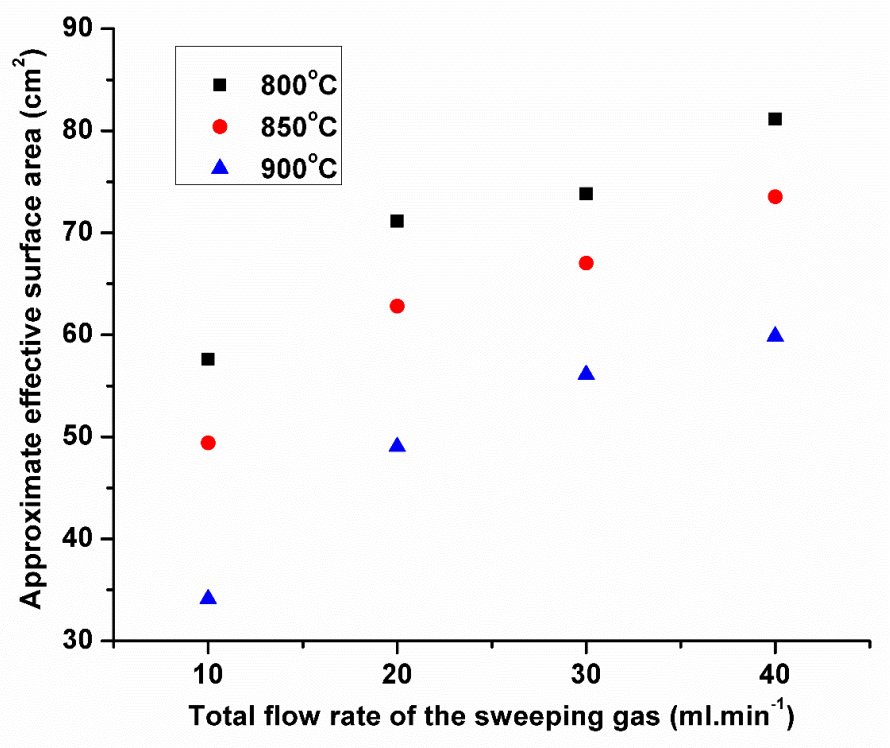

Figure 7.5 Approximate effective surface area of 30SDC-70SSC dual-phase OTM estimated at varying total sweeping gas flow rates and membrane temperatures

7.3.3 Estimating the average oxygen permeation flux and AESA under recirculated exhaust gas conditions

Chapter 4, 5, and 6 have shown that increasing the sweeping gas flow rate consequently increases the oxygen chemical gradient across the OTM, ultimately improving the oxygen permeation flux. Acknowledging this, several researchers have suggested recirculating exhaust gases back into the incoming sweeping gas to increase the total flow rate of the sweeping gas and improve the oxygen permeation flux [13,22,28,52,183]. This concept is furthered explored by defining the methane fraction in the incoming sweeping gas composition as the proportion of the incoming methane flow rate ($\dot{F}_{CH_4}$) and total flow rate of sweeping gas ($\dot{F}_{total}$), as shown in Eq. 7.4:

$$X'_{CH_4} = \frac{\dot{F}_{CH_4}}{\dot{F}_{total}} = \frac{\dot{F}_{CH_4}}{\dot{F}_{CH_4}+\dot{F}_{CO_2}} \qquad \text{(Eq. 7.4)}$$

where the total sweeping gas flow rate is defined as the summation between the incoming methane flow rate and recirculated exhaust gas flow rate ($\dot{F}_{CO_2}$). From Eq. 7.4 and the fitted 2nd order polynomials, X'_{CH_4} was determined by modifying the methane flow rate from 10 to 40 ml.min^{-1} on increments of 2 ml.min^{-1} while also modifying the total sweeping gas flow rate from 10 to 40 ml.min^{-1} on increments of 10 ml.min^{-1}.

Figure 7.6 shows the average oxygen permeation flux subjected to a modified incoming methane flow rate and total flow rate of the sweeping gas ranging from 10 to 40 ml.min^{-1} while maintained at a membrane temperature of 900°C. The average oxygen permeation flux subjected to modified incoming methane and sweeping gas flow rates held at other membrane temperatures such as 800°C and 850°C are shown in Appendix E. The average oxygen permeation flux is observed to increase as the total sweeping gas flow rate increases while maintaining a constant methane flow rate. For example, at a constant methane flow rate of 10 ml.min^{-1}, the average oxygen permeation flux is 0.59 ml.min^{-1}.cm^{-2} and 0.71 ml.min^{-1}.cm^{-2} at a total sweeping gas flow rate of 10 and 40 ml.min^{-1}, respectively. The difference in the average oxygen permeation flux as the total sweeping gas flow rate increases is attributed to the increase in the oxygen chemical gradient across the membrane. These results demonstrate that recirculating the exhaust into the incoming sweeping gas does improve the oxygen permeation flux.

However, when held at a constant total sweeping gas flow rate, Fig. 7.6 shows the average oxygen permeation flux decreasing with the addition of CO_2 in the incoming sweeping gas. At a total flow rate of 40 ml.min^{-1}, the average oxygen permeation flux is 1.34 ml.min^{-1}.cm^{-2} and 0.71 ml.min^{-1}.cm^{-2} at a methane flow rate of 40 and 10 ml.min^{-1}, respectively. The decline in the average oxygen permeation flux is related to the fraction of CO_2 in the sweeping gas composition which reduces the oxygen permeation flux by impeding the reaction between methane and permeated

oxygen, as previously demonstrated in Fig 7.2 and 7.3. Therefore, although the recirculating exhaust does improve the average oxygen permeation flux by increasing the total flow rate of the sweeping gas, it will always be lower compared to using a pure methane sweeping gas at the same total sweeping gas flow rate.

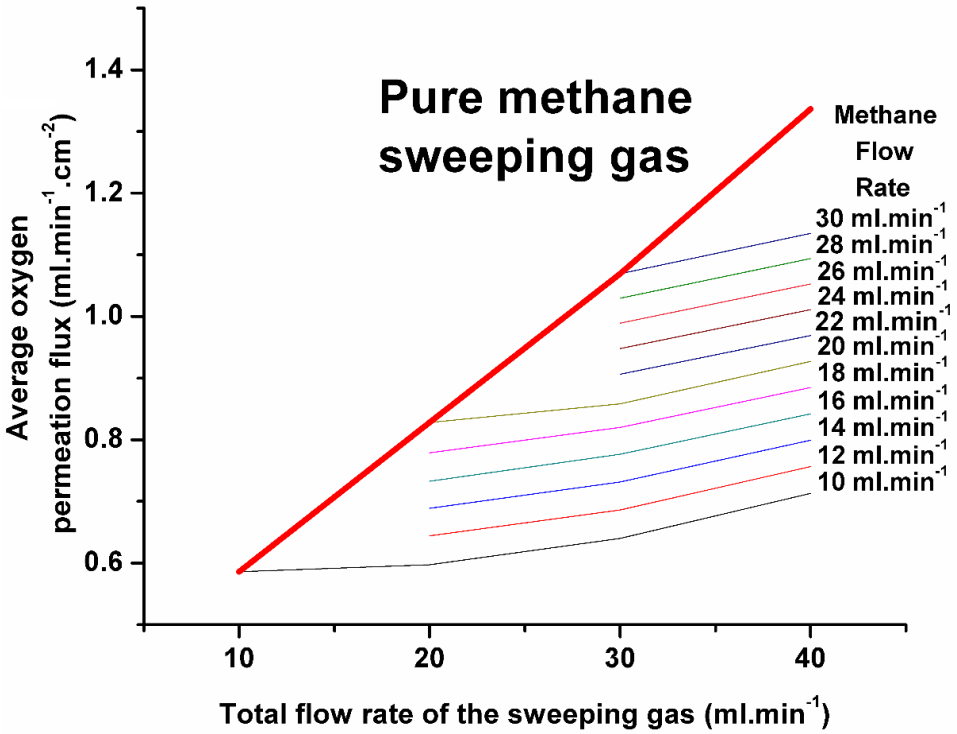

Figure 7.6 Average oxygen permeation flux subjected to modified incoming methane and total sweeping gas flow rate ranging from 10 to 40 ml.min^{-1} while maintained at a membrane temperature of 900°C

Despite the lower average oxygen permeation flux with the addition of recirculated exhaust into the sweeping gas compared to using a pure methane sweeping gas, the results shown in Fig. 7.6 highlight a potential design advantage. Specifically, a comparable average oxygen permeation flux can be achieved by increasing the total sweeping gas flow rate with recirculating exhaust, alternative to using a pure methane sweeping gas. For example, an OTM at a reactor temperature of 900°C subjected to 20 ml.min^{-1} pure methane sweeping gas will exhibit an average oxygen permeation flux of 0.83 ml.min^{-1}.cm^{-2}. A similar average oxygen permeation flux (0.82 ml.min^{-}

^{1}.cm^{-2}) can be achieved by at total sweeping gas flow rate of 30 ml.min^{-1} with a methane flow rate of 18 ml.min^{-1}, indicating that the same oxygen permeability can be achieved by the OTM using less fuel, which may be favorable to specific system designs.

However, when considering an OTM design for a specific system, the membrane size must also be considered. Figure 7.7 shows the AESA subjected to modified methane and total sweeping gas flow rates while held at a membrane temperature of 900°C. The AESA subjected to modified methane and total sweeping gas flow rates while held at other membrane temperatures such as 800°C and 850°C are shown in Appendix F. It observed in Fig. 7.7 that at a constant total sweeping gas flow rate the AESA decreases with a decrease in the methane flow rate. At a constant total sweeping gas flow rate of 30 ml.min^{-1}, the AESA was determined to be 56.1 and 31.2 cm^{2} at a methane flow rate of 30 and 10 ml.min^{-1}. The reduction in the AESA is a result of the smaller fraction of methane in the sweeping gas composition. The smaller fraction of methane in the sweeping gas composition requires less permeated oxygen for complete combustion, thus reducing the effective surface area of the OTM.

Furthermore, the AESA is also reduced by an increase in total sweeping gas flow rate when held at a constant methane flow rate. At a constant methane flow rate of 20 ml.min^{-1}, the AESA was determined to be 49.0 and 43.1 cm^{2} at a total sweeping gas flow rate of 20 and 40 ml.min^{-1}. These results indicate that the AESA decreases due to the improved average oxygen permeation flux achieved by the increased total sweeping gas flow rate. The decline in the required membrane size further solidifies the advantage of recirculating exhaust into the incoming sweeping gas composition and highlights additional measures that should be accounted for when designing OTMs.

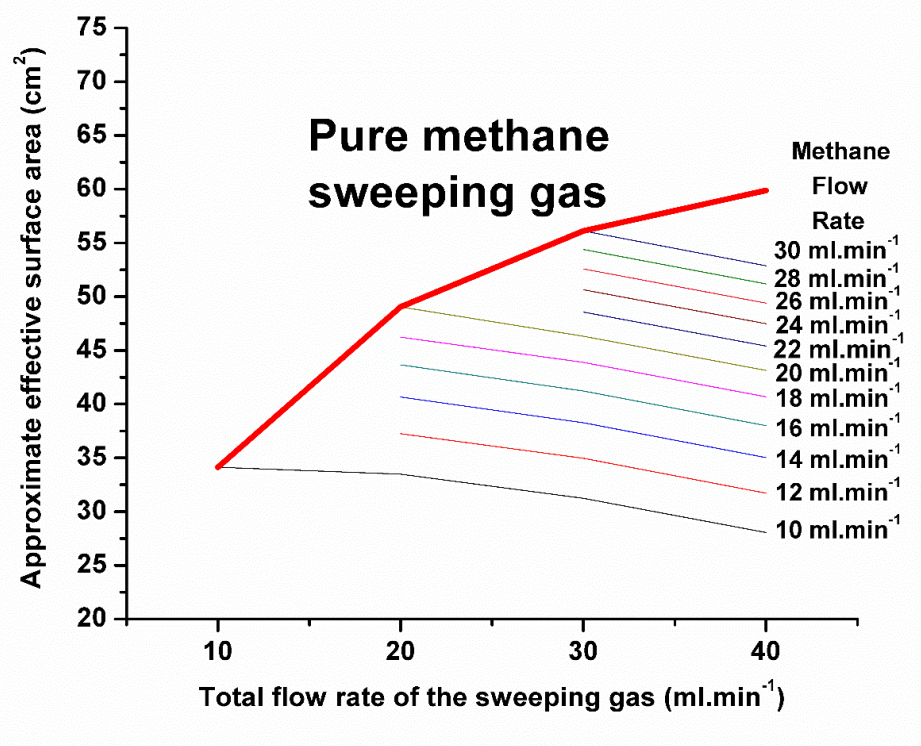

Figure 7.7 AESA subjected to modified incoming methane and total sweeping gas flow rate ranging from 10 to 40 ml.min^{-1} while maintained at a membrane temperature of 900°C

7.4 Conclusion

A new method for evaluating OTMs for the application of oxy-fuel combustion is presented in this study. Using a common experimental setup, the oxygen permeation flux of an OTM was evaluated at varying sweeping gas flow rates and membrane temperatures while also modifying the methane fraction in the sweeping gas composition. It was discovered that the oxygen permeation flux of the planar membrane decreased with the reduction in the methane fraction in the sweeping gas composition. The experimental data was fitted to a 2nd order polynomial that provided a quantifiable relationship between the oxygen permeation flux and methane fraction in the sweeping gas composition.

The fitted curves provided a deeper insight into the overall oxygen permeation flux and approximate effective surface area. It was found that the overall oxygen permeation flux increased with an increase in the total flow rate of the sweeping gas and reactor temperature. The

approximate effective surface area was found to decrease with the reactor temperature but increase with an increase in the total flow rate of the sweeping gas, since a larger volume of methane requires more oxygen for a complete combustion. Furthermore, the average oxygen permeation flux was discovered to increase with an increase in the total flow rate of the sweeping gas by the addition of recirculated CO_2. However, the increase in the total flow rate of the sweeping gas by the addition of repurposed exhaust still exhibits a lower overall oxygen permeation flux in comparison to a pure methane sweeping gas with the same total flow rate. This suggests that the addition of exhaust gases in the incoming sweeping gas is a factor that influences the oxygen permeability of an OTM and may be favorable in specific system designs.

Chapter 8 Conclusion and future work

8.1 Summary and conclusions

The first component of this thesis investigated the oxygen diffusivity and oxygen permeation performance of a single-phase crystal structure, $SrSc_{0.1}Co_{0.9}O_{3-\delta}$ (SSC), and focused on the feasibility of utilizing OTMs for the application of oxy-fuel combustion. The following conclusions were drawn from this portion of the thesis:

(1) The surface exchange and oxygen chemical diffusion coefficients are revealed to be superior to other commonly investigated materials ($La_{0.6}Sr_{0.4}Co_{0.2}Fe_{0.8}O_{3-\delta}$ and $Ba_{0.5}Sr_{0.5}Co_{0.8}Fe_{0.2}O_{3-\delta}$) at different membrane temperatures.

(2) SSC's average oxygen diffusion coefficient found experimentally is observed to be an order of magnitude higher than the results determined in the molecular dynamics simulation at all investigated temperatures. The difference between the experimental and numerical results is potentially attributed to the presence of grain boundaries in the perovskite structure, which have been documented to enhance oxygen ion diffusivity due to a low coordination number at the grain boundary interfaces [184–188].

(3) The oxygen permeation flux of SSC is determined to be higher than the oxygen permeation flux of $La_{0.6}Sr_{0.4}Co_{0.2}Fe_{0.8}O_{3-\delta}$ (LSCF) due to SSC's superior surface exchange and oxygen chemical diffusion coefficients. The oxygen permeation flux is also shown to increase with an increase in methane flow rate on the permeation side of the OTM. Furthermore, the oxygen permeation flux is found to increase with membrane temperature which enhances the surface exchange reaction and oxygen diffusion coefficients in the SSC OTM.

(4) The oxygen permeation flux is found to be consistent for an LSCF planar and LSCF tubular OTM with the same effective surface area and membrane thickness. The tubular membrane

is shown to exhibit a lower oxygen permeation flux due to its larger thickness (1.1 mm) compared to thinner membranes (0.44 mm), which reduces the oxygen partial pressure gradient across the OTM. The larger thickness of the LSCF tubular OTM exposes a limitation for implementing OTMs for the application of oxy-fuel combustion under a tubular configuration.

(5) The highest CO_2 selectivity of the SSC planar OTM is determined to be 98%, indicating the potential for the application of oxy-fuel combustion.

The second component of this thesis examined the material properties and oxygen permeation performance of dual-phase OTMs under modified membrane compositions using SSC and $Sm_{0.2}Ce_{0.8}O_{1.9-\delta}$ (SDC). Major conclusions are described below:

(1) When exposed to a pure CO_2 atmosphere, a single-phase SSC membrane exhibits a modification in its chemical structure, morphology, ionic and electronic conductivity, and oxygen permeability due to a carbonate formation on the A-site of the perovskite-type material. The poor chemical stability of SSC in CO_2 atmospheres signifies the need for dual-phase OTM compositions.

(2) The addition of SDC in the OTM composition reduces the growth rate of the carbonate on the SSC material. A 30 wt.% SDC-70 wt.% SSC dual-phase OTM is observed to achieve a steady oxygen permeation flux during a long-term oxygen permeation test using a CO_2 sweeping gas. The steady oxygen permeation flux was achieved due to the formation of a thick carbonate layer on the permeation surface of the dual-phase OTM, separating the CO_2 sweeping gas from the uncompromised SSC material.

(3) The carbonate formation growth rate is observed to vary with CO_2 sweeping gas flow rates and membrane temperatures. The increase in the CO_2 sweeping gas flow rate furthers the

reaction between the SSC material and CO_2 sweeping gas due to the larger volume of CO_2 exposed to the permeation surface causing the oxygen permeation flux to vary. The increase in membrane temperature is also observed to increase the carbonate formation growth rate on the permeation surface. In permeation tests where the membrane temperature was 800°C, the carbonate formation was not observed to protrude into the internal structure of the membrane.

(4) When using a helium or methane sweeping gas, the oxygen permeation flux diminishes with an increase in SDC wt.% in the membrane composition. The decrease in the oxygen permeation flux with more SDC in the dual-phase membrane composition is a result of the limited electronic pathways needed to maintain the oxygen permeation flux.

(5) All dual-phase membrane compositions swept with pure methane exhibited a higher oxygen permeation flux than when swept with helium. The difference in the oxygen permeation flux, relative to the variation in the sweeping gas composition, attributes to the higher oxygen partial pressure gradient maintained across the OTM by the reaction between methane and the permeated oxygen.

(6) Despite the decline in the oxygen permeation flux with the addition of SDC in the dual-phase membrane composition, the oxygen permeation flux using a methane sweeping gas is observed to be high (>1 $ml.min^{-1}.cm^{-2}$), signifying a superior oxygen permeability compared to other developed materials. Furthermore, at methane flow rates lower than 20 $ml.min^{-1}$, the CO_2 selectivity is greater than 80% for all investigated dual-phase membrane compositions, indicating the potential to be used for the application of oxy-fuel combustion.

The final component of this thesis develops and investigates a new method for evaluating OTMs for the application of oxy-fuel combustion. The following significant conclusions can be drawn from this portion of the thesis:

(1) The oxygen permeation flux decreases with a reduced methane fraction in the sweeping gas composition. In the presence of CO_2, the reaction between methane and permeated oxygen is hindered, decreasing the oxygen partial pressure gradient across the membrane and the OTM's oxygen permeation flux.

(2) Oxygen permeation flux results were fitted to a 2^{nd} order polynomial using the Polyfit function in MATLAB, which returned a polynomial least-square regression. The fitted polynomials provided a relation between the oxygen permeation flux and methane fraction in the sweeping gas composition. From the determined polynomial functions, the overall oxygen permeation flux and the approximate effective surface area of an OTM can be determined for a specific total flow rate of the sweeping gas or membrane temperature.

(3) The overall oxygen permeation flux is shown to increase with an increase in the total flow rate of the sweeping and membrane temperature. The approximate effective surface area is also discovered to decrease with membrane temperature. However, the approximate effective surface area is shown to increase with an increase in the total flow rate of the sweeping gas, since a larger volume of methane requires more oxygen for a complete combustion.

(4) The overall oxygen permeation flux is discovered to increase with an increase in the total flow rate of the sweeping gas by the addition of recirculated CO_2. However, the increase in the total flow rate of the sweeping gas by the addition of repurposed exhaust still exhibits a lower overall oxygen permeation flux in comparison to a pure methane sweeping gas

with the same total flow rate. This suggests that the addition of exhaust gases in the incoming sweeping gas is a factor that influences the oxygen permeability of an OTM and may be favorable in specific system designs.

8.2 Recommendations for future research

Based on the work conducted in this thesis, the following areas should be considered for further investigation:

(1) There has been little work done to investigate grain boundary structure, which can influence the oxygen ion diffusion throughout a membrane [184–188]. Using electron backscatter diffraction (EBSD), coincident site lattices, grain orientation, texture, grain size and the angle between grains can be characterized to provide a detailed understanding of the single crystal membrane structure [134]. Characterized grain boundary structures can then be used to develop a molecular dynamics simulation that investigates the oxygen diffusivity through perovskite grain boundaries.

(2) Alternative to fabricating a single component tubular OTM, a multilayer tubular OTM can be fabricated to reduce the thickness needed to maintain the mechanical integrity of the membrane structure. In doing so, the oxygen chemical gradient and oxygen permeation flux could be improved. This new configuration would further support the potential for OTM technology to be implemented for the application of oxy-fuel combustion.

(3) The method presented in Chapter 7 is a new approach for evaluating the performance of OTMs for the application of oxy-fuel combustion. Future research should focus on validating this approach through the construction of a working demonstration. Once validated, this method can be used to evaluate other perovskite-type materials, providing a better standard for designing OTMs for the application of oxy-fuel combustion.

Appendix A

Derivation of the oxygen permeation flux (J_{O_2}) using a methane sweeping gas

$$\dot{n}'_{CH_4}CH_4 + \dot{n}'_{O_{2,perm}}O_2 \rightarrow \dot{n}''_{CO_2}CO_2 + \dot{n}''_{CO}CO + \dot{n}''_{C_2H_6}C_2H_6 + \dot{n}''_{CH_4}CH_4 + \dot{n}''_{O_2}O_2 + \dot{n}''_{H_2O}H_2O \quad \text{(Eq. 0.1)}$$

The elemental conservation of C, O, and H results in:

$$\textbf{C:}\ \dot{n}'_{CH_4} = \dot{n}''_{CO_2} + \dot{n}''_{CO} + 2\dot{n}''_{C_2H_6} + \dot{n}''_{CH_4} \quad \text{(Eq. 0.2)}$$

$$\textbf{H:}\ 4\dot{n}'_{CH_4} = 6\dot{n}''_{C_2H_6} + 4\dot{n}''_{CH_4} + 2\dot{n}''_{H_2O} \quad \text{(Eq. 0.3)}$$

$$\textbf{O:}\ 2\dot{n}'_{O_{2,perm}} = 2\dot{n}''_{CO_2} + \dot{n}''_{CO} + 2\dot{n}''_{O_2} + \dot{n}''_{H_2O} \quad \text{Eq. 0.4)}$$

$$\dot{n}_{total} = \dot{n}''_{CO_2} + \dot{n}''_{CO} + \dot{n}''_{C_2H_6} + \dot{n}''_{CH_4} + \dot{n}''_{O_2} + \dot{n}''_{H_2O} \quad \text{(Eq. 0.5)}$$

$$X''_i = \dot{n}''_i/\dot{n}_{total} = \dot{F}''_i/\dot{F}_{total} \quad \text{(Eq. 0.6)}$$

Eq. 4.2 can be rearranged as:

$$\dot{n}'_{CH_4} - \dot{n}''_{CH_4} = \dot{n}''_{CO_2} + \dot{n}''_{CO} + 2\dot{n}''_{C_2H_6} \quad \text{(A.1)}$$

$\dot{n}''_{H_2O}$ can be determined using Eq. 4.3:

$$\dot{n}''_{H_2O} = 2\left(\dot{n}'_{CH_4} - \dot{n}''_{CH_4}\right) - 3\dot{n}''_{C_2H_6} \quad \text{(A.2)}$$

$\dot{n}'_{O_{2,perm}}$ can be determined using Eq. 4.4 and combining the A.1 and A.2:

$$\dot{n}'_{O_{2,perm}} = \dot{n}''_{CO_2} + \frac{1}{2}\dot{n}''_{CO} + \dot{n}''_{O_2} + \left(\dot{n}'_{CH_4} - \dot{n}''_{CH_4}\right) - \frac{3}{2}\dot{n}''_{C_2H_6} \quad \text{(A.3)}$$

$$\dot{n}'_{O_{2,perm}} = \dot{n}''_{CO_2} + \frac{1}{2}\dot{n}''_{CO} + \dot{n}''_{O_2} + \dot{n}''_{CO_2} + \dot{n}''_{CO} + 2\dot{n}''_{C_2H_6} - \frac{3}{2}\dot{n}''_{C_2H_6} \quad \text{(A.4)}$$

Simplified to:

$$\dot{n}'_{O_{2,perm}} = 2\dot{n}''_{CO_2} + \frac{3}{2}\dot{n}''_{CO} + \dot{n}''_{O_2} + \frac{1}{2}\dot{n}''_{C_2H_6} \quad \text{(A.5)}$$

Since,

$$J_{O_2} = \frac{\dot{n}'_{O_{2,perm}}}{2S} = \frac{\dot{n}_{total} \cdot X'_{O_{2,perm}}}{2S} \quad \text{(A.6)}$$

Then J_{O_2} is defined as

$$J_{O_2} = (\dot{n}_{total}(2X''_{CO_2} + 1.5X''_{CO} + X''_{O_2} + 0.5X''_{C_2H_6}))/(2S)$$

Appendix B

Derivation of the approximate effective surface area (AESA)

The global reaction for methane combustion indicates the ratio between fuel and oxygen is 1 to 2, as shown in the equation below:

$$CH_4 + 2O_2 \rightarrow CO_2 + 2H_2O$$

The fuel to air ratio can be applied to the volumetric flow rate of methane and permeating oxygen by the approximate effective surface area, as shown in the following equation:

$$\frac{1}{2} = \frac{\dot{\mathrm{F}}_{CH_4}}{J_{O_2}(ave.) * AESA}$$

where $J_{O_2}(ave.)$ is the average oxygen permeation flux and $\dot{\mathrm{F}}_{CH_4}$ is the methane flow rate. $\dot{\mathrm{F}}_{CH_4}$ can be further defined as $\dot{\mathrm{F}}_{CH_4} = (\dot{\mathrm{F}}_{total} \times X'_{CH_4})$ where $\dot{\mathrm{F}}_{total}$ is the total sweeping gas flow rate and X'_{CH_4} is the fraction of methane introduced onto the permeation side of the OTM. The approximate effective surface area can then be defined as:

$$AESA = \frac{2(\dot{\mathrm{F}}_{total} \times X'_{CH_4})}{J_{O_2}(ave.)}$$

Appendix C

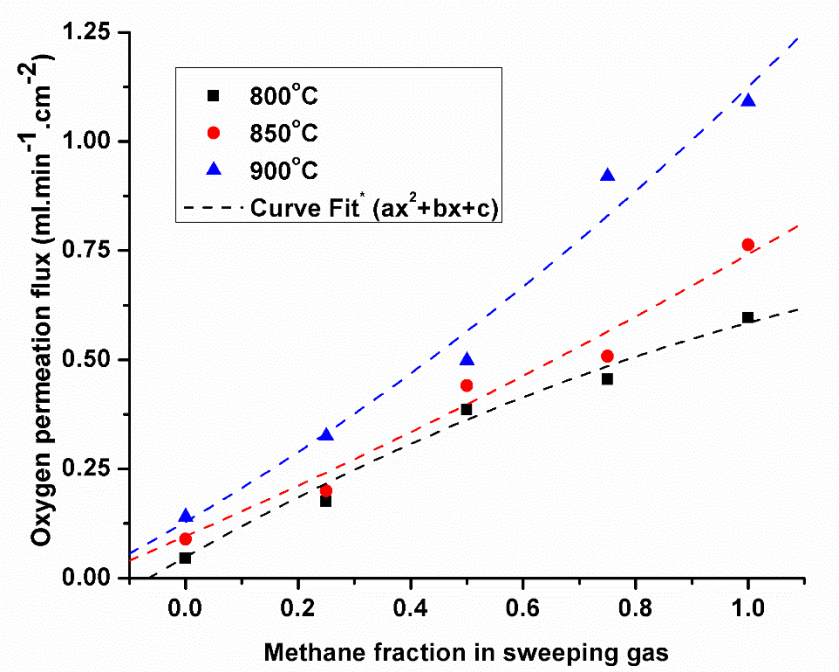

Figure C.1 Oxygen permeation flux of 30SDC-70SSC dual-phase OTM subjected to varying temperatures and sweeping gas compositions with a constant total sweeping gas flow rate of 10 $ml.min^{-1}$. *Polynomial curve fit coefficients can be found in Table 7.1

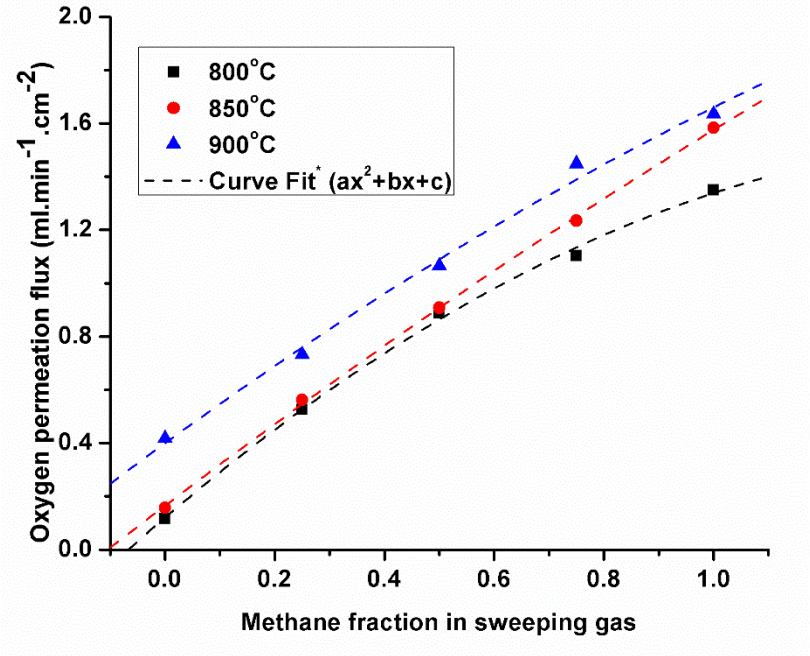

Figure C.2 Oxygen permeation flux of 30SDC-70SSC dual-phase OTM subjected to varying membrane temperatures and sweeping gas compositions with a constant total sweeping gas flow rate of 30 $ml.min^{-1}$. *Polynomial curve fit coefficients can be found in Table 7.1

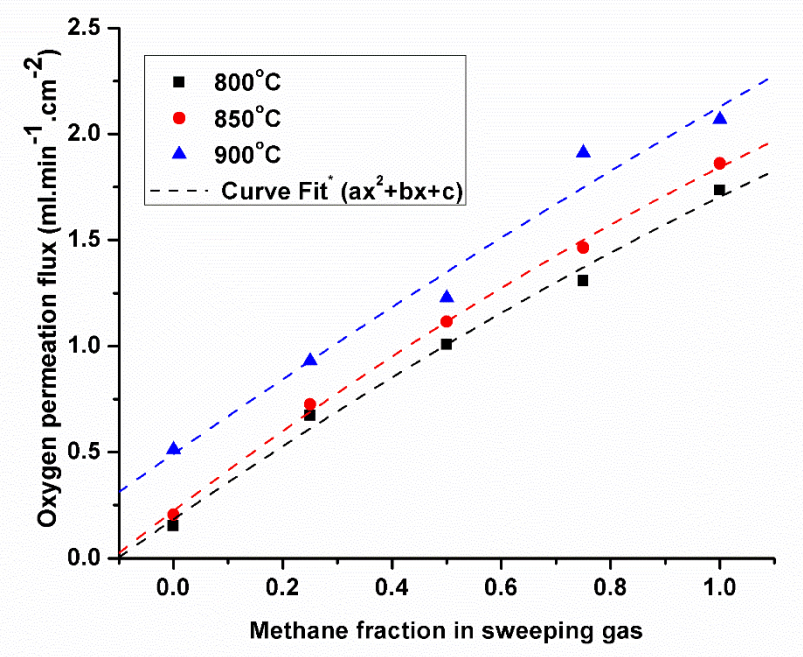

Figure C.3 Oxygen permeation flux of 30SDC-70SSC dual-phase OTM subjected to varying membrane temperatures and sweeping gas compositions with a constant total sweeping gas flow rate of 30 ml.min^{-1}. *Polynomial curve fit coefficients can be found in Table 7.1

Appendix D

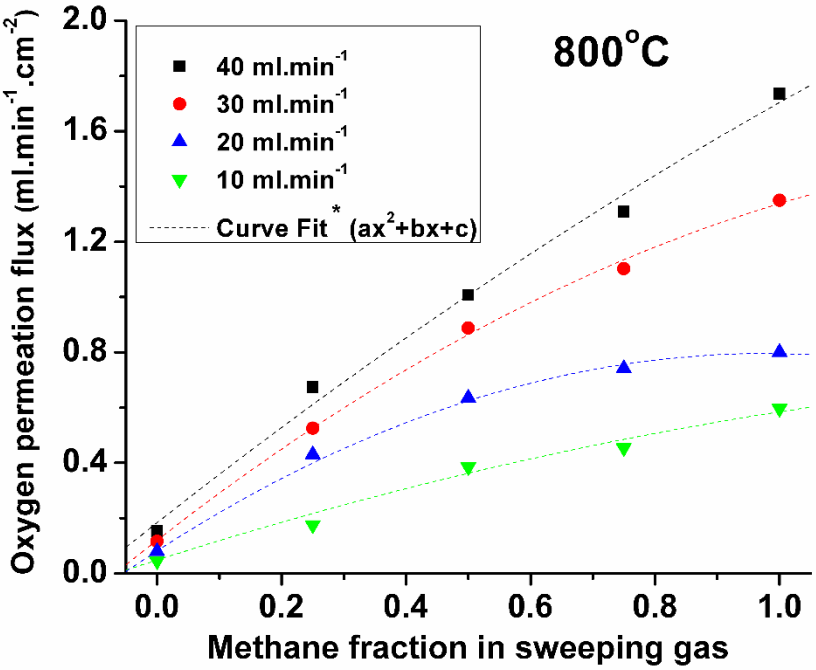

Figure D.1 Oxygen permeation flux of 30SDC-70SSC dual-phase OTM subjected to varying sweeping gas compositions and flow rates while held at a constant membrane temperature of 800°C. *Polynomial curve fit coefficients can be found in Table 7.1

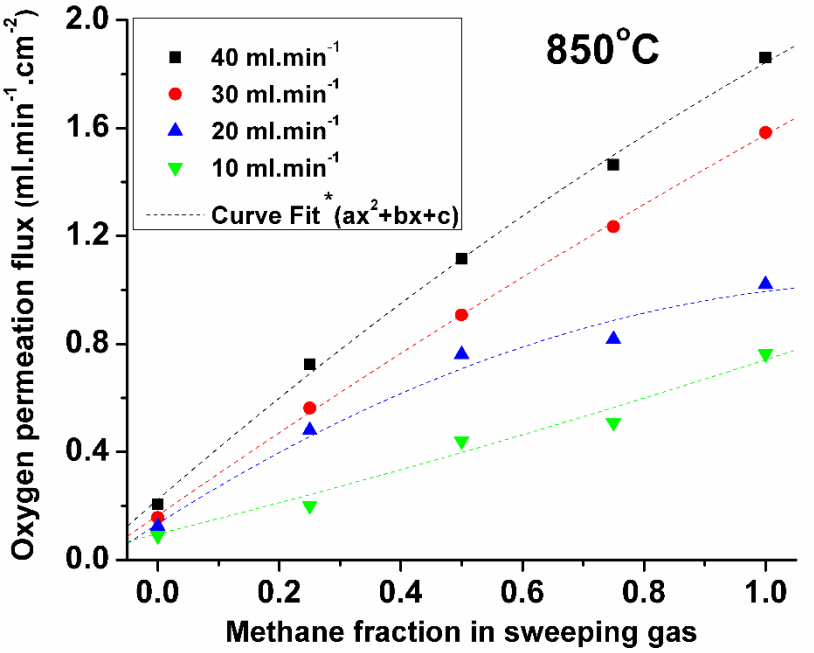

Figure D.2 Oxygen permeation flux of 30SDC-70SSC dual-phase OTM subjected to varying sweeping gas compositions and flow rates while held at a constant membrane temperature of 850°C. *Polynomial curve fit coefficients can be found in Table 7.1

Appendix E

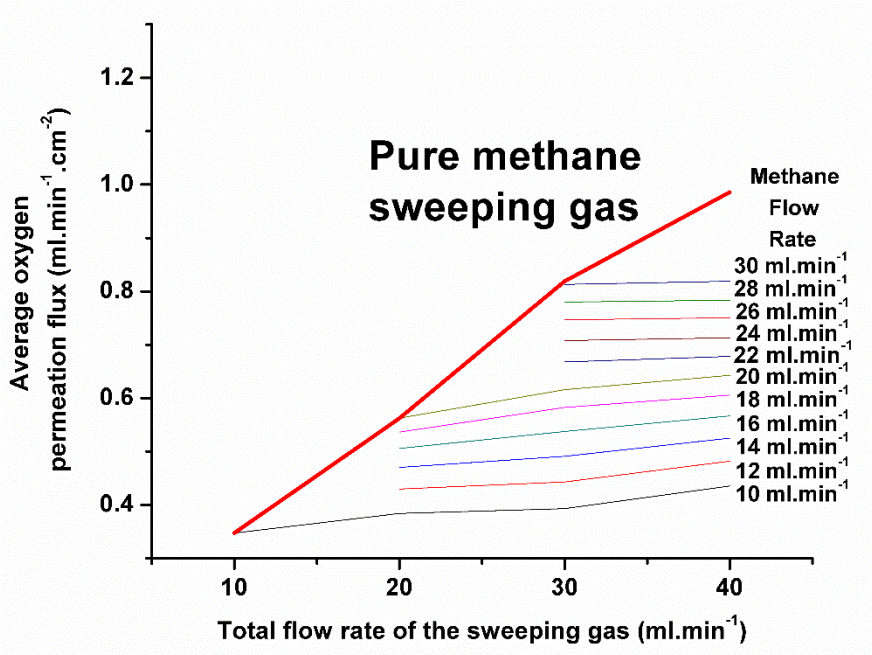

Figure E.1 Average oxygen permeation flux subjected to modified incoming methane and total sweeping gas flow rate ranging from 10 to 40 ml.min^{-1} while maintained at a membrane temperature of 800°C

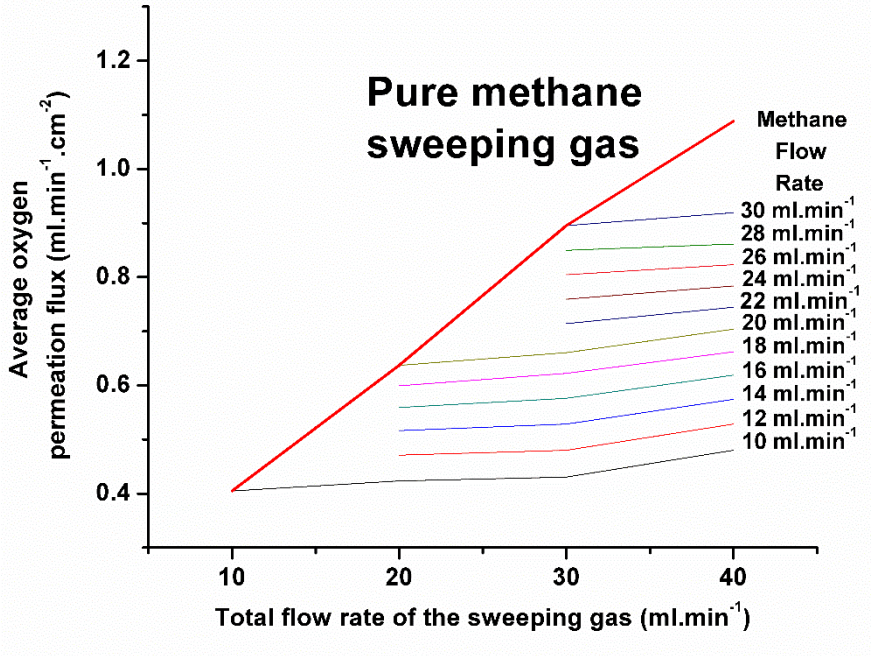

Figure E.2 Average oxygen permeation flux subjected to modified incoming methane and total sweeping gas flow rate ranging from 10 to 40 ml.min^{-1} while maintained at a membrane temperature of 850°C

Appendix F

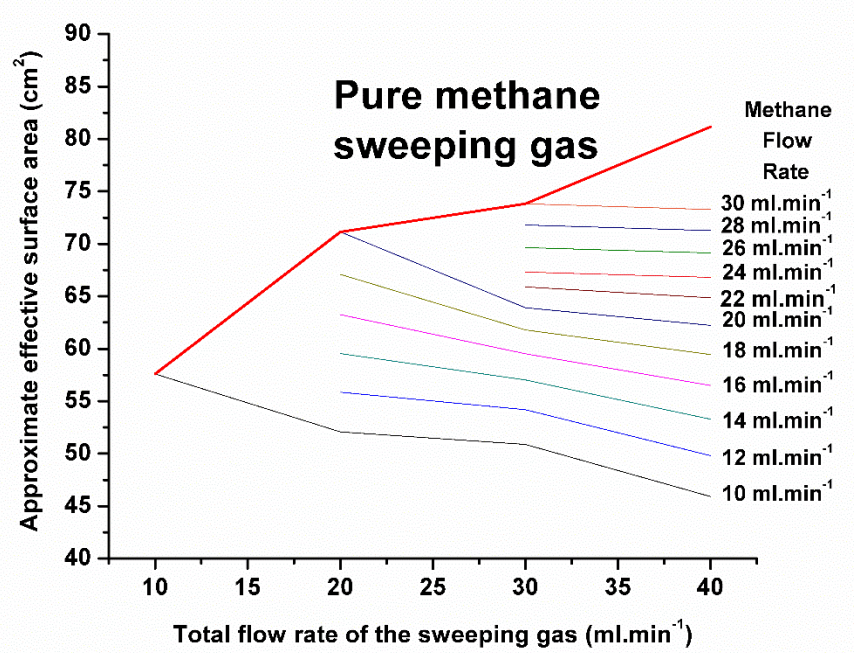

Figure F.1 AESA subjected to modified incoming methane and total sweeping gas flow rate ranging from 10 to 40 ml.min^{-1} while maintained at a membrane temperature of 800°C

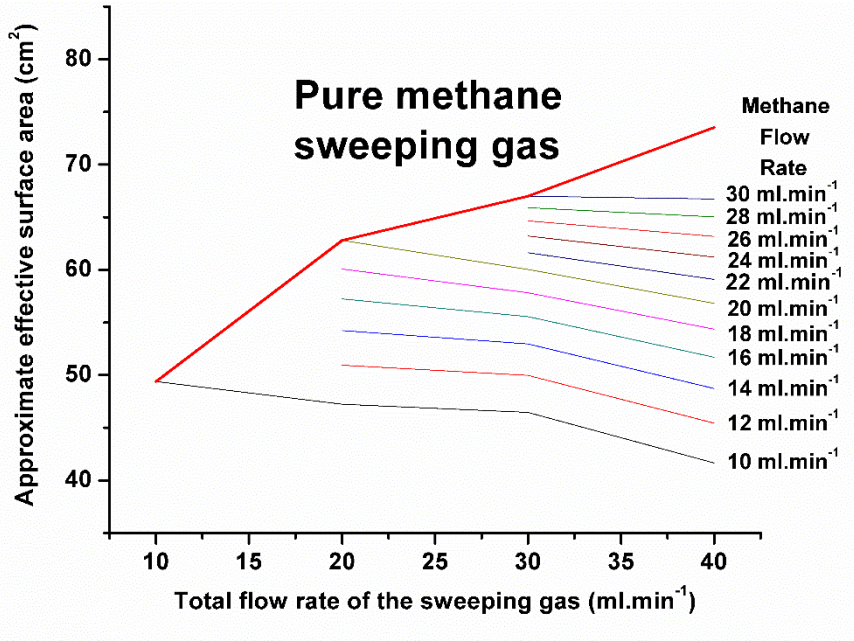

Figure F.2 AESA subjected to modified incoming methane and total sweeping gas flow rate ranging from 10 to 40 ml.min^{-1} while maintained at a membrane temperature of 850°C

References

[1] OECD/IEA, Fossil fuel energy consumption (% of total) | Data, Data.Worldbank.Org. (2017) (2014). Available from: https://data.worldbank.org/indicator/EG.USE.COMM.FO.ZS.

[2] IEA, 2015. CO_2 Emissions from fuel combustion highlights (2015 Edition). Available from: https://www.iea.org/publications/freepublications/publication/CO2EmissionsFromFuelCombustionHighlights2015.pdf

[3] C. Le Quéré, Interview with Professor Corinne Le Quéré, Carbon Management. 4 (2013) 243–248.

[4] U. Change, The Paris Agreement - main page, Unfccc.Int. (2017). Available from: http://unfccc.int/paris_agreement/items/9485.php.

[5] P. Narayan, Energy Finance: An Overview, Energy Economics. 66 (2017) 535.

[6] J.C.M. Pires, F.G. Martins, M.C.M. Alvim-Ferraz, M. Simões, Recent developments on carbon capture and storage: An overview, Chem. Eng. Res. Des. 89 (2011) 1446–1460.

[7] R.M. Cuéllar-Franca, A. Azapagic, Carbon capture, storage and utilisation technologies: A critical analysis and comparison of their life cycle environmental impacts, J. CO_2 Utilization. 9 (2015) 82–102.

[8] R. Surampalli, Carbon Capture and Storage: Physical, Chemical, and Biological Methods, ASCE, 2015.

[9] E. Blomen, C. Hendriks, F. Neele, Capture technologies: Improvements and promising developments, Energy Procedia. 1 (2009) 1505–1512.

[10] D. Mendes, A. Mendes, L.M. Madeira, A. Iulianelli, J.M. Sousa, A. Basile, The water-gas shift reaction: From conventional catalytic systems to Pd-based membrane reactors- A review, Asia-Pacific J. Chemical Engineering. 5 (2010) 111–137.

[11] K.E. Zanganeh, A. Shafeen, C. Salvador, CO_2 Capture and Development of an Advanced Pilot-Scale Cryogenic Separation and Compression Unit, Energy Procedia. 1 (2009) 247–252.

[12] A.A. Olajire, CO_2 capture and separation technologies for end-of-pipe applications - A review, Energy. 35 (2010) 2610–2628.

[13] K. Damen, M. van Troost, A. Faaij, W. Turkenburg, A comparison of electricity and hydrogen production systems with CO_2 capture and storage-Part B: Chain analysis of promising CCS options, Progress Energy and Combustion Science. 33 (2007) 576–605.

[14] K.H. Kaggerud, O. Bolland, T. Gundersen, Chemical and process integration: Synergies in co-production of power and chemicals from natural gas with CO_2 capture, Applied Thermal Engineering. 26 (2006) 1345–1352.

[15] A. Krzemień, A. Więckol-Ryk, A. Duda, A. Koteras, Risk Assessment of a Post-Combustion and Amine-Based CO_2 Capture Ready Process, J. Sustainable. Mining. 12 (2013) 18–23.

[16] H. Jin, X. Zhang, Chemical-looping combustion for power generation and carbon dioxide (CO_2) capture, Oxy-Fuel Combustion for Power Generation Carbon Dioxide Capture, 1 (2011) 294–334.

[17] T. Fujimori, T. Yamada, Realization of oxyfuel combustion for near zero emission power generation, Proceedings of the Combustion Institute. 34 (2013) 2111–2130.

[18] R. Stanger, T. Wall, R. Spörl, M. Paneru, S. Grathwohl, M. Weidmann, G. Scheffknecht, D. McDonald, K. Myöhänen, J. Ritvanen, S. Rahiala, T. Hyppänen, J. Mletzko, A. Kather, S. Santos, Oxyfuel combustion for CO_2 capture in power plants, Int. J. Greenhouse Gas Control. 40 (2015) 55–125.

[19] B.J.P. Buhre, L.K. Elliott, C.D. Sheng, R.P. Gupta, T.F. Wall, Oxy-fuel combustion technology for coal-fired power generation, Progress in Energy and Combustion Science. 31 (2005) 283–307.

[20] H.I. Mathekga, B.O. Oboirien, B.C. North, A review of oxy-fuel combustion in fluidized bed reactors, Int. J. Energy Research. 40 (2016) 878–902.

[21] K.J. Borgert, E.S. Rubin, Oxy-fuel combustion: Technical and economic considerations for the development of carbon capture from pulverized coal power plants, Energy Procedia. 37 (2013) 1291–1300.

[22] A. Leo, S. Liu, J.C.D. da Costa, Development of mixed conducting membranes for clean coal energy delivery, Int. J. Greenhouse Gas Control. 3 (2009) 357–367.

[23] R.L. Cornelissen, G.G. Hirs, Exergy Analysis of Cryogenic Air Separation, Energy Conversion and Management. 39 (1998) 1821–1826.

[24] M. Nakaiwa, T. Akiya, M. Owa, Y. Tanaka, Evaluation of an energy supply system with air separation, Energy Conversion and Management. 37 (1996) 295–301.

[25] M. Ishida, H. Jin, T. Okamoto, A fundamental study of a new kind of medium material for chemical-looping combustion, Energy and Fuels. 10 (1996) 958–963.

[26] A. Lyngfelt, B. Leckner, T. Mattisson, A fluidized-bed combustion process with inherent CO_2 separation; Application of chemical-looping combustion, Chemical Engineering Science. 56 (2001) 3101–3113.

[27] T. Mattisson, M. Johansson, A. Lyngfelt, The use of NiO as an oxygen carrier in chemical-looping combustion, Fuel. 85 (2006) 736–747.

[28] L. Zheng, Oxy-fuel combustion for power generation and carbon dioxide (CO_2) capture, Woodhead Pub., Philadelphia, PA, 2011.

[29] Y. Teraoka, H.M. Zhang, S. Furukawa, N. Yamazoe, Oxygen permeation through Perovskite-type oxides, Chemistry Letters. 14 (1985) 1743–1746.

[30] A.S. Bhalla, R. Guo, R. Roy, The perovskite structure-a review of its role in ceramic science and technology, Material Research Innovations. 4 (2000) 3–26.

[31] M.A. Peña, J.L.G. Fierro, Chemical structures and performance of perovskite oxides, Chemical Reviews. 101 (2001) 1981–2017.

[32] P. Lemes-Rachadel, G.S. Garcia, R.A.F. Machado, D. Hotza, J.C.D. da Costa, Current developments of mixed conducting membranes on porous substrates, Materials Research. 17 (2014) 242–249.

[33] K. Zhang, J. Sunarso, Z. Shao, W. Zhou, C. Sun, S. Wang, S. Liu, Research progress and materials selection guidelines on mixed conducting perovskite-type ceramic membranes for oxygen production, RSC Adv. 1 (2011) 1661-1667.

[34] U. Balachandran, J.T. Dusek, P.S. Maiya, B. Ma, R.L. Mieville, M.S. Kleefisch, C.A. Udovich, Ceramic Membrane Reactor for Converting Methane to Syngas, Catalyst Today. 36 (1997) 265–272.

[35] P.N. Dyer, R.E. Richards, S.L. Russek, D.M. Taylor, Ion transport membrane technology for oxygen separation and syngas production, Solid State Ionics. 134 (2000) 21–33.

[36] U. Balachandran, J.T. Dusek, R.L. Mieville, R.B. Poeppel, M.S. Kleefisch, S. Pei, T.P. Kobylinski, C.A. Udovich, A.C. Bose, Dense ceramic membranes for partial oxidation of methane to syngas, Applied Catalyst A: General. 133 (1995) 19–29.

[37] H.J.M. Bouwmeester, Dense ceramic membranes for methane conversion, Catalyst Today. 82 (2003) 141–150.

[38] Z. Shao, H. Dong, G. Xiong, Y. Cong, W. Yang, Performance of a mixed-conducting ceramic membrane reactor with high oxygen permeability for methane conversion, J. Membrane Science. 183 (2001) 181–192.

[39] J. Yi, M. Schroeder, T. Weirich, J. Mayer, Behavior of Ba(Co, Fe, Nb)$O_{3-\delta}$ perovskite in CO_2-containing atmospheres: Degradation mechanism and materials design, Chemistry of Materials. 22 (2010) 6246–6253.

[40] S.J. Benson, W. D., J.A. Kilner, Degradation of $La_{0.6}Sr_{0.4}Fe_{0.8}Co_{0.2}O_{3-\delta}$ in Carbon Dioxide and Water Atmospheres, J. Electrochemical Society. 146 (1999) 1305-1309.

[41] J. Yi, M. Schroeder, High temperature degradation of $Ba_{0.5}Sr_{0.5}Co_{0.8}Fe_{0.2}O_{3-\delta}$ membranes in atmospheres containing concentrated carbon dioxide, J. Membrane Science. 378 (2011) 163–170.

[42] Z. Shao, W. Yang, Y. Cong, H. Dong, J. Tong, G. Xiong, Investigation of the permeation behavior and stability of a $Ba_{0.5}Sr_{0.5}Co_{0.8}Fe_{0.2}O_{3-\delta}$ oxygen membrane, J. Membrane Science. 172 (2000) 177–188.

[43] P.Y. Zeng, Z. Shao, S. Liu, Z.P. Xu, Influence of M cations on structural, thermal and electrical properties of new oxygen selective membranes based on $SrCo_{0.95}M_{0.05}O_{3-\delta}$ perovskite, Separation and Purification Technology. 67 (2009) 304–311.

[44] P.Y. Zeng, R. Ran, Z. Chen, W. Zhou, H. Gu, Z. Shao, S. Liu, Efficient stabilization of cubic perovskite $SrCoO_{3-\delta}$ by B-site low concentration scandium doping combined with sol-gel synthesis, J. Alloys Compounds. 455 (2008) 465–470.

[45] P.Y. Zeng, K. Wang, R.L. Falkenstein-Smith, J. Ahn, Effects of sintering temperature on the performance of $SrSc_{0.1}Co_{0.9}O_{3-\delta}$ oxygen semipermeable membrane, Brazilian J. Chemical Engineering. 32 (2015) 757–765.

[46] B. Wei, Z. Lü, X. Huang, J. Miao, X. Sha, X. Xin, W. Su, Crystal structure, thermal expansion and electrical conductivity of perovskite oxides $Ba_xSr_{1-x}Co_{0.8}Fe_{0.2}O_{3-\delta}$ ($0.3 \leq x \leq 0.7$), J. European Ceramic Society. 26 (2006) 2827–2832.

[47] L. Wu, J.A. Aguiar, P.P. Dholabhai, T. Holesinger, T. Aoki, B.P. Uberuaga, R.H.R. Castro, Interface Energies of Nanocrystalline Doped Ceria: Effects of Manganese Segregation, J. Physical Chemistry C. 119 (2015) 27855–27864.

[48] J.C. Huang, Z. Mao, Z. Liu, C. Wang, Development of novel low-temperature SOFCs with co-ionic conducting SDC-carbonate composite electrolytes, Electrochemistry Communications. 9 (2007) 2601–2605.

[49] S. Cheng, M. Søgaard, L. Han, W. Zhang, M. Chen, A. Kaiser, P. V Hendriksen, A novel CO_2- and SO_2-tolerant dual phase composite membrane for oxygen separation, Chemical Communications. 51 (2015) 7140–7143.

[50] R.J. Allam, Improved oxygen production technologies, Energy Procedia. 1 (2009) 461–470.

[51] S.G. Sundkvist, A. Power, N.P. Thorshaug, N.H. Asa, Development of an Integrated Air Separation Membrane-Gas Turbine, Second Nord. Minisymp. Carbon Dioxide Capture Storage, in: Second Nordic Minisymposium On Carbon Dioxide Capture And Storage, Center for Environment and Sustainability, Chalmers, Gothenburg, 2017: pp. 52-57.

[52] S.S. Hashim, A.R. Mohamed, S. Bhatia, Oxygen separation from air using ceramic-based membrane technology for sustainable fuel production and power generation, Renewable and Sustainable Energy Reviews. 15 (2011) 1284–1293.

[53] H. Ullmann, N. Trofimenko, F. Tietz, D. Stöver, A. Ahmad-Khanlou, Correlation between thermal expansion and oxide ion transport in mixed conducting perovskite-type oxides for SOFC cathodes, Solid State Ionics. 138 (2000) 79–90.

[54] C. Wagner, Theoretical Analysis of the Diffusion Processes Determining the Oxidation Rate of Alloys, J. Electrochemical Society. 99 (1952) 369–380.

[55] C. Gazeau, E. Blond, M. Riechmann, P.M. Geffroy, A. Batakis, T. Chartier, N. Richet, Surface exchange model for ITM membrane in transient stage, J. Membrane Science. 523 (2017) 614–622.

[56] J.E. ten Elshof, H.J.M. Bouwmeester, H. Verweij, Oxidative coupling of methane in a mixed-conducting perovskite membrane reactor, Applied Catalyst A: General. 130 (1995) 195–212.

[57] F. Mauvy, J.M. Bassat, E. Boehm, P. Dordor, J.C. Grenier, J.P. Loup, Chemical oxygen diffusion coefficient measurement by conductivity relaxation-correlation between tracer diffusion coefficient and chemical diffusion coefficient, J. European Ceramic Society. 24 (2004) 1265–1269.

[58] H.J.M. Bouwmeester, A.J. Burggraaf, Chapter 10 Dense ceramic membranes for oxygen separation, Membrane Science and Technology. 4 (1996) 435–528.

[59] H.J.M. Bouwmeester, H. Kruidhof, A.J. Burggraaf, Importance of the surface exchange kinetics as rate limiting step in oxygen permeation through mixed-conducting oxides, Solid State Ionics. 72 (1994) 185–194.

[60] S.J. Xu, W.J. Thomson, Oxygen permeation rates through ion-conducting perovskite membranes, Chemical Engineering Science. 54 (1999) 3839–3850.

[61] J. Sunarso, S. Baumann, J.M. Serra, W.A. Meulenberg, S. Liu, Y.S. Lin, J.C. Diniz da Costa, Mixed ionic-electronic conducting (MIEC) ceramic-based membranes for oxygen separation, J. Membrane Science. 320 (2008) 13–41.

[62] Y. Liu, X. Tan, K. Li, Mixed conducting ceramics for catalytic membrane processing, Catalyst Reviews-Science and Engineering. 48 (2006) 145–198.

[63] K. Li, Ceramic membranes for separation and reaction, John Wiley, Chichester, England, 2007.

[64] M.H.R. Lankhorst, H.J.M. Bouwmeester, H. Verweij, Thermodynamics and Transport of Ionic and Electronic Defects in Crystalline Oxides, J. of American Ceramic Society. 80 (2005) 2175–2198.

[65] Z. Shao, G. Xiong, Y. Cong, W. Yang, Synthesis and oxygen permeation study of novel perovskite-type $BaBi_xCo_{0.2}Fe_{0.8-x}O_{3-\delta}$ ceramic membranes, J. Membrane Science. 164 (2000) 167–176.

[66] X. Zhu, H. Wang, W. Yang, Novel cobalt-free oxygen permeable membrane, Chemical Communications. 1 (2004) 1130-1131.

[67] S. Liu, G.R. Gavalas, Oxygen selective ceramic hollow fiber membranes, J. Membrane Science. 246 (2005) 103–108.

[68] J. Tong, W. Yang, R. Cai, B. Zhu, G. Xiong, L. Lin, Investigation on the structure stability and oxygen permeability of titanium-doped perovskite-type oxides of $BaTi_{0.2}Co_xFe_{0.8-x}O_{3-\delta}$ (x=0.2–0.6), Sep. Purif. Technol. 32 (2003) 289–299.

[69] Y. Teraoka, T. Nobunaga, N. Yamazoe, Effect of Cation Substitution on the Oxygen Semipermeability of Perovskite-type Oxides, Chemistry Letters. 17 (1988) 503–506.

[70] J.E. ten Elshof, H.J.M. Bouwmeester, H. Verweij, Oxygen transport through $La_{1-x}Sr_xFeO_{3-\delta}$ membranes II. Permeation in air/CO, CO_2 gradients, Solid State Ionics. 89 (1996) 81–92.

[71] C.Y. Tsai, A.G. Dixon, Y.H. Ma, W.R. Moser, M.R. Pascuccie, Dense Perovskite, $La_{1-x}A_xFe_{1-y}Co_yO_{3-\delta}$ (A=Ba, Sr, Ca), Membrane Synthesis, Applications, and Characterization, J. American Ceramic Society. 81 (1998) 1437–1444.

[72] N. Miura, Y. Okamoto, J. Tamaki, K. Morinaga, N. Yamazoe, Oxygen semipermeability of mixed-conductive oxide thick-film prepared by slip casting, Solid State Ionics. 79 (1995) 195–200.

[73] H. Kruidhof, H.J.M.M. Bouwmeester, R.H.E.E. v. Doorn, A.J. Burggraaf, Influence of order-disorder transitions on oxygen permeability through selected nonstoichiometric perovskite-type oxides, Solid State Ionics. 63–65 (1993) 816–822.

[74] K. Li, X. Tan, Y. Liu, Single-step fabrication of ceramic hollow fibers for oxygen permeation, J. Membrane Science. 272 (2006) 1–5.

[75] T. Ishihara, T. Yamada, H. Arikawa, H. Nishiguchi, Y. Takita, Mixed electronic–oxide ionic conductivity and oxygen permeating property of Fe-, Co-or Ni-doped LaGaO perovskite oxide, Solid State Ionics. 135 (2000) 631–636.

[76] L. Siwen, C. You, F. Lianqing, Y. Weishen, L. Liwu, M. Jian, R. Yufang, Oxygen Permeating Properties of the Mixed Conducting Membranes without Cobalt, Material Research Bulletin. 33 (1998) 183–188.

[77] L. Qiu, T.H. Lee, L.M. Liu, Y.L. Yang, A.J. Jacobson, Oxygen permeation studies of $SrCo_{0.8}Fe_{0.2}O_{3-\delta}$, Solid State Ionics. 76 (1995) 321–329.

[78] P.Y. Zeng, R. Ran, Z. Chen, H. Gu, Z. Shao, J.C.D. da Costa, S. Liu, Significant effects of sintering temperature on the performance of $La_{0.6}Sr_{0.4}Co_{0.2}Fe_{0.8}O_{3-\delta}$ oxygen selective membranes, J. Membrane Science. 302 (2007) 171–179.

[79] H. Wang, C. Tablet, A. Feldhoff, J. Caro, Investigation of phase structure, sintering, and permeability of perovskite-type $Ba_{0.5}Sr_{0.5}Co_{0.8}Fe_{0.2}O_{3-\delta}$ membranes, J. Membrane Science. 262 (2005) 20–26.

[80] M. Simioni, S.E. Kentish, G.W. Stevens, Membrane stripping: Desorption of carbon dioxide from alkali solvents, J. Membrane Science. 378 (2011) 18–27.

[81] O. Czuprat, M. Arnold, S. Schirrmeister, T. Schiestel, J. Caro, Influence of CO_2 on the oxygen permeation performance of perovskite-type $BaCo_xFe_yZr_zO_{3-\delta}$ hollow fiber membranes, J. Membrane Science. 364 (2010) 132–137.

[82] W. Chen, A. Nijmeijer, L. Winnubst, Oxygen non-stoichiometry determination of perovskite materials by a carbonation process, Solid State Ionics. 229 (2012) 54–58.

[83] M. Arnold, H. Wang, A. Feldhoff, Influence of CO_2 on the oxygen permeation performance and the microstructure of perovskite-type $(Ba_{0.5}Sr_{0.5})(Co_{0.8}Fe_{0.2})O_{3-\delta}$ membranes, J. Membrane Science. 293 (2007) 44–52.

[84] M. Balaguer, J. García-Fayos, C. Solís, J.M. Serra, Fast Oxygen Separation Through SO_2- and CO_2-Stable Dual-Phase Membrane Based on $NiFe_2O_4$ –$Ce_{0.8}Tb_{0.2}O_{2-\delta}$, Chemistry of Materials. 25 (2013) 4986–4993.

[85] X. Dong, G. Zhang, Z. Liu, Z. Zhong, W. Jin, N. Xu, CO_2-tolerant mixed conducting oxide for catalytic membrane reactor, J. Membrane Science. 340 (2009) 141–147.

[86] L. Gui, Y. Wan, R. Wang, Z. Wang, B. He, L. Zhao, A comparison of oxygen permeation and CO_2 tolerance of $La_{0.6}Sr_{0.4}Co_{0.2}Fe_{0.6}Nb_{0.2}O_{3-\delta}$ and $La_{0.6}Sr_{0.4}Fe_{0.8}Nb_{0.2}O_{3-\delta}$ ceramic membranes, J. Alloys and Compounds. 644 (2015) 788–792.

[87] T. Klande, O. Ravkina, A. Feldhoff, Effect of A-site lanthanum doping on the CO_2 tolerance of $SrCo_{0.8}Fe_{0.2}O_{3-\delta}$ oxygen-transporting membranes, J. Membrane Science. 437 (2013) 122–130.

[88] K. Partovi, F. Liang, O. Ravkina, J.J. Caro, High-flux oxygen-transporting membrane $Pr_{0.6}Sr_{0.4}Co_{0.5}Fe_{0.5}O_{3-\delta}$: CO_2 stability and microstructure, ACS Applied Materials and Interfaces. 6 (2014) 10274–10282.

[89] M. Schulz, R. Kriegel, A. Kämpfer, Assessment of CO_2 stability and oxygen flux of oxygen permeable membranes, J. Membrane Science. 378 (2011) 10–17.

[90] X. Tan, N. Liu, B. Meng, J. Sunarso, K. Zhang, S. Liu, Oxygen permeation behavior of $La_{0.6}Sr_{0.4}Co_{0.8}Fe_{0.2}O_{3-\delta}$ hollow fibre membranes with highly concentrated CO_2 exposure, J. Membrane Science. 389 (2012) 216–222.

[91] J. Yi, M. Schroeder, M. Martin, CO_2-Tolerant and Cobalt-Free $SrFe_{0.8}Nb_{0.2}O_{3-\delta}$ Perovskite Membrane for Oxygen Separation, Chemistry of Materials. 25 (2013) 815–817.

[92] J. Yi, T.E. Weirich, M. Schroeder, CO_2 corrosion and recovery of perovskite-type $BaCo_{1-x-y}Fe_xNb_yO_{3-\delta}$ membranes, J. Membrane Science. 437 (2013) 49–56.

[93] Q. Zeng, Y. bo Zuo, C. gang Fan, C. sheng Chen, CO_2-tolerant oxygen separation membranes targeting CO_2 capture application, J. Membrane Science. 335 (2009) 140–144.

[94] Y. Zhang, G.M. Yang, G. Chen, R. Ran, W. Zhou, Z.P. Shao, Evaluation of the CO_2 Poisoning Effect on a Highly Active Cathode $SrSc_{0.175}Nb_{0.025}Co_{0.8}O_{3-\delta}$ in the Oxygen Reduction Reaction, ACS Applied Materials and Interfaces. 8 (2016) 3003–3011.

[95] J. Zhu, S. Guo, Z. Zhang, X. Jiang, Z. Liu, W. Jin, CO_2-tolerant mixed-conducting multichannel hollow fiber membrane for efficient oxygen separation, J. Membrane Science. 485 (2015) 79–86.

[96] Z. Zhang, D. Chen, F. Dong, Z. Shao, Efficient and CO_2-tolerant oxygen transport membranes prepared from high-valence B-site substituted cobalt-free $SrFeO_{3-\delta}$, J. Membrane Science. 495 (2015) 187–197.

[97] J. Martynczuk, K. Efimov, L. Robben, A. Feldhoff, Performance of zinc-doped perovskite-type membranes at intermediate temperatures for long-term oxygen permeation and under a carbon dioxide atmosphere, J. Membrane Science. 344 (2009) 62–70.

[98] W. Li, J.J. Liu, C.S. Chen, Hollow fiber membrane of yttrium-stabilized zirconia and strontium-doped lanthanum manganite dual-phase composite for oxygen separation, J. Membrane Science. 340 (2009) 266–271.

[99] H. Luo, T. Klande, Z. Cao, F. Liang, H. Wang, J. Caro, A CO_2-stable reduction-tolerant Nd-containing dual phase membrane for oxyfuel CO_2 capture, J. Material Chemistry A. 2 (2014) 7780–7787.

[100] H. Luo, K. Efimov, H. Jiang, A. Feldhoff, H. Wang, J. Caro, CO_2-stable and cobalt-free dual-phase membrane for oxygen separation, Angew. Chemie - Int. Ed. 50 (2011) 759–763.

[101] K.S. Yun, J.H. Park, Y. Kwon, D.Y. Kim, C.-Y. Yoo, J.H. Yu, J.H. Joo, A new strategy for enhancing the thermo-mechanical and chemical stability of dual-phase mixed ionic electronic conductor oxygen membranes, J. Material Chemistry A. 4 (2016) 13549–13554.

[102] H. Luo, H. Jiang, T. Klande, Z. Cao, Novel Cobalt-Free, Noble Metal-Free Oxygen-Permeable $40Pr_{0.6}Sr_{0.4}FeO_{3-\delta}$–$60Ce_{0.9}Pr_{0.1}O_{2-\delta}$ Dual-Phase Membrane, Chemistry of Materials. 24 (2012) 2148–2154.

[103] H. Luo, H. Jiang, K. Efimov, H. Wang, Influence of the Preparation Methods on the Microstructure and Oxygen Permeability of a CO_2-Stable Dual Phase Membrane, American. Inst. of Chemical Engineers. 57 (2011) 2738–2745.

[104] J. Xue, Q. Liao, Y. Wei, Z. Li, H. Wang, A CO_2-tolerance oxygen permeable $60Ce_{0.9}Gd_{0.1}O_{2-\delta}$-$40Ba_{0.5}Sr_{0.5}Co_{0.8}Fe_{0.2}O_{3-\delta}$ dual phase membrane, J. Membrane Science. 443 (2013) 124–130.

[105] P. Wang, H. Cheng, Y. Wang, X. Lu, Investigation of Co–doped $Ce_{0.8}Sm_{0.2}O_{2-\delta}$–$Ba_{0.95}La_{0.05}Zr_{0.1}Fe_{0.9-x}Co_xO_{3-\delta}$ Dual–phase Oxygen Transport Membranes, in: Symposium On Materials Application And Engineering 2016, EDP Sciences, Chiang Mai, Thailand, 2016: pp. 8-13.

[106] F. Liang, H. Luo, K. Partovi, O. Ravkina, Z. Cao, Y. Liu, J. Caro, A novel CO_2-stable dual phase membrane with high oxygen permeability, Chemical Communications. 50 (2014) 2451–2454.

[107] X. Zhu, Y. Liu, Y. Cong, W. Yang, $Ce_{0.85}Sm_{0.15}O_{1.925}$-$Sm_{0.6}Sr_{0.4}Al_{0.3}Fe_{0.7}O_{3-\delta}$ dual-phase membranes: One-pot synthesis and stability in a CO_2 atmosphere, Solid State Ionics. 253 (2013) 57–63.

[108] J. Xue, Q. Zheng, Y. Wei, K. Yuan, Z. Li, H. Wang, Dual Phase Composite Oxide of $Ce_{0.9}Gd_{0.1}O_{2-\delta}$-$Ba_{0.5}Sr_{0.5}Co_{0.8}Fe_{0.2}O_{3-\delta}$ with Excellent Oxygen Permeation, Industrial and Engineering Chemistry Research. 51 (2012) 4703-4709.

[109] T. Liu, W. He, H. Huang, S. Wang, H.J.M. Bouwmeester, C. Chen, $Ce_{0.8}Sm_{0.2}O_{1.9}$-$La_{0.8}Sr_{0.2}Cr_{0.5}Fe_{0.5}O_{3-\delta}$ dual-phase hollow fiber membranes operated under different gradients, Industrial and Engineering Chemistry Research. 53 (2014) 6131–6136.

[110] Z. Wang, W. Sun, Z. Zhu, T. Liu, W. Liu, A Novel Cobalt-Free, CO_2-Stable, and Reduction-Tolerant Dual-Phase Oxygen-Permeable Membrane, Applied Materials and Interfaces. 5 (2013) 11038-11043.

[111] H. Luo, H. Jiang, K. Efimov, F. Liang, H. Wang, J. Caro, CO_2-Tolerant Oxygen-Permeable Fe_2O_3-$Ce_{0.9}Gd_{0.1}O_{2-\delta}$ Dual Phase Membranes, Industrial and Engineering Chemistry Research. 50 (2011) 13508–13517.

[112] H. Cheng, L. Luo, W. Yao, X. Lu, X. Zou, Z. Zhou, Novel cobalt-free CO_2-tolerant dual-phase membranes of $Ce_{0.8}Sm_{0.2}O_{2-\delta}$-$Ba_{0.95}La_{0.05}Fe_{1-x}Zr_xO_{3-\delta}$ for oxygen separation, J. Membrane Science. 492 (2015) 220–229.

[113] C. Fu, K. Sun, N. Zhang, X. Chen, D. Zhou, Electrochemical characteristics of LSCF-SDC composite cathode for intermediate temperature SOFC, Electrochim. Acta. 52 (2007) 4589–4594.

[114] Q. Xu, D. ping Huang, F. Zhang, W. Chen, M. Chen, H. xing Liu, Structure, electrical conducting and thermal expansion properties of $La_{0.6}Sr_{0.4}Co_{0.8}Fe_{0.2}O_{3-\delta}$-$Ce_{0.8}Sm_{0.2}O_{2-\delta}$ composite cathodes, J. Alloys and Compounds. 454 (2008) 460–465.

[115] Air Products and Chemicals, Inc., Ion transport membrane module and vessel system with directed internal gas flow, EP 1676811 A3, 2009.

[116] S.M. Kelly, Praxair's Oxygen Transport Membranes for Oxycombustion and Syngas Applications, (2014) 1–16. Available from: https://www.netl.doe.gov/File Library/Events/2014/2014 NETL CO_2 Capture/S-Kelly-PRAXAIR-Praxair-s-Oxygen-Transport-Membranes.pdf.

[117] S. Diethelm, J. Van herle, P.H. Middleton, D. Favrat, Oxygen permeation and stability of $La_{0.4}Ca_{0.6}Fe_{1-x}Co_xO_{3-\delta}$ (x = 0, 0.25, 0.5) membranes, J. Power Sources. 1-2 (2003) 270–275.

[118] M.A. Nemitallah, M.A. Habib, R. Ben Mansour, Investigations of oxy-fuel combustion and oxygen permeation in an ITM reactor using a two-step oxy-combustion reaction kinetics model, J. Membrane Science. 432 (2013) 1–12.

[119] J. Tonziello, M. Vellini, Oxygen production technologies for IGCC power plants with CO_2 capture, Energy Procedia. 4 (2011) 637–644.

[120] L. Rosen, N. Degenstein, M. Shah, J. Wilson, S. Kelly, J. Peck, M. Christie, Energy Procedia Development of Oxygen Transport Membranes for Coal-Based Power Generation, Energy Procedia. 4 (2011) 750–755.

[121] M.A. Nemitallah, M.A. Habib, K. Mezghani, Experimental and numerical study of oxygen separation and oxy-combustion characteristics inside a button-cell LNO-ITM reactor, Energy. 84 (2015) 600–611.

[122] M.A. Nemitallah, M.A. Habib, R. Ben-mansour, A.F. Ghoniem, Design of an ion transport membrane reactor for gas turbine combustion application, J. Membrane Science. 450 (2014) 60–71.

[123] M.A. Habib, M.A. Nemitallah, Design of an ion transport membrane reactor for application in fire tube boilers, Energy. 81 (2015) 787–801.

[124] M.A. Habib, S.A. Salaudeen, M.A. Nemitallah, R. Ben-Mansour, E.M.A. Mokheimer, Numerical investigation of syngas oxy-combustion inside a LSCF-6428 oxygen transport membrane reactor, Energy. 96 (2016) 654–665.

[125] S. Fuyuki, Effects of doped acceptor ions on proton diffusion in perovskite oxides: a first-principles molecular- dynamics simulation, J. Physics: Condensed Matter. 10 (1998) 285-294.

[126] M. Fronzi, Y. Tateyama, N. Marzari, M. Nolan, E. Traversa, First-principles molecular dynamics simulations of proton diffusion in cubic $BaZrO_3$ perovskite under strain conditions, Materials for Renewable and Sustainable Energy. 5 (2016) 13-23.

[127] T. Wu, Q. Wang, T. Yao, S. He, Molecular dynamics simulations of the structural properties of Al_2O_3-based binary systems, J. Non-Crystalline Solids. 435 (2016) 17–26.

[128] D. Bai, J. Sun, W. Chen, D. Du, Molecular dynamics simulation of the diffusion behavior between Co and Ti and its effect on the wear of WC/Co tools when titanium alloy is machined, Ceramics International. 42 (2016) 17754–17763.

[129] C. Kong, Q. Yao, D. Yu, S. Li, Ionic self-diffusion of Al cations and O anions in the vitreous Al_2O_3 with molecular dynamics simulations, J. Non-Crystalline Solids. 430 (2015) 31–37.

[130] P.Y. Zeng, R. Ran, Z.H. Chen, H.X. Gu, Z.P. Shao, S.M. Liu, Novel mixed conducting $SrSc_{0.05}Co_{0.95}Co_{0.95}O_{3-\delta}$ ceramic membrane for oxygen separation, American. Inst. of Chemical Engineers. 53 (2007) 3116–3124.

[131] P.Y. Zeng, Z. Chen, W. Zhou, H. Gu, Z. Shao, S. Liu, Re-evaluation of $Ba_{0.5}Sr_{0.5}Co_{0.8}Fe_{0.2}O_{3-\delta}$ perovskite as oxygen semi-permeable membrane, J. Membrane Science. 291 (2007) 148–156.

[132] S. Gopalan, A. V. Virkar, Interdiffusion and Kirkendall Effect in Doped $BaTiO_3$-$BaZrO_3$ Perovskites: Effect of Vacancy Supersaturation, J. American Ceramics Society. 82 (2004) 2887–2899.

[133] S. Tokita, H. Kokawa, Y.S. Sato, H.T. Fujii, In situ EBSD observation of grain boundary character distribution evolution during thermomechanical process used for grain boundary engineering of 304 austenitic stainless steel, Materials Characterization. 131 (2017) 31–38.

[134] J.C. Huang, I.C. Hsiao, T.D. Wang, B.Y. Lou, EBSD study on grain boundary characteristics in fine-grained Al alloys, Scr. Mater. 43 (2000) 213–220.

[135] W. Sitte, E. Bucher, A. Benisek, W. Preis, Oxygen nonstoichiometry and ionic transport properties of $La_{0.4}Sr_{0.6}CoO_{3-\delta}$, Spectrochim. Acta. A. Mol. Biomol. Spectrosc. 57 (2001) 2071–2076.

[136] I. Yasuda, Precise Determination of the Chemical Diffusion Coefficient of Calcium-Doped Lanthanum Chromites by Means of Electrical Conductivity Relaxation, J. Electrochemical Society. 141 (1994) 1268-1273.

[137] I. Yasuda, M. Hishinuma, Electrical conductivity and chemical diffusion coefficient of Sr-doped lanthanum chromites, Solid State Ionics. 80 (1995) 141–150.

[138] F. Ciucci, Electrical conductivity relaxation measurements: Statistical investigations using sensitivity analysis, optimal experimental design and ECRTOOLS, Solid State Ionics. 239 (2013) 28–40.

[139] P.Y. Zeng, CO_2 Separation, Ph.D., Syracuse University, 2013.

[140] D. Frenkel, B. Smit, Understanding molecular simulation: from algorithms to applications, Phys. Today. 50 (2002) 638.

[141] R.A. Buckingham, The Classical Equation of State of Gaseous Helium, Neon and Argon, Proc. R. Soc. A Math. Phys. Eng. Sci. 168 (1938) 264–283.

[142] S. Plimpton, Fast Parallel Algorithms for Short-Range Molecular Dynamics, J. Computational Physics. 117 (1995) 1–19.

[143] S. Plimpton, LAMMPS-large-scale atomic/molecular massively parallel simulator, Sandia Natl. Lab. (2007).

[144] G. V Lewis, C.R.A. Catlow, Potential models for ionic oxides, J. Phys. C Solid State Physics. 18 (1985) 1149–1161.

[145] M. Cherry, M.S. Islam, C.R.A. Catlow, Oxygen Ion Migration in Perovskite-Type Oxides, J. Solid State Chem. 118 (1995) 125-132.

[146] L. Minervini, M.O. Zacate, R.W. Grimes, Defect cluster formation in M_2O_3-doped CeO_2, Solid State Ionics. 116 (1999) 339–349.

[147] R.E. Smallman, A.H.W. Ngan, Surfaces, Grain Boundaries and Interfaces, Modern Physical Metallurgy. 1 (2014) 415–442.

[148] T. Hong, L. Zhang, F. Chen, C. Xia, Oxygen surface exchange properties of $La_{0.6}Sr_{0.4}Co_{0.8}Fe_{0.2}O_{3-\delta}$ coated with $Sm_xCe_{1-x}O_{2-\delta}$, J. Power Sources. 218 (2012) 254–260.

[149] F. He, X. Jin, T. Tian, H. Ding, R.D. Green, X. Xue, Determination of Electrochemical Kinetic Property for Mixed Ionic Electronic Conductors from Electrical Conductivity Relaxation Measurements, J. Electrochemical Society. 162 (2015) F951–F958.

[150] F. Landuzzi, L. Pasquini, S. Giusepponi, M. Celino, A. Montone, P.L. Palla, F. Cleri, Molecular dynamics of ionic self-diffusion at an MgO grain boundary, J. Material Science. 50 (2015) 2502–2509.

[151] P. Heitjans, S. Indris, Diffusion and ionic conduction in nanocrystalline ceramics, J. Phys. Condensed Matter. 15 (2003) R1257–R1289.

[152] A. Suzuki, Y. Mishin, Atomic mechanisms of grain boundary diffusion: Low versus high temperatures, J. Material Science. 40 (2005) 3155–3161.

[153] K.J. Borgert, E.S. Rubin, Oxy-combustion Carbon Capture for Pulverized Coal in the Integrated Environmental Control Model, Energy Procedia. 114 (2017) 522–529.

[154] S. Upasen, P. Batocchi, F. Mauvy, A. Slodczyk, P. Colomban, Chemical and structural stability of $La_{0.6}Sr_{0.4}Co_{0.2}Fe_{0.8}O_{3-\delta}$ ceramic vs. medium/high water vapor pressure, Ceramics Internation. 41 (2015) 14137–14147.

[155] Y. Kimura, T. Kushi, S. Hashimoto, K. Amezawa, T. Kawada, Influences of Temperature and Oxygen Partial Pressure on Mechanical Properties of $La_{0.6}Sr_{0.4}Co_{1-y}Fe_yO_{3-\delta}$, J. American Ceramic Society. 95 (2012) 2608–2613.

[156] F. Wang, K. Yamaji, D.-H. Cho, T. Shimonosono, H. Kishimoto, M.E. Brito, T. Horita, H. Yokokawa, Sulfur Poisoning on $La_{0.6}Sr_{0.4}Co_{0.2}Fe_{0.8}O_{3-\delta}$ Cathode for SOFCs, J. Electrochemical Society. 158 (2011) B1391-B1397.

[157] Z. Liu, M.F. Han, W.T. Miao, Preparation and characterization of graded cathode $La_{0.6}Sr_{0.4}Co_{0.2}Fe_{0.8}O_{3-\delta}$, J. Power Sources. 173 (2007) 837–841.

[158] J.W. Stevenson, T.R. Armstrong, R.D. Carneim, L.R. Pederson, W.J. Weber, Electrochemical properties of mixed conducting perovskites $La_{1-x}M_xCo_{1-y}Fe_yO_{3-\delta}$ (M = Sr, Ba, Ca), J. Electrochemical Society. 143 (1996) 2722–2729.

[159] S.S. Hashim, S. Bhatia, A.R. Mohamed, Parameter optimization for sintering of $La_{0.6}Sr_{0.4}Co_{0.2}Fe_{0.8}O_{3-\delta}$ (LSCF6428) perovskite-structured ceramics by Taguchi method, Science of Sintering. 48 (2016) 177–189.

[160] J.S. Hardy, J.W. Templeton, D.J. Edwards, Z. Lu, J.W. Stevenson, Lattice expansion of LSCF-6428 cathodes measured by in situ XRD during SOFC operation, J. Power Sources. 198 (2012) 76–82.

[161] S.J. Xu, W.J. Thomson, Stability of $La_{0.6}Sr_{0.4}Co_{0.2}Fe_{0.8}O_{3-\delta}$ Perovskite Membranes in Reducing and Nonreducing Environments, Industrial and Engineering Chemistry Research. 37 (1998) 1290-1299.

[162] H.T. Lim, S.C. Hwang, Y.M. Park, S. Lee, Performance and long term stability of large area anode supported solid oxide fuel cells (SOFCs), Solid State Ionics. 225 (2012) 124–130.

[163] Cathode Powders and Composite Cathode Powders for SOFCs, Fuelcellmaterials. (2017). https://fuelcellmaterials.com/products/powders/cathode-powders/

[164] Q. Zheng, J. Xue, Q. Liao, Y. Wei, Z. Li, H. Wang, CO_2-tolerant alkaline-earth metal-free single phase membrane for oxygen separation, Chemical Engineering Science. 101 (2013) 240–247.

[165] K. Partovi, B. Geppert, F. Liang, C.H. Rüscher, J. Caro, Effect of the B-Site Composition on the Oxygen Permeability and the CO_2 Stability of $Pr_{0.6}Sr_{0.4}Co_xFe_{1-x}O_{3-\delta}$ ($0.0 \leq x \leq 1.0$) Membranes, Chemistry of Materials. 27 (2015) 2911–2919.

[166] J.W. Zhu, S.B. Guo, Z.Y. Chu, W.Q. Jin, CO_2-tolerant oxygen-permeable perovskite-type membranes with high permeability, J. Material Chemistry A. 3 (2015) 22564–22573.

[167] Samarium Doped Ceria Premium Electrolyte Powder, Fuelcellmaterials. (2017). https://fuelcellmaterials.com/products/powders/premium-powders/samarium-doped-ceria-20-sm-premium-powder/

[168] M. Burriel, C. Niedrig, W. Menesklou, S.F. Wagner, J. Santiso, E. Ivers-Tiffée, BSCF epitaxial thin films: Electrical transport and oxygen surface exchange, Solid State Ionics. 181 (2010) 602–608.

[169] Z. Yáng, A.S. Harvey, A. Infortuna, J. Schoonman, L.J. Gauckler, Electrical conductivity and defect chemistry of $Ba_xSr_{1-x}Co_yFe_{1-y}O_{3-\delta}$ perovskites, J. Solid State Electrochemistry. 15 (2011) 277–284.

[170] N. Bauer, I. Mouratiadou, G. Luderer, L. Baumstark, R.J. Brecha, O. Edenhofer, E. Kriegler, Global fossil energy markets and climate change mitigation- an analysis with REMIND, Clim. Change. 136 (2016) 69–82.

[171] W. Chen, C. Chen, H.J.M. Bouwmeester, A. Nijmeijer, L. Winnubst, Oxygen-selective membranes integrated with oxy-fuel combustion, J. Membrane Science. 463 (2014) 166–172.

[172] S. Engels, T. Markus, M. Modigell, L. Singheiser, Oxygen permeation and stability investigations on MIEC membrane materials under operating conditions for power plant processes, J. Membrane Science. 370 (2011) 58–69.

[173] J. Tong, W. Yang, B. Zhu, R. Cai, Investigation of ideal zirconium-doped perovskite-type ceramic membrane materials for oxygen separation, J. Membrane Science. 203 (2002) 175–189.

[174] R. Falkenstein-Smith, P. Zeng, J. Ahn, Investigation of oxygen transport membrane reactors for oxy-fuel combustion and carbon capture purposes, Proc. Combustion Institute. 36 (2017) 3969–3976.

[175] B. Wei, Z. Lü, X. Huang, M. Liu, N. Li, W. Su, Synthesis, electrical and electrochemical properties of $Ba_{0.5}Sr_{0.5}Zn_{0.2}Fe_{0.8}O_{3-\delta}$ perovskite oxide for IT-SOFC cathode, J. Power Sources. 176 (2008) 1–8.

[176] L. Wang, R. Dou, M. Bai, Y. Li, D. Hall, Y. Chen, Characterisation of microstructure and hardness of perovskite-structured $Ba_{0.5}Sr_{0.5}Co_{0.8}Fe_{0.2}O_{3-\delta}$ under different sintering conditions, J. European Ceramics Society. 36 (2016) 1659–1667.

[177] L. da Conceição, A.M. Silva, N.F. Ribeiro, M.M.V.M. Souza, Combustion synthesis of $La_{0.7}Sr_{0.3}Co_{0.5}Fe_{0.5}O_{3-\delta}$ (LSCF) porous materials for application as cathode in IT-SOFC, Material Research Bulletin. 46 (2011) 308–314.

[178] H. Li, X. Zhu, Y. Liu, W. Wang, W. Yang, Comparative investigation of dual-phase membranes containing cobalt and iron-based mixed conducting perovskite for oxygen permeation, J. Membrane Science. 462 (2014) 170–177.

[179] H. Li, Y. Liu, X. Zhu, Y. Cong, S. Xu, W. Xu, W. Yang, Oxygen permeation through Ca-contained dual-phase membranes for oxyfuel CO_2 capture, Separation and Purification Technology. 114 (2013) 31–37.

[180] H. Yoshida, K. Miura, J.-I. Fujita, T. Inagaki, Effect of Gallia Addition on the Sintering Behavior of Samaria-Doped Ceria, J. American Ceramics Society. 82 (1999) 219–221.

[181] X. Tan, K. Li, Modeling of air separation in a LSCF hollow-fiber membrane module, American. Inst. of Chemical Engineers. 48 (2002) 1469–1477.

[182] H. Wang, R. Wang, D.T. Liang, W. Yang, Experimental and modeling studies on $Ba_{0.5}Sr_{0.5}Co_{0.8}Fe_{0.2}O_{3-\delta}$ (BSCF) tubular membranes for air separation, J. Membrane Science. 243 (2004) 405–415.

[183] S.G. Sundkvist, S. Julsrud, B. Vigeland, T. Naas, M. Budd, H. Leistner, D. Winkler, Development and testing of AZEP reactor components, Int. J. Greenhouse Gas Control. 1 (2007) 180–187.

[184] V. Randle, The coincidence site lattice and the “sigma enigma,” Material Characterization. 47 (2001) 411–416.

[185] A. Gupta, G.Q. Gong, G. Xiao, P.R. Duncombe, P. Lecoeur, P. Trouilloud, Y.Y. Wang, V.P. Dravid, J.Z. Sun, Grain-boundary effects on the magnetoresistance properties of perovskite manganite films, Physics Review B. 54 (1996) R15629–R15632.

[186] H. Hojo, T. Mizoguchi, H. Ohta, S.D. Findlay, N. Shibata, T. Yamamoto, Y. Ikuhara, Atomic structure of a CeO_2 grain boundary: The role of oxygen vacancies, Nano Letters. 10 (2010) 4668–4672.

[187] D.M. Hwang, T.S. Ravi, R. Ramesh, S.W. Chan, C.Y. Chen, L. Nazar, X.D. Wu, A. Inam, T. Venkatesan, Application of a near coincidence site lattice theory to the orientations of $YBa_2Cu_3O_{7-x}$ grains on (001) MgO substrates, Applied Physics Letters. 57 (1990) 1690–1692.

[188] D.M. Duffy, Grain boundaries in ionic crystals, J. Phys. C Solid State Physics. 19 (1986) 4393–4412.

Curriculum Vitae

Education and Research

Syracuse University

Ph.D. Mechanical and Aerospace Engineering, December 2017
Advisor: Dr. Jeongmin Ahn
Thesis: "*Oxygen transport membranes for oxy-fuel combustion process and carbon capture purposes"*
- Project 1: Oxygen Transport Membranes for Oxy-Fuel Combustion
- Project 2: Molecular Dynamic Simulation of Perovskite Structures and Grain Boundaries
- Project 3: CO_2 Tolerance of Dual-Phase Oxygen Transport Membranes
- Project 4: Approximating Oxygen Transport Membrane Performance for Combustion
- Project 5: Automatic Identification and Data Capture System for Material Characterization
- Project 6: Developing On-line Micro-Videos to be used as a Supplementary Course Material

M.S. Mechanical and Aerospace Engineering, May 2015
- Project 1: Anaerobic Digester System Integration with Solid Oxide Fuel Cells
- Project 2: Tubular Flame-Assisted Solid Oxide Fuel Cells
- Project 3: Innovating Engineering Education in an Energy System Course

B.S. Mechanical Engineering, May 2013
- Project 1: Dual-layer Solid Oxide Fuel Cells
- Project 2: Tooling Design for Extrusion

Teaching Experience

Teaching Assistant

- ECS 326: Engineering Materials, Properties, and Processing, Fall 2017
- MAE 486/686: Fuel Cell Science and Technology, Fall 2014 to Spring 2016
- ECS 221: Statics, Fall 2013/2014
- MAE 355: Fundamentals Heat and Mass Transfer, Spring 2014

Invited Lecturer

- MAE 251: Thermodynamics, Spring 2016
- MAE 655: Advanced Heat Transfer, Fall 2015

Teaching Mentor

- MAE 341: Fluid Mechanics, Fall 2015
- MAE 355: Fundamentals of Heat and Mass Transfer, Spring 2015

Honors

Awards

1st Place Poster: PhD Category at COE Symposium — October 2017
Center of Excellence, Syracuse University

Outstanding Teaching Assistantship Award — April 2016
Syracuse University

Best Poster at the General Electric Student Research Summit — August 2015
General Electric Global Research

Best Departmental Poster (Mechanical and Aerospace) — April 2014
Syracuse University Nunan Research Day

ASME George Farnell Senior Design Award — April 2013
Syracuse University

Best Student Paper Award
March 2013
ASEE St. Lawrence Conference

Fellowships

Syracuse University Graduate Fellowship — 2015-2017
Syracuse University

East Asia and Pacific Summer Institute Fellowship — Summer 2016
National Science Foundation

Leadership

American Society for Engineering Education at Syracuse University
April 2015-June 2017
President, Founder

College of Engineering and Computer Science Graduate Student Organization
April 2016-May 2017
Comptroller

Syracuse University Senate
April 2017-Present
Graduate Student Senator, Committee on Instruction Member

Graduate Student Organization
December 2015-Present
At-Large Senator, Finance Committee Member

Publications

Ryan L. Falkenstein-Smith, Matthew Rushby, and Jeongmin Ahn, "Approximating the permeability of oxygen transport membrane reactors for oxy-fuel combustion", Proceedings of the Combustion Institute, (2017): submitted.

Ryan L. Falkenstein-Smith, Ryan Milcarek, and Jeongmin Ahn, "Enhancing and Evaluating T-shape Professional Skills through Innovative Energy Education", Advances in Engineering Education, (2017): submitted.

Ryan L. Falkenstein-Smith, Matthew Rushby and Jeongmin Ahn, "Exploring the performance of dual-phase oxygen transport membranes for carbon capture purpose", Journal of Fluid Science and Technology, (2017): submitted.

Ryan L. Falkenstein-Smith, Pingying Zeng and Jeongmin Ahn, "Investigation of oxygen transport membrane reactors for oxy-fuel combustion and carbon capture purposes", Proceedings of the Combustion Institute, 36.3 (2017): 3969-3976.

Ryan L. Falkenstein-Smith and Jeongmin Ahn, "Experimental study of oxygen transport membranes for oxy-fuel combustion reactors", Journal of Fluid Science and Technology, 11.4 (2016): JFST0025-JFST0025.

Wei Liu, Ryan Milcarek, **Ryan L. Falkenstein-Smith** and Jeongmin Ahn, "Interfacial impedance studies of multilayer structured electrolyte fabricated with solvent-casted PE_{10} - $LiN(CF_3SO_2)_2$ and Ceramic $Li_{1.3}Al_{0.3}Ti_{1.7}(PO_4)_3$ and its application in all-solid-state lithium ion batteries", Journal of Electrochemical Energy Conversion and Storage, 13.2 (2016): 021008-021014.

Ryan Milcarek, Kang Wang, **Ryan L. Falkenstein-Smith**, and Jeongmin Ahn, "Performance Variation with SDC Buffer Layer Thickness", International Journal of Hydrogen Energy, 41.22 (2015): 9500-9506

Ryan Milcarek, Kang Wang, **Ryan L. Falkenstein-Smith**, and Jeongmin Ahn, "Micro-tubular flame-assisted fuel cell for micro-combined heat and power systems", Journal of Power Sources, 306 (2015): 148-151.

Pingying Zeng, Kang Wang**, Ryan L. Falkenstein-Smith**, and Jeongmin Ahn, "Effects of Sintering Temperature on the Performance of $SrSc_{0.1}Co_{0.9}O_{3-\delta}$ Oxygen Semipermeable Membrane", Brazilian Journal of Chemical Engineering, 32.3 (2014) 757-765.

Kang Wang, Pingying Zeng, **Ryan L. Falkenstein-Smith**, and Jeongmin Ahn, "Flame-assisted Fuel Cells for the Power Generation Systems", KSEA Letters, 41.3 (2013) 25-26.

Conference Papers

Ryan L. Falkenstein-Smith, Matthew Rushby, Hiroki Nagashima, Takashi Tokumasu, and Jeongmin Ahn, "High Performing Oxygen Transport Membrane Reactors for Oxy-fuel Combustion", 14th International Conference on Flow Dynamics (ICFD), Sendai, Japan, November 2017.

Hiroki Nagashima, Ryan L. Falkenstein-Smith, Takashi Tokumasu, and Jeongmin Ahn, "Characterization of Transport Phenomena of Oxygen Ion in Electrolyte of Solid Oxide Fuel Cell", 14th International Conference on Flow Dynamics (ICFD), Sendai, Japan, November 2017.

Ryan L. Falkenstein-Smith, Matthew Rushby, and Jeongmin Ahn, " Composite oxygen transport membrane reactors for oxy-fuel combustion processes", US National Technical Meeting of the Combustion Institute, College Park, MD, May 2017.

Ryan L. Falkenstein-Smith, Matthew Rushby, Hiroki Nagashima, Takashi Tokumasu, and Jeongmin Ahn, "Exploring the Performance of Dual-Phase Oxygen Transport Membranes for Carbon Capture Purposes", 13th International Conference on Flow Dynamics (ICFD), Sendai, Japan, October 2016.

Ryan L. Falkenstein-Smith, Jack S. Rossetti, Michael Garrett, and Jeongmin Ahn, "Investigating the Influence of Micro-Videos used as a Supplementary Course Material", ASEE Annual Conference and Exposition 2016 (ASEE 2016), New Orleans, LA, June 2016

Ryan L. Falkenstein-Smith, Ryan Milcarek, Michael Garrett, and Jeongmin Ahn, "Exploring T-Shaped Professional Skill Development in Graduate Students in an Advanced Energy Systems Course", ASEE Annual Conference and Exposition 2016 (ASEE 2016), New Orleans, LA, June 2016.

Pingying Zeng, Kang Wang, Ryan L. Falkenstein-Smith, and Jeongmin Ahn, "A Ceramic Membrane Based Oxy-fuel Combustion", 12th International Conference on Flow Dynamics (ICFD), Sendai, Japan, October 2015.

Ryan L. Falkenstein-Smith, Ryan Milcarek, Kang Wang, and Jeongmin Ahn, "Developing T-Shaped Professional Engineers Through an Advance Energy System Course", ASEE Annual Conference and Exposition 2015 (ASEE 2015), Seattle, WA, June 2015.

Ryan Falkenstein-Smith, Kang Wang, Ryan Milcarek, and Jeongmin Ahn. "Integrated Anaerobic Digester and Fuel Cell Power Generation System for Community Use.", ASME 2015 13th International Conference on Fuel Cell Science, Engineering and Technology collocated with the ASME 2015 Power Conference, the ASME 2015 9th International Conference on Energy Sustainability, and the ASME 2015 Nuclear Forum, San Diego, CA, June 2015.

Ryan Milcarek, Kang Wang, Ryan Falkenstein-Smith, Jeongmin Ahn, and H. E. Khalifa. "Flame-Assisted Fuel Cell Operating With Methane for Combined Heating and Micro Power.", ASME 2015 13th International Conference on Fuel Cell Science, Engineering and Technology collocated with the ASME 2015 Power Conference, the ASME 2015 9th International Conference on Energy Sustainability, and the ASME 2015 Nuclear Forum, San Diego, CA, June 2015.

Ryan L. Falkenstein-Smith, Pingying Zeng, and Jeongmin Ahn, "Ceramic Planar and Tubular Reactor Membranes for Oxy-fuel Combustion Processes", US National Technical Meeting of the Combustion Institute, Cincinnati, OH, May 2015.

Ryan L. Falkenstein-Smith, Pingying Zeng, Tyler Culp, and Jeongmin Ahn, "Thermal Transpiration Based Propulsion", ASME Conference Proceedings, ASME International Mechanical Engineers Congress and Exposition (IMECE2014), Montreal, Canada, November 2014.

Pingying Zeng, Kang Wang, Ryan L. Falkenstein-Smith, and Jeongmin Ahn, "A Ceramic Membrane Based Methane Combustion Reactor with Tailored Function of Simultaneous Separation of Carbon-dioxide from Nitrogen", ASME International Mechanical Engineers Congress and Exposition (IMECE2014), Montreal, Canada, November 2014.

Ryan L. Falkenstein-Smith, Ryan J. Milcarek, Kang Wang, and Jeongmin Ahn, "Integrated Anaerobic Digester and Fuel Cell Power Generation System for Community Use", 1000 Island Energy Research Forum (TIERF), Ottawa, Canada, October 2014.

Ryan L. Falkenstein-Smith, Pingying Zeng, and Jeongmin Ahn, "A Ceramic Membrane Based on Oxy-Fuel Combustion Processes", 1000 Island Energy Research Forum (TIERF), Ottawa, Canada, October 2014.

Pingying Zeng, Kang Wang, Ryan L. Falkenstein-Smith, Jeongmin Ahn, and Paul D. Ronney, "Thermal Transpiration Based Pumping and Power Generation Device", ASME 2014 12th International Conference on Fuel Cell Science, Engineering and Technology collocated with the ASME 2014 Power Conference, the ASME 2014 8th International Conference on Energy Sustainability, and the ASME 2014 Nuclear Forum, Boston, MA, June 2014.

Pingying Zeng, Kang Wang, Ryan L. Falkenstein-Smith, and Jeongmin Ahn, "A Ceramic-Membrane-Based Methane Combustion Reactor with Tailored Function of Simultaneous Separation of Carbon Dioxide from Nitrogen", ASME 2014 12th International Conference on Fuel Cell Science, Engineering and Technology collocated with the ASME 2014 Power Conference, the ASME 2014 8th International Conference on Energy Sustainability, and the ASME 2014 Nuclear Forum, Boston, MA, June 2014.

Ryan L. Falkenstein-Smith, Kang Wang, and Jeongmin Ahn, "Revitalizing Engineering Education through Practical Applications of Advanced Energy Systems", ASEE Annual Conference and Exposition 2015 (ASEE 2015), Indianapolis, IN, June 2014.

Kang Wang, Pingying Zeng, Ryan L. Falkenstein-Smith, and Jeongmin Ahn, "An Electricity and Value-added Gases Co-generation via Solid Oxide Fuel Cells", ASME International Mechanical Engineers Congress and Exposition (IMECE2013), San Diego, CA, November 2013.

Pingying Zeng, Ryan L. Falkenstein-Smith, Kang Wang, and Jeongmin Ahn, "Single-phase Ceramic Membranes integrated with Combustion Processes", ASME International Mechanical Engineers Congress and Exposition (IMECE2013), San Diego, CA, November 2013.

Kang Wang, Pingying Zeng, Ryan L. Falkenstein-Smith, and Jeongmin Ahn, "An Electricity and Value-added Gases Co-generation via Solid Oxide Fuel Cells", US National Technical Meeting of the Combustion Institute, Salt Lake City, UT, May 2013.

Pingying Zeng, Ryan L. Falkenstein-Smith, Kang Wang, and Jeongmin Ahn, "A Ceramic Membrane Reactor for Methane Combustion Processes", US National Technical Meeting of the Combustion Institute, Salt Lake City, UT, May 2013.

Kang Wang, Ryan L. Falkenstein-Smith, and Jeongmin Ahn, "Revitalizing Engineering Education through Practical Applications of Advanced Energy Systems", Conference for the St. Lawrence Section of the American Society of Engineering Education, Buffalo, NY, April 2013.

Conference Presentations and Posters

Ryan L. Falkenstein-Smith, Matthew Rushby, Hiroki Nagashima, Takashi Tokumasu, and Jeongmin Ahn, "High Performing Oxygen Transport Membrane Reactors for Oxy-fuel Combustion", 14th International Conference on Flow Dynamics (ICFD), Sendai, Japan, November 2017.

Ryan L. Falkenstein-Smith, Matthew Rushby, and Jeongmin Ahn, " Composite oxygen transport membrane reactors for oxy-fuel combustion processes", US National Technical Meeting of the Combustion Institute, College Park, MD, May 2017.

Ryan L. Falkenstein-Smith, Matthew Rushby, Hiroki Nagashima, Takashi Tokumasu, and Jeongmin Ahn, "Exploring the Performance of Dual-Phase Oxygen Transport Membranes for Carbon Capture Purposes", 13th International Conference on Flow Dynamics (ICFD), Sendai, Japan, October 2016.

Pingying Zeng, Kang Wang, Ryan L. Falkenstein-Smith, and Jeongmin Ahn, "A Ceramic Membrane Based Oxy-fuel Combustion", 12th International Conference on Flow Dynamics (ICFD), Sendai, Japan, October 2015.

Ryan L. Falkenstein-Smith, Pingying Zeng, and Jeongmin Ahn, "Ceramic Reactor Membrane for Oxy-Fuel Combustion Processes", 4th Annual Student Research Summit at the General Electric (GE) Global Research, Niskayuna, NY, August 2015.

Ryan L. Falkenstein-Smith, Ryan Milcarek, Kang Wang, and Jeongmin Ahn, "Developing T-Shaped Professional Engineers Through an Advance Energy System Course", ASEE Annual Conference and Exposition 2015 (ASEE 2015), Seattle, WA, June 2015.

Ryan Falkenstein-Smith, Kang Wang, Ryan Milcarek, and Jeongmin Ahn. "Integrated Anaerobic Digester and Fuel Cell Power Generation System for Community Use.", ASME 2015 13th International Conference on Fuel Cell Science, Engineering and Technology collocated with the ASME 2015 Power Conference, the ASME 2015 9th International Conference on Energy Sustainability, and the ASME 2015 Nuclear Forum, San Diego, CA, June 2015.

Ryan L. Falkenstein-Smith, Pingying Zeng, and Jeongmin Ahn, "Ceramic Planar and Tubular Reactor Membranes for Oxy-fuel Combustion Processes", US National Technical Meeting of the Combustion Institute, Cincinnati, OH, May 2015.

Pingying Zeng, Kang Wang, Ryan L. Falkenstein-Smith, and Jeongmin Ahn, "A Ceramic Membrane Based Methane Combustion Reactor with Tailored Function of Simultaneous Separation of Carbon-dioxide from Nitrogen", ASME International Mechanical Engineers Congress and Exposition (IMECE2014), Montreal, Canada, November 2014.

Ryan J. Milcarek, Kang Wang, Ryan L. Falkenstein-Smith, Jeongmin Ahn, and H. Ezzat Khalifa, "Flame-assisted Fuel Cell Furnace for micro Combined Heating and Power (FFF-ìCHP)", Syracuse COE Symposium, Syracuse, NY, October 2014.

Ryan L. Falkenstein-Smith, Ryan J. Milcarek, Kang Wang, and Jeongmin Ahn, "Integrated Anaerobic Digester and Fuel Cell Power Generation Systems for Community Use", Syracuse COE Symposium, Syracuse, NY, October 2014.

Ryan L. Falkenstein-Smith, Ryan J. Milcarek, Kang Wang, and Jeongmin Ahn, "Integrated Anaerobic Digester and Fuel Cell Power Generation System for Community Use", 1000 Island Energy Research Forum (TIERF), Ottawa, Canada, October 2014.

Ryan L. Falkenstein-Smith, Pingying Zeng, and Jeongmin Ahn, "A Ceramic Membrane Based on Oxy-Fuel Combustion Processes", 1000 Island Energy Research Forum (TIERF), Ottawa, Canada, October 2014.

Ryan L. Falkenstein-Smith, Kang Wang, and Jeongmin Ahn, "Integrated Anaerobic Digester and Fuel Cell Power Generation System for Community Use", The 35th International Symposium on Combustion, San Francisco, CA, August 2014.

Shirin Jouzdani, Ryan L. Falkenstein-Smith, Pingying Zeng, and Jeongmin Ahn, "Thermal Transpiration Based Pumping and Propulsion Device", The 35th International Symposium on Combustion, San Francisco, CA, August 2014.

Pingying Zeng, Kang Wang, Ryan L. Falkenstein-Smith, Jeongmin Ahn, and Paul D. Ronney, "Thermal Transpiration Based Pumping and Power Generation Device", ASME 2014 12th International Conference on Fuel Cell Science, Engineering and Technology collocated with the ASME 2014 Power Conference, the ASME 2014 8th International Conference on Energy Sustainability, and the ASME 2014 Nuclear Forum, Boston, MA, June 2014.

Pingying Zeng, Kang Wang, Ryan L. Falkenstein-Smith, and Jeongmin Ahn, "A Ceramic-Membrane-Based Methane Combustion Reactor with Tailored Function of Simultaneous Separation of Carbon Dioxide from Nitrogen", ASME 2014 12th International Conference on Fuel Cell Science, Engineering and Technology collocated with the ASME 2014 Power Conference, the ASME 2014 8th International Conference on Energy Sustainability, and the ASME 2014 Nuclear Forum, Boston, MA, June 2014.

Ryan L. Falkenstein-Smith, Kang Wang, and Jeongmin Ahn, "Revitalizing Engineering Education through Practical Applications of Advanced Energy Systems", ASEE Annual Conference and Exposition 2015 (ASEE 2015), Indianapolis, IN, June 2014.

Kang Wang, Ryan Milcarek, Ryan L. Falkenstein-Smith, Jeongmin Ahn, and H. Ezzat Khalifa, "Flame-Assisted Fuel Cell Furnace MicroCHP (FFF ìCHP)", Nunan Lecture and Research Day, Syracuse, NY, April 2014.

Ryan L. Falkenstein-Smith, Kang Wang, Sara E. Silverstone, and Jeongmin Ahn, "Integrated Anaerobic Digester and Fuel Cell Power Generation System for Community Use", Nunan Lecture and Research Day, Syracuse, NY, April 2014.

Pingying Zeng, Ryan L. Falkenstein-Smith, Kang Wang, and Jeongmin Ahn, "Single-phase Ceramic Membranes integrated with Combustion Processes", ASME International Mechanical Engineers Congress and Exposition (IMECE2013), San Diego, CA, November 2013.

Ryan L. Falkenstein-Smith, Pingying Zeng, and Jeongmin Ahn, "CO_2 Separation Process using Ceramic Hollow Fibre Membranes", CASE NEXT Conference, Liverpool, NY, November 2013.

Kang Wang, Ryan L. Falkenstein-Smith, Pingying Zeng, and Jeongmin Ahn, "An Electricity and Value-Added Gases Co-Generation System via SOFC ", CASE NEXT Conference, Liverpool, NY, November 2013.

Kang Wang, Pingying Zeng, Ryan L. Falkenstein-Smith, and Jeongmin Ahn, "An Electricity and Value-added Gases Co-generation via Solid Oxide Fuel Cells", Nunan Lecture and Research Day, Syracuse, NY, April 2013.

Pingying Zeng, Ryan L. Falkenstein-Smith, Kang Wang, and Jeongmin Ahn, "A Ceramic Membrane Reactor for Methane Combustion Processes", US National Technical Meeting of the Combustion Institute, Salt Lake City, UT, May 2013.

Kang Wang, Ryan L. Falkenstein-Smith, and Jeongmin Ahn, "Revitalizing Engineering Education through Practical Applications of Advanced Energy Systems", Conference for the St. Lawrence Section of the American Society of Engineering Education, Buffalo, NY, April 2013.

Ryan L. Falkenstein-Smith, Pingying Zeng, and Jeongmin Ahn, "CO_2 Separation Process using Ceramic Hollow Fibre Membranes", ASME International Mechanical Engineering Congress and Exposition (IMECE), Houston, TX, November 2012.